TÉCNICO LISBOA

On the design of thermal management systems for hybrid-electric aircraft

Maria Maia Coutinho

Thesis to obtain the Master of Science Degree in

Aerospace Engineering

Supervisors: Prof. Afzal Suleman
Prof. Frederico José Prata Rente Reis Afonso

Examination Committee

Chairperson: Prof. Filipe Szolnoky Ramos Pinto Cunha
Supervisor: Prof. Afzal Suleman
Member of the Committee: Prof. Pedro Jorge Martins Coelho

December 2022

The rest is still unwritten...

Declaração

Declaro que o presente documento é um trabalho original da minha autoria e que cumpre todos os requisitos do Código de Conduta e Boas Práticas da Universidade de Lisboa.

Declaration

I declare that this document is an original work of my own authorship and that it fulfills all the requirements of the Code of Conduct and Good Practices of the Universidade de Lisboa.

Agradecimentos

Em primeiro lugar, gostaria de agradecer ao Prof. Afzal Suleman, ao Prof. Fernando Lau, ao Alain Souza, à Iara Figueiras e ao David Bento pelo apoio durante todo o projeto. Agradeço ainda a bolsa de estudo co-financiada pelo IDMEC no âmbito do projeto FutPrInt50 (PE677). Manifesto também o meu agradecimento à equipa da Embraer, em especial, ao Felipe Reyes e Ricardo Gandolfi, pela oportunidade e pelo auxílio prestado. Ainda neste contexto, um especial agradecimento ao Prof. Frederico Afonso pela incansável ajuda. O que aprendi com o professor ao longo dos últimos 8 meses, vai muito além do conteúdo presente nesta dissertação. Certamente, o levarei como um exemplo de dedicação, trabalho e educação para as próximas etapas da minha vida.

De seguida, agradeço aos meus amigos de longa data, aos ”Reformados” e a todos os colegas que cruzaram o meu caminho e que o tornaram, de certa forma, mais fácil. Agradeço ainda à Inês e à Filipa pelas memórias do 3ºDto. Foram essenciais neste processo ao tornarem os meus dias mais leves e ao me ajudarem a ultrapassar os momentos de desânimo.

Ainda, aos que remaram juntamente comigo durante estes anos, entre eles, Mariana Costa, André Pereira, Beatriz Casqueiro e Mariana Ribeiro, o meu mais sincero obrigado. Ao grupo de Barcelona, Leonardo, João, Afonso, Guadalupe e Margarida, agradeço por terem partilhado comigo a maior e melhor experiência da minha vida.

Não posso deixar de agradecer ao André, pela paciência e companheirismo e por me incentivar, todos os dias, a ser a minha melhor versão.

À Associação Gímnica de Águeda e a toda equipa por sempre apoiarem os meus sonhos e me permitirem viver e conciliar o desporto com o meu percurso académico.

À minha família, mãe, pai, mano, avó, avô e Fernanda, que foram a minha maior força durante estes cinco anos. Foram eles que me ouviram, apoiaram e acreditaram em mim. Certamente não estaria onde estou hoje sem eles e nunca irei conseguir agradecer o suficiente pelo apoio incondicional.

Resumo

Uma das potenciais soluções para reduzir a pegada ambiental da aviação é a introdução de sistemas de propulsão híbridos. No entanto, visto que estes sistemas aumentam a quantidade de calor gerado na aeronave, é necessário desenvolver um sistema de gestão térmica capaz de lidar com os problemas inerentes a este aumento de calor dissipado. Nesse sentido, o principal objetivo deste trabalho é identificar tecnologias promissoras de transmissão de calor para serem integradas num sistema de gestão térmica que minimize o seu impacto na aeronave regional do projeto FutPrInt50 em termos de potência, massa e resistência aerodinâmica.

Tendo em vista este objetivo, são modelados em Matlab/Simulink cinco sistemas de gestão térmica, os quais são constituídos por um circuito de líquido fechado, integrando diferentes dissipadores de calor identificados como promissores. A capacidade de refrigeração e o efeito no desempenho da aeronave em diferentes condições de voo são as métricas utilizadas para comparar as diferentes arquiteturas. Posteriormente, é realizado um estudo paramétrico seguido de um estudo de otimização multi-objetivo, visando minimizar o impacto dos sistemas de gestão térmica no desempenho da aeronave.

Nenhuma das arquiteturas investigadas revelou ter um desempenho ótimo em todas as métricas estudadas. Deste modo, a investigação concluiu que enquanto se planeia o sistema térmico para futuros aviões híbridos elétricos, várias arquiteturas alternativas devem ser analisadas à luz dos requisitos de potência e necessidades de projeto.

Palavras-chave: sistema de gestão térmica, propulsão hibrida-elétrica, otimização multi-objetivo, permutador de calor de superfície, combustível

Abstract

The electrification of aircraft propulsive system is identified as a potential solution towards a lower carbon footprint in the aviation industry. One of the effects of increased electrification is the generation of a large amount of waste heat that needs to be removed. As high-power systems must be cooled to avoid performance deterioration such as battery thermal runaway, a suitable thermal management system is required to regulate the thermal behaviour of the powertrain components. With this in mind, the main objective of this thesis is to identify promising heat transfer technologies to be integrated into a Thermal Management System (TMS) such that power, mass, and drag can be minimised for a parallel hybrid-electric regional aircraft in the context of an EU-funded FutPrInt50 project.

Five different TMS architectures are modelled using the Matlab/Simulink environment based on thermodynamic principles, heat transfer fundamentals, and fluid flow equations. The systems are a combination of a closed-loop liquid cooling integrated with different heat dissipation components, namely, ram air, skin heat exchanger, and fuel. Their cooling capacity and overall aircraft performance penalties under different flight conditions are estimated and compared to each other. Then, a parametric study is conducted, followed by a multi-objective robust optimisation analysis with the aim of minimising the TMS impact.

None of the investigated architectures exhibits an ideal performance across the range of the studied metrics. The research revealed that while planning the TMS for future hybrid-electric aircraft, alternative architectures will need to be developed and studied in light of the power requirements.

Keywords: thermal management system, hybrid-electric propulsion, multi-objective optimisation, skin heat exchanger, ram air, fuel

Contents

List of Tables

List of Figures

Abbreviations

A	TMS proposed Architecture
AC	Alternating Current
ASTM	American Society for Testing and Materials
ATJ-SPK	Alcohol-to-Jet Synthetic Paraffinic Kerosene
ATM	Air Traffic Management
ATR	Avions de transport regional
BLI	Boundary Layer Ingestion
CAD	Computer-Aided Design
CEA	Chemical Equilibrium with Applications
CFD	Computational Fluid Dynamics
CL	Climb
CR	Cruise
DC	Direct Current
DP	Distributed Propulsion
EASA	European Union Aviation Safety Agency
ECS	Environment Control System
EFA	Engine Fan Air
EGW	Mixture of 60% of Ethylene-Glycol and 40% Water
EM	Electric Motor
ESAero	Empirical Systems Aerospace
FC	Fuel Cell
FEM	Finite Element Method

FHX	Fuel Heat eXchanger
FMDU	Fuel Management and Distribution Unit
FT-SPK	Fischer-Tropsch hydroprocessed Synthesized Paraffinic Kerosene
FTMS	Fuel Thermal Management System
GA	Genetic Algorithm
HEATheR	High-Efficiency Aircraft Thermal Research
HEFA-SPK	Synthesized Paraffinic kerosene produced from Hydroprocessed Esters and Fatty Acids
HEMM	High Efficiency Megawatt Motor
HEP	Hybrid Electric Propulsion
HEX	Heat EXchanger
HTO	Hot day Take-Off
ICE	Internal Combustion Engine
IMD	Integrated Motor Drives
ISA	International Standard Atmosphere
JP	Jet Propellant
LB	Lower Boundary
LMTD	Log Mean Temperature Difference
MTOM	Maximum Take-Off Mass
NACA	National Advisory Committee for Aeronautics
NASA	National Aeronautics and Space Administration
NSGA-II	Non-dominated Sorting Genetic Algorithm
OML	Outer Mould Line
PAO	Polyalphaolefin
PCM	Phase Change Material
PEGASUS	Parallel Electric-Gas Architecture with Synergistic Utilisation Scheme
PGW30	Propylene Glycol Water 30%
PH	Parallel Hybrid
PMDU	Power Management and Distribution Unit

PSF-5	Pure Silicone Fluid with a viscosity of 5cSt
RA	Ram Air
RBDO	Reliability Based Design Optimisation
RDO	Robust Design Optimisation
RHX	Ram air Heat eXchanger
RPK	Revenue Passenger Kilometer
RVLT	Revolutionary Vertical Lift Technology
SAE	Society of Automotive Engineers
SAF	Sustainable Aviation Fuel
SH	Series Hybrid
SHP	Series Parallel Hybrid
SHX	Skin Heat eXchanger
SP	Sigma Point
STARC-ABL	Single-aisle Turboelectric AiRCraft with an Aft Boundary-Layer propulsor
SUSAN	Subsonic Single Aft eNgine
TE	Turboelectric
TLAR	Top-Level Aircraft Requirement
TMS	Thermal Management System
TO	Take-Off
TRL	Technology Readiness Level
UAM	Urban Air Mobility
UB	Upper Boundary
ULI	University Leadership Initiative
VCS	Vapour Compression System
VTOL	Vertical Take-Off and Landing

Nomenclature

Greek symbols

β	Surface density, m^2/m^3
γ	Ratio of specific heats
η	Thermodynamic efficiency
κ	Thermal conductivity, W/mK
μ	Viscosity, kg/ms
μ_g	Mean value
ρ	Mass density, kg/m^3
σ	Porosity factor
σ_g	Standard deviation

Roman symbols

A	Area, m^2
b	Wing span, m
COP	Coefficient of performance
c	Wing chord, m
C_D	Coefficient of drag
c_p	Specific heat at constant pressure, J/kgK
D	Drag, N
D_h	Hydraulic diameter, m
E	Energy, J
e	Emission factor, g/g or g/J
e^*	Energy density, J/kg

f Friction factor

G Robust objective function

g Objective function

h Enthalpy per unit of mass, J/kg

h Convection heat transfer coefficient W/m^{2}K;

L Length, m

$\dot{m}$ Mass flow rate, kg/s

M Mach number

m Mass, kg

Nu Nusselt number

O_{liquid} Mass flow rate of the liquid per kW, kg/(skW)

P Probability

p Pressure, Pa

Pr Prandtl number

$\dot{Q}$ Heat transfer rate, W

R Universal Gas Constant, J/kgK

Re Reynolds number

s Entropy, J/kgK

T Temperature, K

t Thickness, m

U Global heat transfer coefficient, W/m^{2}K

V Volume, m^3

v Scalar velocity, m/s

W Power, W

X Distance along the fuselage from the aircraft nose, m

x Design variable

Subscripts

$1, 2, 3, 4$ Different states of a system

∞	Free-stream condition
al	Aluminium
aw	Adiabatic wall
av	Available
b	Bottom
bd	Boundary layer
bat	Battery
cs	Consumption
cv	Control volume
c	Cold
comp	Compressor
e	Engine fuel
equip	Propulsion components
evap	Evaporator
ext	Exterior
f	Fuel
h	Hot
i	Inlet
int	Interior
isen	Isentropic
lm	Log mean condition
liquid	Ethylene-glycol and water mixture
n	Nozzle
o	Outlet
p	Production
r	Recirculation fuel
re	Recharge
ref	Refrigerant R314a

s Side

surf Surface

T Fuel tank

Superscripts

* Reference value

Chapter 1

Introduction

This chapter will provide an outline of the motivation for the work presented in this thesis, along with a short overview of Hybrid-Electric Propulsion (HEP) and Thermal Management Systems (TMS) topics. A description of the main goals of the research project and the methodology followed are detailed here, as well as a brief summary of how this thesis is organised.

1.1 Motivation and topic overview

The aviation sector is currently facing new challenges such as energy demand and environmental impact. From 2013 to 2019, the number of flight departures increased by 22% and Revenue Passenger Kilometers (RPKs) increased by 50%. In fact, passenger air traffic increased nearly four times faster than fuel efficiency improved [1]. The report *"Flightpath 2050: Europe's vision for future aviation"* published by the European Commission and Advisory Council for Aviation Research and Innovation in Europe set a series of goals that must be accomplished by the year 2050 [2]. Since aviation is responsible for approximately 2.4% of global CO_2 emissions [3], one of the objectives of Flightpath 2050 is to reduce by 75% CO_2 emissions per passenger kilometer by 2050. It also aims for a 90% NO_x and 65% noise emissions reduction. These goals cannot be accomplished with small advancements in gas-turbine technology or tiny changes in aircraft design. This way, sustainable design is quickly becoming a key factor in the development of the next generation aircraft. Due to its inherent complexity, close collaboration among the various disciplines involved is needed. A multidisciplinary aircraft design will be crucial, beginning with the requirements and specifications, followed by the development of restrictions based on airworthiness, performance, and safety [4]. According to Afonso et al. [5], five key disciplines show up in this domain, including aerodynamics, propulsion, energy, materials, and structures, as presented in Figure 1.1.

As highlighted, the interaction of propulsion and energy fields is of particular interest. Using electric powertrains and cleaner energy sources as a propulsive system seems to be a promising solution. Some design possibilities are being carefully investigated to meet the Flightpath 2050 goals, namely the Hybrid-Electric Aircraft (HEA) and the All Electric Aircraft [6]. The goal of these designs is to

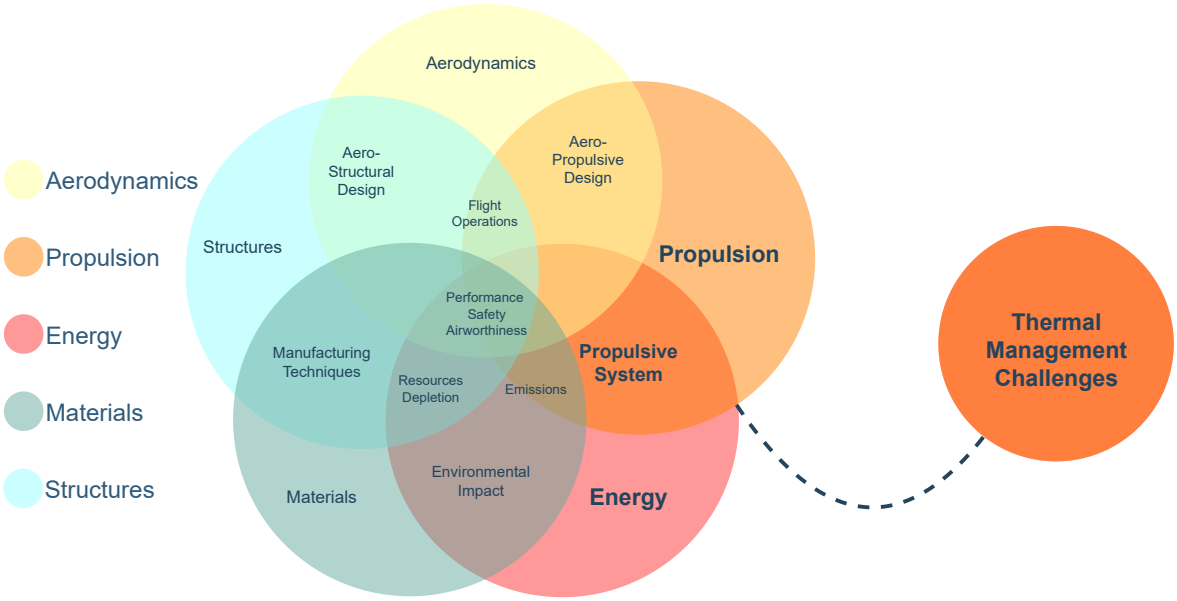

Figure 1.1: Venn diagram for sustainable aviation, adapted from [5].

bring together a variety of electric energy sources and energy conversion technologies that are able to provide several advantages on fuel, emissions, and noise reduction [7]. The adoption of battery-electric powertrains, which replace totally or partially traditional jet engines, is a potential method for short-haul flights. Furthermore, sustainable aviation fuels (SAFs) may replace fossil kerosene as an energy source without requiring any changes to the powertrain layout, resulting in considerable cost savings [8]. The ultimate goal may also include carbon free combustion using hydrogen in a hydrogen gas turbine or using a fuel cell powering electric motors. These architectures are promising options but imply huge design changes due to the low volumetric density of liquid hydrogen and its boiling point [9].

Hybrid-electric aircraft will offer a potential solution to reduce in-flight emissions. However, more electrification results in more electric losses, which in turn produce more heat, rising some thermal challenges as highlighted in Figure 1.1. More electric aircraft have increased demands on engines for thrust and power generation, leading to hotter fluids, greater component temperatures, and increased heat generation. Although electrical equipment is typically efficient, the enormous amount of electrical power needed (in the Megawatt range) will result in significant power losses. For example, in the class of a regional jet explored by the National Aeronautics and Space Administration (NASA) program, each motor (8 motors in total) has a power of 2.1 MW and an efficiency of 0.98 [10]. The resulting heat is roughly 42 kW (336 kW total), which is much greater than the existing heat generated by the electric systems used in aeroplanes. Additionally, unlike the typical propulsion system where the majority of the heat generated can be disposed via exhaust air, the heat created by the electric propulsion system cannot be taken through the engine nozzles, making heat removal more difficult [11]. The use of ram air to cool electric motors and high-power electric systems is also limited because of their greater integration into the fuselage [5]. The risk of thermal runaway also increases with some systems, especially batteries that are considered low temperature sources [11].

For all these reasons, novel thermal management systems are required and may be designed in parallel with HEP architecture. Thermal management systems will be responsible for regulating the temperature of aircraft subsystems/ components by managing heat transfer between heat sources and heat sinks in order to optimise comfort, safety, and efficiency [12]. Therefore, the TMS major goal is to maximise the use of heat produced while avoiding excessive heat losses and, at the same time, allow diverse components and systems to run within a safe range to guarantee longer component life and performance, and to reduce the need for maintenance and services.

Within this framework, the FutPrInt50 project stands out as a critical endeavour aimed at finding answers to these technological issues that the aerospace sector will confront to meet the operational environmental targets for the next years. FutPrInt50 is a collaborative research initiative supported by the European Union that joins the work done by multiple universities and companies, including the original equipment manufacturer Embraer. The current FutPrInt50 mission statement is as follows [13]:

> *"To develop a synergetic aircraft design for a commercial regional hybrid-electric aircraft up to 50 seats for entry into service by 2035/2040, to identify key enabling technologies and a roadmap for regulatory aspects. The clean sheet aircraft design shall help accelerate and integrate hybrid-electric aircraft and technologies to achieve a sustainable competitive aviation growth, as well as acting as a disruptor to regulators, Air Traffic Management (ATM) and energy suppliers."*

This way, FutPrInt50 aims to discover and develop technologies and combinations that will help to speed up the entry into service of commercial regional HEA [12]. Regional aircraft is the focus of this project and most of the studies on hybridisation topic mainly because of two reasons [14]. First, the energy storage weight and volume are smaller since the trip duration is shorter. Second because regional planes are responsible for 14% of worldwide aviation CO_2 emissions [15] and their popularity in the next years is expected to grow. Therefore, starting hybridisation in this smaller aircraft and then expanding it to larger aircraft seems a promising strategy. Also, the current air travel disruption, with dramatic reductions in flights due to the COVID-19 pandemic led to a shift toward lower occupancy passenger vehicle options, highlighting the opportunities for small and low-cost aircraft by reducing passenger loads [16].

In the FutPrInt50 project, thermal management is one of the work packages. The outcomes that are anticipated from the TMS work package go from an update on the state-of-the-art for HEA TMS, passing through the modelling and evaluation of novel TMS architectures and to the production of a roadmap for HEA TMS [17]. This thesis work is part of a collaborative research with Embraer for the FutPrInt50 project in the TMS work package.

1.2 Objectives and approach

The research work presented in this document, as a FutPrInt50 collaboration, follows the same major objectives proposed by the project. The main goal is to study new and existing heat dissipation systems and develop possible thermal management system architectures for a future regional 50-seater HEA. This

will help to understand the influence of a TMS on the power, weight, and drag and study the feasibility of these hybrid-electric aircraft. With the models set, the work scope passes through developing an optimisation method to increase the overall performance of the different systems. A comparison between the different models is also a subject of discussion in this document.

In light of the scope and purpose of the research that has been provided, the following related research questions have been formulated and will be answered in this document: **(1)** Which heat transfer technologies seem to be more feasible? **(2)** Which points of the flight are the most critical in terms of cooling power required? **(3)** Which components/architectures are the most critical in terms of power consumption, volume, and weight? **(4)** How do different design parameters, such as the liquid mass flow rate of the coolant, affect the system? **(5)** How can the analysed architectures be optimised? **(6)** What are potential practical aircraft level issues of some components?

1.3 Document outline

This document continues in Chapter 2 providing a literature review on hybrid-electric propulsion systems and alternative fuels (Section 2.1), heat transfer technologies (Section 2.2) and novel TMS architectures (Section 2.3) being studied recently.

Chapter 3 starts by presenting some relevant information about the reference aircraft and mission (Section 3.1). Five different TMS architectures are proposed and presented in Section 3.2. The methods used to model the different components that incorporate each architecture, including individual flowcharts, are detailed in Section 3.3 and the verification of each component is described in Section 3.4. The simulation procedure (Section 3.5) and the further analysis using an optimisation algorithm (Section 3.6) are also documented in this chapter.

The results are presented in Chapter 4. First, the baseline parameters used are given in Section 4.1. Second, the baseline results are discussed in Section 4.2, including the impact of each architecture in terms of weight, drag penalty and energy consumption. Section 4.3 examines a parametric study carried out for different design variables, while Section 4.4 discusses the optimisation results obtained for some TMS architectures. Section 4.4 also includes the optimisation results of a coupled research between this work and HEP computational models developed in another thesis [18].

Finally, the conclusions and the recommendations for future research are given in Chapter 5.

Chapter 2

Literature review

In order to understand the data needed to develop thermal management systems for hybrid-electric aircraft, it is necessary to review the existing research efforts and studies prior to developing an actual methodology. This overview focuses on presenting the current TMS capabilities and identifying the gaps to be filled such that the initially proposed research objectives in Section 1.2 are achieved; firstly, the current hybrid-electric propulsion architectures are reviewed in Section 2.1 along with a discussion on the future usage of sustainable aviation fuels. In Section 2.2, an overview of the heat transfer technologies is presented, which includes a description of the general heat loads, heat sinks and heat transport components used in air vehicles. The main recent TMS architectures reported in the literature, that make use of the surveyed heat transfer technologies, are also described in this chapter (Section 2.3), as well as some new trends in thermal management (Section 2.2.4).

2.1 Theoretical overview of hybrid-electric propulsion systems and alternative fuels

2.1.1 Hybrid-electric propulsion systems

Hybrid-electric propulsion designs are classified by IATA [19] into the following five categories: Series Hybrid (SH), Parallel Hybrid (PH), Series/Parallel Hybrid (SPH), Fully/Partial Turboelectric (TE), and all electric.

On hybrid-electric aircraft, an Internal Combustion Engine (ICE) can be used to provide electric propulsive power, to drive directly a propeller and/or to recharge batteries. For **parallel hybrid** architectures, an ICE (turboprop/turbofan) and a battery powered Electric Motor (EM) are connected to two parallel propulsion shafts, which are mechanically coupled to a shaft that drives a fan. This allows one or both components to produce propulsion at any given moment. On the other hand, in **series hybrid** systems, only the electric motors are mechanically linked to the fans. In this latter architecture, the purpose of the ICE (turboshaft) is to drive an electric generator, which in turn powers the motors and/or charges the batteries. The motor can also be fed by the battery packs. Regarding, the **series/parallel hybrid**

systems, these architectures combine the two previously stated types. One or more fans may be driven directly by the ICE (turboprop/turbofan), while other fans can be driven completely by electric motors, which can be supplied by either a turboshaft driven generator or a battery [4].

Turboelectric systems are comparable to series but do not depend on batteries. To power the propellers, fuel energy is turned into electrical power. The ICE propels a generator which powers the EM that drives the fan. The distinction between entirely and partially turboelectric propulsion is based on whether or not the electrical propulsion provides all of the propelling force. In partial turboelectric design, the remaining propelling power is supplied by a turboprop/turbofan engine [20].

An **all electric** architecture relies solely on batteries for aircraft propulsion. The benefits include the higher efficiency of energy conversion of electric motors and converters when compared to ICEs, as well as the simpler control strategies required to manage a single power source. The main disadvantage is that actual battery technologies have a low energy density, making them unsuitable for most aircraft [4].

Figure 2.1 simply portrays the HEP architectures described above.

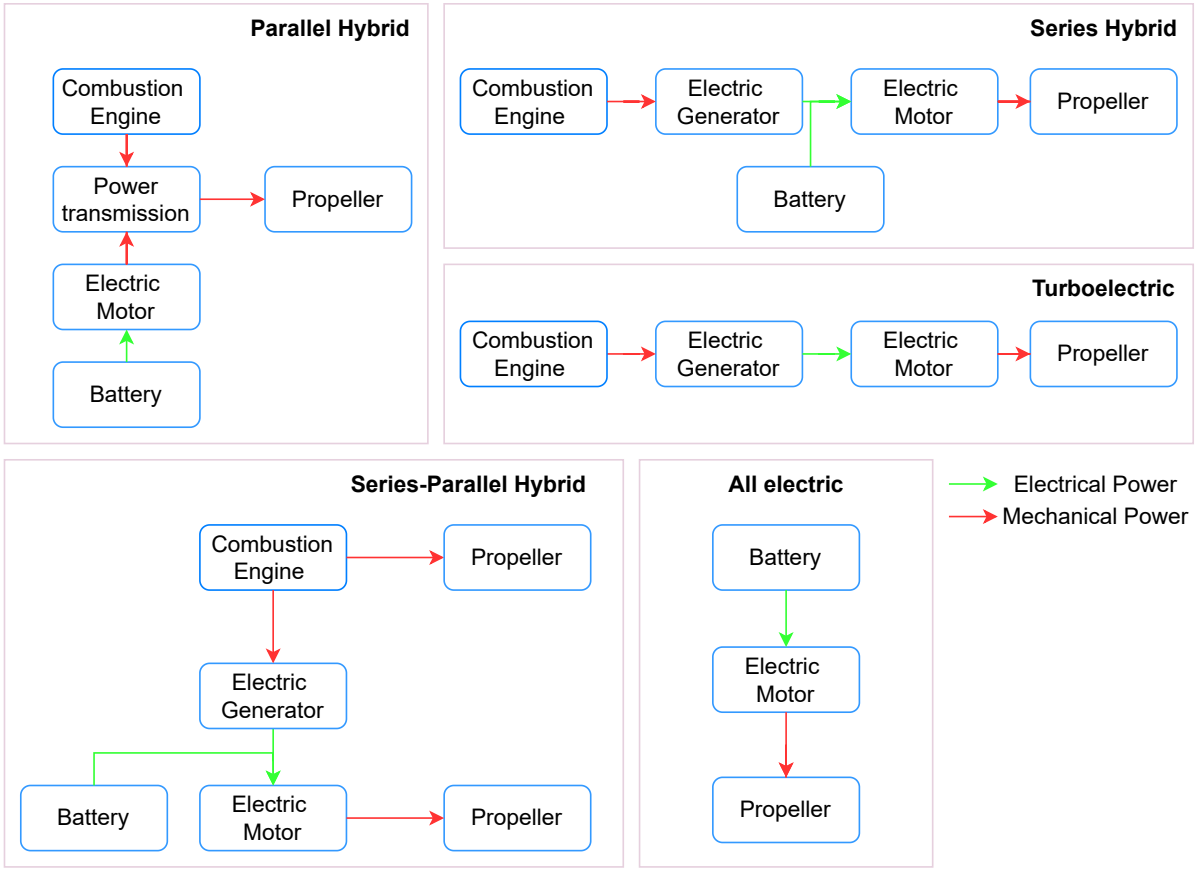

Figure 2.1: HEP architectures, adapted from [4, 20].

One of the main advantages of hybrid-electric architectures is the flexibility in transferring power throughout the vehicle, increasing the importance of propeller integration research in a multidisciplinary context [6]. The enhanced design freedom afforded by HEP enables unique methods of Distributing the Propellers (DP) on the aircraft such that its propulsive efficiency is increased [21]. Series hybrid and turboelectric systems, for example, are suitable for these distributed propulsion solutions using

several tiny motors and fans according to Felder from NASA [20]. One strategy used to decrease the induced drag coefficient and at the same time increase the maximum lift coefficient and effective aspect ratio is by placing the propeller on the wing tip. These aerodynamic advantages are realised when the propeller rotates in the opposite direction of the wingtip vortex, thereby attenuating the wingtip vortex and decreasing the downstream swirl [22]. However, this design option requires an aero-structural trade-off given the increase of the root bending moment due to the mass of the wingtip propulsion. Another concept where aerodynamic and propulsive performance gains are obtained is by employing propellers that ingest the boundary layer produced by the aircraft [23]. Multiple design studies for Boundary Layer Ingestion (BLI) integration use an aft-fuselage-mounted propulsion system. Despite this, it has not been implemented in a practical aircraft configuration since BLI system design is difficult [24]. All these technologies have synergistic relationships with hybrid-electric propulsion and may increase its overall performance.

In this context, in the last 10 years, aircraft designs using electricity for part or all of its propulsion power and new DP technologies have grabbed the public's interest and attracted considerable new coverage. Table 2.1 summarises some novel technologies and aircraft ideas that have been studied by different companies and institutions, such as Boeing, NASA, and Airbus. The Technology Readiness Level (TRL) of each architecture is also included [6, 25].

Zunum Aero is designing a 12-passenger series hybrid-electric regional aircraft with wing-integrated batteries for the ultimate transition to an entirely electric flight [26]. Eco4 also employs the architecture of SH, but implements a vertical tail-mounted propeller. Compared to contemporary conventional aircraft, the Eco4 design improves fuel consumption by 40% [25, 37]. PEGASUS (Parallel Electric-Gas Architecture with Synergistic Utilisation Scheme) is a parallel hybrid idea from NASA and it is intended for 200–400 nmi trips that are currently flown by turboprops like the ATR42 [6]. It is equipped with two wingtip-mounted turboprops, two mid-span electric motors with folding propellers, and a tail-cone pusher propeller using BLI technology. Moreover, the SUGAR Volt by Boeing has a PH architecture with two engines, a tube-shaped body, and a top-mounted truss-braced wing configuration [27]. Recently, Rolls-Royce and Airbus have cancelled an ambitious project on a series hybrid-electric demonstrator, E Fan-X, one year before its test flight. In the SH architecture, one of the four jet engines was replaced by a 2MW electric motor. The decision of quitting indicates a shift toward hydrogen-powered planes. Still, preliminary findings provided important information on component technologies, namely the world's most powerful aircraft generator (Mark I), built by Rolls Royce [30].

Is easy to conclude that, in a new era of electric flying, NASA is delving into revolutionary electrified aircraft propulsion. Electric vertical take-off and landing (eVTOL) vehicles have been created to fulfil the promise of an Urban Air Mobility (UAM) mission among these concepts. The air taxi concept for short ranges has been a topic of research activities [38]. NASA has developed some UAM configurations, highlighting a VTOL turboelectric tiltwing using Revolutionary Vertical Lift Technology (RVLT). This air taxi uses a turboelectric propulsion system where a turboshaft engine is used to produce electric power which is transmitted to the four electric motors one for each rotor. The on-board battery is used for emergency backup only [39]. In the regional range field, another concept for a partially turboelectric aircraft is being

Table 2.1: Summary of HEP aircraft concepts and studies.

Type of architecture	Aircraft	TRL	Range	Pax	Characteristics	Refs
Series hybrid Parallel hybrid SP hybrid	Zunum Aero (2023)	5-6	Regional	12	Series hybrid ICE-driven generator Two EM-driven fans	[26]
	NASA PEGASUS (2035)	4-5	Regional	50	ATR42-500 PH version Four wingtip propulsors BLI propulsor	[27]
	Eco4	3–4	Regional	4	Series hybrid Vertical tail propeller	[28]
	Boeing SUGAR Volt (2035)	2-3	Regional	154	Parallel hybrid Two engines Truss-braced wing	[29]
	E-FAN X (Cancelled)	6-7	Regional	-	Series hybrid One EM and three jet engines Mark I generator	[30]
Turboelectric	NASA STARC-ABL (2035)	3-4	Regional	154	Two turbofan engines Electric tail fan for BLI	[31]
	ESAero ECO-150R (2035)	2-3	Regional	150	DP system Split-wing	[32]
	VTOL tiltwing	-	UAB	6	Battery for emergency Four propellers	[28]
	NASA ULI aircraft	-	Regional	76	DP system Eight motors	[28]
	NASA N3-X (2045)	3-4	Regional	300	Superconducting DP	[33]
All electric	Eviation Alice (2022)	6–7	Regional	9	Lithium-ion battery EM on wingtips Tail EM	[34]
	NASA X-57 Maxwell (2022)	4-5	Regional	2	Twelve EM in DP Lithium-ion battery	[35]
	Airbus VoltAir (2035)	2-3	Regional	33	Two counter-rotating propellers Two EM BLI and laminar flow wing	[36]

developed: the Single-Aisle Turboelectric Aircraft with Aft Boundary Layer Propulsion (STARC-ABL) that uses two turbofan engines [31]. Also, NASA N3-X, a bigger hybrid wing body shape with trailing edge distributed turboelectric propulsion, offers numerous advantages, including lower fuel usage and noise emissions [33]. NASA has also created the agency's University Leadership Initiative (ULI). To enter service in the 2030s, a 76-passenger hybrid-turboelectric regional jet is being developed by a group of universities working together. Still, another group working with NASA is the ESAero (Empirical Systems Aerospace). ESAero is refining a turboelectric airliner design for NASA, the ECO-150R, a "split-wing" turboelectric system, which has 2 generators and 16 motor driven fans embedded in the wing [40].

NASA's X-57 'Maxwell' is the agency's first all electric experimental aircraft. Twelve high-lift fixed-pitch propellers are positioned upstream of the wing leading edge to increase lift at low speeds by accelerating

the flow [41]. As a completely electric experimental aircraft, the X-57 will be powered by lithium-ion batteries [35]. Moreover, Eviation, an Israeli company, is designing the nine-passenger ”Alice” concept. The Alice is equipped with two pusher propellers positioned at the wingtips and a tail-cone propeller, where BLI is claimed [34]. Airbus had also entered on the all electric discussion topic. The VoltAir was heavily promoted in popular media, but only one conference article (with minimum design definition) appears to have emerged [6, 36]. The structure was designed for natural laminar flow over the wing and featured a rear-mounted BLI propulsor. No further development is documented.

It is important to note that regardless of the HEP solution, there are thermal management issues due to the increase in electrical components. Furthermore, the lower thermal conductivity of light-weight composite structures when compared to conventional metallic structures aggravates this [42]. These are the main drivers for the development of novel TMS architectures which is the main focus of this work.

2.1.2 Alternative fuels

Besides all the efforts that have been done to develop HEP architectures, low-carbon fuels have also been considered over the past years to achieve the decarbonisation goals set for the industry. There is no globally recognised definition of sustainable aviation fuel. Although it is most often used to describe drop-in kerosene alternatives [43], ICAO defines SAF as alternative aviation fuels that fulfil stated sustainability requirements [44]. In this work, SAF is connected with drop-in fuels, distinguishing it from hydrogen (another interesting alternative fuel) or electric propulsion. Using SAF has two main advantages. Firstly, the aviation industry offers certain technological benefits for the deployment of drop-in fuels due to the high degree of uniformity across current aircraft, engines, and fuel standards. Secondly, life cycle carbon emissions can be reduced [45].

Currently, alternative fuels account for a negligible portion of aviation fuel, but their commercialisation is progressing well. There are several potential approaches to derive renewable drop-in kerosene from various raw materials and technological pathways. Bringing new fuels on passenger planes involves a long and costly ASTM (American Society for Testing and Materials) certification process. Until today, ASTM has certified 8 conversion pathways including Fischer-Tropsch hydroprocessed Synthesized Paraffinic Kerosene (FT-SPK), Synthesized Paraffinic Kerosene produced from Hydroprocessed Esters and Fatty Acids (HEFA-SPK) and Alcohol-to-Jet Synthetic Paraffinic Kerosene (ATJ-SPK). Increasing global SAF production also demands huge industrial expenditures since SAF production cost is still not economically competitive with the conventional aircraft fuel [46]. Another generation of fuels that do not require the destruction of biomass is the electrofuel. Electrofuels are potential future carbon-based fuels produced from carbon dioxide (CO_2) and water using electricity as the primary source of energy [47]. Renewable electrofuels can have very low greenhouse gas emissions, lower environmental risk than conventional and even advanced biofuel production, and may theoretically be generated in vast volumes. On the other hand, there are no effective regulatory models to guarantee environmental performance or drive industrial expansion and the cost of fuel production is likely to be several times higher than for biofuels, requiring a massive investment in additional renewable electricity generation and electricity systems [48].

The ultimate and long-term goal for alternative fuel is hydrogen. Hydrogen might be a viable option due to its potential advantages of zero-carbon emissions and noise reduction resulting from a cleaner combustion [49]. However, using hydrogen would require huge modifications to aircraft design and fuelling infrastructure. It has a far greater gravimetric energy density than kerosene, but an order of magnitude lower volumetric energy density [50]. This way, the airframe must be redesigned to accommodate bigger tanks necessary for storage [51]. Another challenge would be on the thermal management topic. Hydrogen has a very low boiling point that may result in storage boil-off or OH radicals that produce a greenhouse gas [9]. The integration of hydrogen is thus a challenging but not completely unfeasible goal for the mid-term future. Related to that, the integration of Fuel Cells (FCs) in the aircraft power-plant is also being studied. Hydrogen FCs convert chemical energy into electrical energy, which might be used to power electrical devices on-board [9]. Again thermal management problems arise from the use of FC. Also, despite having a higher specific energy density than batteries due to hydrogen, FCs present a lower specific power density. As the specific power density is lower, its response to varying power demands is reduced, which is a major concern [52].

2.2 Theoretical overview of heat transfer technologies

The thermal management system will be responsible to control the temperature and heat generated by the HEP architecture components described above. It will act mostly in three steps [53]: heat acquisition at the heat source (Section 2.2.1), heat transfer to a specialised heat sink (Section 2.2.3), and heat rejection at the heat sink (Section 2.2.2). Figure 2.2 summarises some of the main thermal sources, thermal transport systems and thermal sinks in a hybrid-electric aircraft discussed in this section. This discussion ends with a brief summary of some new trends in heat transfer technologies (Section 2.2.4).

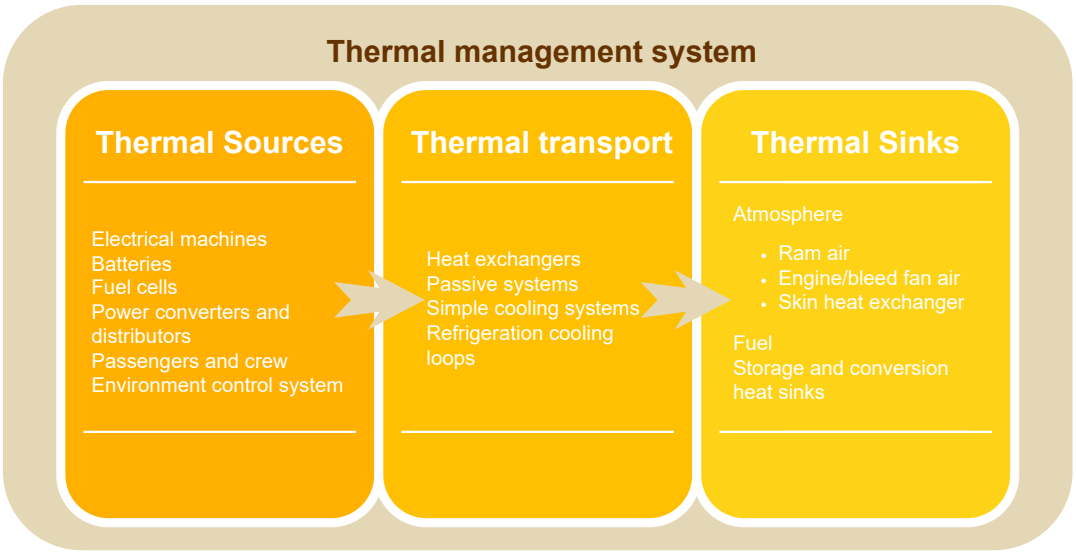

Figure 2.2: Thermal sources, transport systems and sinks, adapted from [11].

2.2.1 Thermal sources

Heat sources are not part of the thermal management system itself but understanding their behaviour is critical to the discussion since it affects the TMS needs. Any component or system that creates heat, either as a by-product of performing its function (e.g., waste heat created due to energy inefficiency) or as its primary purpose (e.g., cabin heaters or anti/de-icing systems), is referred to as a heat source [11]. Besides the main heat sources associated with typical aircraft systems, like combustion engines, mechanical power transmission and Environment Control System (ECS), the electrified propulsion systems are supposed to add considerable extra heat loads. The main electric powertrain heat sources may include:

- **Electrical machines** Motors and generators are responsible for producing electrical power. These machines are expected to be efficient, light-weighted and small. The traditional cooling methods use air cooling or oil cooling [54]. However, recent efforts are being made to develop superconducting electrical machines with cryogenic approaches, to increase the efficiency of these devices [55–57], which is discussed in Section 2.2.4.
- **Batteries** Batteries are used for electrical power storage. The battery pack optimal working temperature ranges between 20 and 50^{o}C. A good battery thermal management system is essential to ensure those values. Cooling techniques proposed to manage the battery temperature include mainly liquid cooling, air cooling, and Phase Change Materials (PCM) [58].
- **Fuel cells** Fuel cells store chemical energy and convert it into electricity by chemical reaction [59]. A hydrocarbon-powered FC emits CO_2 but it does not emit NO_x or other particulates. If fuelled with H_2, it becomes a carbon free source of generation as discussed in Section 2.1.2. The amount of heat created inside the cell as a result of exothermic processes, over-potentials, and irreversibility is significant [9]. Conventional cooling methods proposed include air cooling, liquid cooling and PCM cooling [60].
- **Power converters and distributors** Power conversion system translates electrical energy from Alternating Current (AC) sinks to AC sources via AC or DC (Direct Current) line, while the power distribution system is responsible for transporting the electrical power [61]. Although inverts and rectifiers have high efficiency, the heat generated must be removed through convection with air or with a liquid coolant. Regarding the cables used for electrical propulsion systems, convection (either natural or forced) with atmospheric air may be sufficient for cooling [11].

2.2.2 Thermal sinks

The thermal sink is the component that absorbs the unwanted heat that is released by the thermal sources. The most used terminal heat sinks to reject heat are the ambient atmospheric air and on-board fuel. These heat sinks have high technology readiness level in aircraft [12]. Other thermal accumulators, despite having lower TRLs, like PCM, thermoelectric and thermionic devices, are also topics of study in thermal sinks and their performance is being analysed in multiple studies.

Atmosphere

Atmospheric air can work as a heat load or a heat sink depending on the flight conditions and on the fluid temperature to be cooled. If the aeroplane is flying fast enough or if it is facing a hot day, the surrounding air will become a source of heat rather than a sink [11]. On the other hand, at low Mach numbers, the low air temperatures at high altitude enable ambient atmospheric air to be used largely as a heat sink. Atmospheric air heat sink can be used via Ram Air (RA), Engine Fan Air (EFA), and Skin Heat Exchanger (SHX) [62].

Ram air RA systems use the dynamic pressure caused by the movement of the aircraft to ingest air into a duct that can be charged directly to cool down the devices or can be transferred to Ram air Heat Exchangers (RHXs) to cool down fuel or a liquid coolant. Kellermann et al. [63] studied the effects of a ram air–based thermal management system on the fuel consumption of an aircraft using an expected TMS design drag and mass for a 180-passenger short-range partial-turboelectric aircraft. The study concluded that adding the RA TMS results in an increase in fuel consumption of 0.19% for an aeroplane having a 30% power split. With the aid of a tiny puller fan put behind the main heat exchanger, the system could endure hot-day take-off conditions. Oversizing the ram air TMS, on the other hand, eliminated the need for a puller fan but slightly raised the extra fuel consumption to 0.29%.

In ram air inlets, the air is brought to a halt relative to the aircraft which causes significant drag. To reduce the amount of drag experienced by the system, it is necessary to carefully consider the design of the flow inlet and outlet. Using submerged National Advisory Committee for Aeronautics (NACA) inlets [64] and taking advantage of the 'Meredith' effect are ways to reduce the amount of drag produced. Using the Meredith Effect, the system creates a jet of exhaust air, causing the aircraft to experience a forward reaction force, which helps to partially compensate the drag created [65]. Schiltgen et al. [40] did a research about a RA cooling system for the ESAero ECO-150R turboelectric aircraft introduced in Section 2.1 making use of the Meredith effect. The entire drag caused by the cooling system during the cruise accounted for around 2 to 3% of the total drag. The TMS with a RHX can be seen in Figure 2.3.

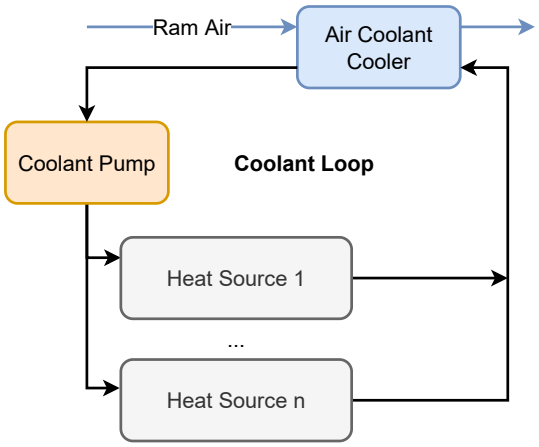

Figure 2.3: Thermal management system diagram using ram air, adapted from [40].

Engine/Bleed Fan Air EFA systems use compressed air taken from the compressor stage of a gas turbine mostly to cool down the downstream machinery components of the engine (e.g. turbine blades) or to maintain the temperature and pressure in the cabin. The use of fan air has increased mainly as a result of ongoing attempts to minimise or totally remove the apertures outside of the aircraft that ram air systems require [62]. Although the EFA system eliminates the RA drag penalty and frees up significant fuel volume, it has a lower cooling capacity. Since fan air has already been compressed in the engine fan, its temperature is higher than ram air, reducing the capacity of working as a heat sink. Furthermore, the pressure decrease caused by bleeding the fan air or introducing a heat exchanger into the fan stream adds a thrust penalty which results in a specific fuel consumption increase [11]. This might be a potential barrier to the development of this technology [66], one of the reasons why these EFA cooling systems will not be considered in this work.

Skin Heat Exchanger SHX system uses the existing aircraft surface as an alternative way to reach the atmosphere heat sink. It employs outside high altitude cold air flow and does not use intake air. For example, in A320 and B757, this cooling method successfully removes the heat produced by high-power electrical components without significantly reducing airplane performance [67]. The heated fluid (which might be oil, water, air, or other) comes into direct contact with the airframe skin, which, in turn, gets into contact with the ambient air through surface heat exchangers. This eliminates the need for air inlets, reducing the cooling drag associated with the RA systems.

This surface heat exchanger concept was first reported on the Curtiss Oriole in a 1922 stock plane race [68]. Although the concept was not widely used in commercial aircraft in the following years, the notion of heat transfer from the surface remained a topic of interest, especially in recent years with the increase of the hybridisation level in aircraft. Pang et al. [67] carried out an experimental prototype of an air/air-type skin heat exchanger for aircraft avionics to study its feasibility. They tested a plate-fin heat exchanger with a single layer fin presented in Figure 2.4 at two different positions on the fuselage skin. For position 1 (an unfavourable position where air flows in parallel with the skin heat exchanger), the range of global heat transfer coefficient obtained for a 1000 m and 0.9 Mach number flight was about 45–51 W/(m^2 °C). For Position 2 (a favourable position with a windward angle), the coefficient improved to $66 - 80$ W/ (m^2 °C).

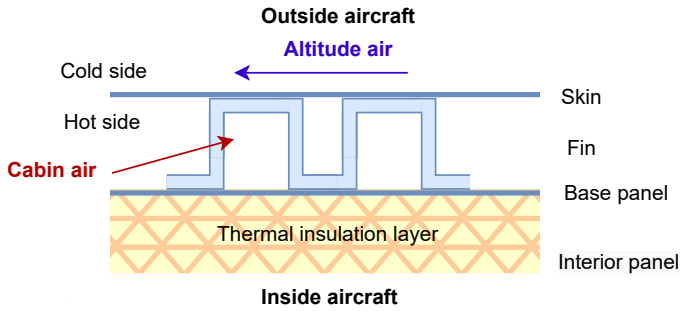

Figure 2.4: Air-air type skin heat exchanger experiment, adapted from [67].

Within NASA's High-Efficiency Electrified Aircraft Thermal Research (HEATheR) programme, the feasibility of the Outer Mould Line (OML) heat exchangers for electrified aircraft is computationally investigated for three different aircraft models (STARC-ABL, PEGASUS and RVLT Tiltwing) by Sozer et al. [69]. Computational fluid dynamics (CFD) study was used to examine the heat flux distribution across the aircraft OML at the surface temperature limit. For all three aircraft concepts, the heat rejection capacity was surprisingly consistent between take-off (or hover in the case of RVLT Tiltwing) and cruise conditions. The largest difference was noticed for the PEGASUS, whose heat rejection capability during the cruise was two times the rejection capability during the take-off. At cruising altitudes, the ambient air temperature is much lower than in a normal take-off scenario at sea level, yet at sea level, the higher air density promotes heat transmission. However, heat transmission is still limited during take-off (or hover) circumstances, particularly on a hot day. Also, Schnulo et al. [70] evaluated the influence of surface heat exchangers on the fuel consumption of the STARC-ABL concept with an upgraded power system and found that it decreased fuel consumption by an extra 0.8% and eliminated the complexity of the pumps and coolant system. However, this research showed that the OML cooling system is 112% heavier than the baseline TMS. Also, for the STARC-ABL concept, the wings and lower fuselage were identified as suitable regions for placing OML cooling.

Kellerman et al. [71] investigated the thermodynamic potential of the aircraft surface for a variety of air vehicles of various sizes. Maximum Take-Off Weight (MTOW) for different aircraft was related to the total surface area using a weak logarithmic correlation. For higher MTOW (larger aircraft) an increase in flow lengths on all surfaces is considered. All airframe area of the aircraft (A_{surf}) is used in this study, so the values are in an order of magnitude of 10^3 m^2. Using correlations between flat plates, the heat transmission was modelled. Four operational points were used to assess available heat transfer rate ($\dot{Q}_{\text{av}}$): Take-Off (TO), Hot day Take-Off (HTO), Climb (CL), and Cruise (CR). A variation of surface temperature (T_{surf}) between 320 K, 360 K and 400 K is also accounted in the parametric studies. The results showed that $\dot{Q}_{\text{av}}$ increases with MTOW, because A_{surf} increases. $\dot{Q}_{\text{av}}$ also increases for higher T_{surf} due to the higher temperature difference to the ambient. Over the entire MTOW range, $\dot{Q}_{\text{av}}$ is about twice as large for CR and CL compared to TO. The ratio even increases when comparing CR and CL to HTO. $\dot{Q}_{\text{av}}$ was the largest in CR with 7 MW for an A320-sized aircraft and a medium T_{surf} of 360 K. The most critical operating point was HTO with a $\dot{Q}_{\text{av}}$ of only 0.25 MW for the previously mentioned aircraft and T_{surf}. Furthermore, the findings of this paper suggest that heating aircraft surfaces might be used not just for heat dissipation but also for boundary layer control. When adding heat to an area of laminar flow, an increase in skin friction drag is anticipated. Besides, in areas of totally turbulent flow, the addition of heat lowers skin friction drag.

Fuel

Fuel is also a frequent heat sink, since it is abundant in aircraft and can be easily delivered to where it is required. Besides, hydrocarbon fuels have, in general, better heat transfer properties than air, making them a more effective cooling fluid [11]. At the same time, there is a thermodynamic advantage of preheating fuel before combustion resulting in a more efficient thermal cycle.

Despite this, there are some concerns and restrictions associated with fuel. Fuel stability is one of them. Thermal stability of a hydrocarbon-based fuel refers to its resistance from interacting with oxygen molecules dissolved. The development of deposits during heat exchange would have a direct effect on the operational safety of the aircraft [72]. Since the early 1970s, the industry has been studying options for solving this problem and enhancing the capabilities of fuel as a heat sink. Injecting chemical additives into the fuels, or employing deoxygenation systems reduces the amount of dissolved oxygen in the fuel and can increase the thermal stability [66]. Recently, some on-board fuel deoxygenation methods have also been investigated, such as membrane separation and chemical processes [73].

More electric aircraft development leads to less fuel available to reject heat. In the ultimate case of a fully electric aeroplane, no fuel will be available on-board. With this in mind, reducing heat loads from the fuel system itself, to prioritise external heat rejection, is also something to take into consideration. The fuel pumps are a common source of heat load in the fuel system. Donovan et al. [74] found that a variable displacement pump may give a much greater thermal margin (difference between fuel temperature and maximum permitted fuel temperature) than a centrifugal pump. There are also several factors to consider while designing and operating fuel tanks. It is possible to determine the maximum and lower fuel flammability limitations as stipulated by European Union Aviation Safety Agency (EASA) CS-25 regulations [75]. Fuel will inevitably reach its maximum permissible temperature if too much heat is transferred to it. The aeroplane has reached its ”thermal endurance” limit if this occurs. In this work, thermal endurance is defined as the duration it takes for the fuel temperature to reach its maximum in any area of a fuel-cooled aircraft. The thermal endurance of an aircraft that uses fuel as a heat sink will be less than or equal to a conventional aircraft [76]. Thus, in any research of thermal behaviour at the aircraft level, it is crucial to model the thermal concept of the fuel tank as well as the surrounding environment and system of heat sources throughout the whole mission [77]. Fuel tank different thermal modelling approaches that are being used in recent research are summarised in Table 2.2.

Table 2.2: Fuel tank thermal modelling approaches, adapted from [77].

Approach	Equations	References
Bulk one-dimensional steady-state	$\sum \dot{Q}_{loss} + \frac{\Delta T}{R} = 0$	[78]
Bulk one-dimensional transient	$\rho c_p V \frac{dT}{dt} = \sum \dot{Q}_{loss}$	[78–80]
Finite volume one-dimensional transient	$\left(\rho c_p V \frac{dT}{dt}\right)_i = \left(\sum \dot{Q}_{loss}\right)_{i+1,i-1}$	[81]
Three-dimensional heat diffusion CFD	$kV \frac{d^2T}{d^2(x,y,z)} + \dot{Q}_{loss} = \rho c_p V \frac{dT}{dt}$	[82]
Control volume with recirculation	$c_p \frac{d(mT)}{dt} = \dot{Q}_i + \dot{Q}_o + \dot{Q}_{loss}$	[76, 83–87]

In steady state and transient 1-D models, a fuel tank is partitioned into tank units. Upper and lower wall nodes can be considered to have the same temperature as the environment or tank walls may be considered with extra nodes and atmospheric nodes become boundary conditions [78–80]. A more comprehensive tank discretisation leads to a discrete finite element energy method [81]. In this case, to

estimate ullage and fuel surface area under various fill conditions, the fuel tank is assumed trapezoidal. Discretising the fuel volume in the span direction differentiates this model from 1D ones. Temperature distribution is achievable per element, rather than per-tank capacity. Using neighbouring fuel and structural volume elements, 1-D transient heat equations are solved for each element. Detailed CFD models of a wing fuel tank have also been carried [82]out. The key advantage of this computational method is that comprehensive 3D heat maps of the fluid and structure can be generated. However, the generation of results is computationally expensive and hence not ideal for preliminary simulation scenarios.

Another approach used in fuel tank modelling is to consider a control volume surrounding the tank with fuel recirculation in order to construct the governing differential equations for the fuel temperature and mass of fuel in the tank [76, 83–86]. The approach assumes that the liquid fuel inside the control container is well mixed and also indicates that incremental changes in the internal energy in the control volume are consistently distributed throughout the tank. The temperature of the fuel in the tank responds instantly and uniformly to changes in internal energy. Additionally, the work done by pressure at the inlet and outlet of the tank is negligible compared to the internal energy entering and leaving the tank [87].

The heat can be transmitted to the fuel in several ways. The heat can be transferred directly to the fuel in the tank or through a fuel system which includes several sources/sinks and fluid transportation elements: Fuel Thermal Management System (FTMS). A system-based approach of fuel thermal management, which is based on the mass and energy balance equations at each component/control volume, including the fuel tank, is going to be used in this work. In this context, the fuel tank modelling considering a control volume is also the most suitable. Extensive coverage of this approach has been brought out to the public in the last few years.

In the design proposed by German [83], more fuel is extracted from the tank ($\dot{m}_1$) than is required for propulsion ($\dot{m}_e$). Before being sent to the engine, the fuel collects heat ($\dot{Q}_{\text{heater}}$) from the heat-generating components. The excess fuel ($\dot{m}_r$) is then recirculated through a low-temperature heat exchanger rejecting heat ($\dot{Q}_{\text{cooler}}$) to the ambient environment before being returned to the tank. For each component of the system, transient mass and energy balance equations were formulated under the assumption that the physical properties of the fuel remained constant. German numerically integrated the governing equations to figure out how the fuel tank temperature changed over time under different flight conditions. The research concludes that the thermal endurance of the aircraft improved when the initial mass of fuel was increased. In numerous subsequent papers, the same generic design was numerically simulated using a system-level approach [76, 84, 85]. Doman began with the same set of governing equations as the previous study but incorporated the changes in ambient air temperature with altitude, and obtained an approximate analytical solution for predicting the cruising altitude that would maximise the fuel thermal endurance [84]. The scheme used for the aforementioned FTMS modelling is illustrated in Figure 2.5. A strategy for a dual-tank fuel thermal management architecture was subsequently proposed by the same research group. Huang also carried out an experimental work [88], where a dimensional analysis and water as a surrogate for the fuel are used to validate the theoretical results.

Pang et al. [89] extended German [83] analysis for a high-speed vehicle. Especially for these vehicles, such as supersonic aircraft, due to the combined impacts of airborne thermal load and aerodynamic

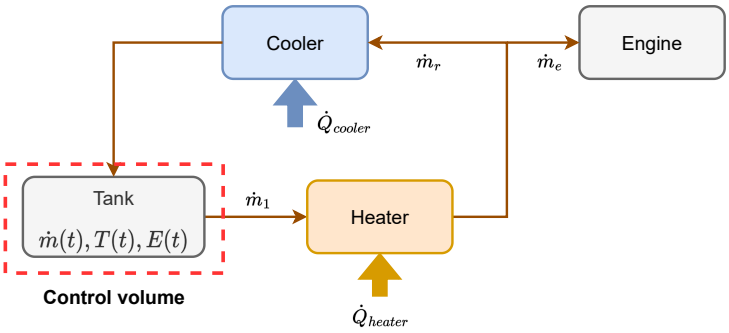

Figure 2.5: Block diagram of FTMS, adapted from [83, 84].

heating, the thermal endurance capacity of fuel will decrease as flight time increases. The modelling approach was similar to the one introduced by German, but this time considering the cumulative effect of aerodynamic heating on the fuselage and higher boundary layer temperatures.

In the same context, Aly et al. [86] studied four fuel thermal management system configurations. First, only a single tank and heat exchanger are considered. The second method recirculates surplus fuel back to the fuel tank, using a second heat exchanger to cool down the hot fuel. The third method is similar, but has a feed tank for recirculating fuel, so the main tank stays cooler. The last system recirculates fuel back into the main tank, but it also contains a feed tank where the fuel is stored before being utilised as a heat sink and burned in the main engine. The simple layouts show that recirculating hot fuel into a tiny reservoir is inefficient. Comparatively, moving hot recirculation fuel to a larger, unrestricted tank is a better way to handle thermal loads. The article forecasts that architectures with several fuel tanks and techniques to transport recirculated fuel to large tanks with reasonably cold fuel have the smallest thermal impact. Recently, Manna et al. [87] also developed a model of an aircraft thermal management in which fuel is cycled through heat dissipating/sourcing components. The modelling approach is similar to the one described above and an extensive parametric study is carried out to understand the influence of some designing parameters on the system efficiency. The model and results will be used in Section 3.4 to verify the FTMS developed in this thesis work.

It is easy to understand that to use fuel as a heat sink, many architectures can be employed, using single or dual recirculation tanks and different heaters and coolers layouts. In this context, Kellermann et al. [90] carried out a study to determine the potential of using fuel as a heat sink on a hybrid-electric model for 180 passengers, whose energy supplies are kerosene and Li-ion batteries. Two different layouts were taken into consideration: one with integrated fuel heat exchangers on the top and bottom surfaces of the wing (Concept 1) and one with conventional heat exchangers put inside the conventional fuel tank (Concept 2). Results showed that Concept 1 could provide the required cooling power in all mission points except for the Taxi case. The installed system added 120 kg of structural mass to the wings. In concept 2, the heat required to cool the devices could only be met in take-off. A reference cooler was also modelled as a compact cross-flow heat exchanger and ram air system with a NACA inlet. If no additional cooling fuel is needed, according to the trade studies, Concept 1 would have a fuel burn advantage when compared with the traditional RHX (fuel burn improvement of up to 0.6%).

Storage and conversion heat sinks

If waste heat could be saved or turned into energy of a more usable kind, such as work, this would be a good use. Although storage and conversion heat sinks are out of this project scope, a brief description of the main technologies studied for TMS integration is presented in Table 2.3.

Table 2.3: Storage and conversion heat sinks.

Heat sinks	**Description**	**TRL** [12]
Phase Changing Materials	Materials that have the ability to release or absorb energy during the phase transition stage, providing heat or cooling. Useful for infrequent peak loads. May be suitable for a battery thermal system. Low thermal efficiency, volume expansion, and liquid leakage after melting could be an issue [91].	4-6
Thermoelectric sink	Devices that produce electricity from heat via the Seebeck effect or absorb heat via the Peltier effect when a voltage is applied across them [92].	3-4
Caloric materials	Materials that utilising magnetic, electric, or mechanical forces, provide cooling effects [93].	2-3
Thermionic converters	Heat engine that transforms thermal energy directly into electrical energy. The energy source is heat, and the working fluid is the electron [94].	$\leq$3

2.2.3 Thermal transport systems

Heat Exchangers In order to transfer heat from one process fluid to another, a Heat Exchanger (HEX) is used. Although these devices are well established and widely used in engineering systems, there is still a great deal of investigation on how to enhance their efficiency, reduce weight, increase compactness and improve manufacturing techniques, especially in the aerospace sector. Compact heat exchangers are frequently used in the aviation industry [95]. It is a common practice to optimise heat exchangers by maximising thermal conductance in a given volume, while simultaneously minimising resistance to fluid flow. Heat exchangers with enhanced surfaces, or fins, can achieve high thermal performance with reduced parasitic power consumption [96]. Single and multiple pass cross-flow and counter-flow configurations are employed to increase heat transfer surface area per unit volume and therefore reach higher densities. For example, in the aerospace field, compact brazed shell-and-tube units are produced for the task of oil cooling, which is frequently paired with fuel preheating. It is also usual to implement plate-fin units using ram air for the aircraft environmental control. The demand in the aerospace industry for heat exchangers is notoriously high, involving delicate compromises between a conflicting design and performance factors across a wide range of operating situations [97]. In some cases, heat exchangers need to be manufactured in unique designs that will help them fit into confined and asymmetrical surfaces (Section 2.2.4). Because of these stringent requirements and lower production rates, the price is often considerable [98].

Passive systems Passive heat transmission components are devices like heat pipes, thermosyphons, and vapour chambers. Heat pipes are closed, sealed systems with a porous wick soaked in a working fluid and a hollow centre in the pipe element. In this system, the fluid turns into vapour when heat is taken in at one end of the pipe. The vapour moves down the hollow middle of the pipe. Then, the vapour cools at the cold end and turns back into liquid, which flows back to the wick. The difference between a thermosyphon and a heat pipe is that the working fluid in the thermosyphon is moved by gravity and natural convection and does not have wicks. Using vapour chambers, which are like heat pipes, enables to move heat in two or three dimensions [99]. The use of passive transport components has a lot of benefits, such as not having any moving parts, being easy to maintain, and not needing any energy to work. They work well for ”federalised” local cooling and can be used in aviation systems for cooling avionics, electromechanical actuators, and de-icing and anti-icing systems [100, 101]. However, designing a heat pipe is hard since its performance depends on how it is oriented and also because it can only move over short distances (3 m) [12]. Although these passive transport components have already been used in aircraft (TRL $\geq$7) [12], they will not be considered as part of the TMS architectures modelled in this work.

Simple liquid/gas cooling loops Closed or semi-closed loop cycles that only require pumping or blowing a liquid or gas, as well as heat acquisition at the source and heat rejection at the sink. Air and liquid cooling loops in aviation are at a very advanced stage of technological readiness since they are easy to implement and do not consider significant phase change [11, 17].

Refrigeration cooling loops The air-standard refrigeration cycle (Brayton) and its many variants are widely used in aircraft environmental control systems [11]. Vapour Compression Systems (VCSs) are also used in refrigeration cycles in general cooling systems but not so often as Brayton cycles. VCSs are significantly more efficient than air cycles, although they have several drawbacks that make them less practical. These include a high mass and a low maximum allowable operating temperature [11]. Nevertheless, this technology has a high TRL in aviation [12] and is going to be used in some architectures developed in this work.

2.2.4 New trends in heat transfer technologies

In recent years, new thermal management solutions for more electric aircraft have been developed and investigated as the expertise of such aircraft has increased. Many of these solutions are not yet ready for implementation. Nonetheless, some of them have already demonstrated considerable promise at low TRLs, including additive manufacturing, nanofluids coolants, superconducting devices and cryogenic coolers.

Additive manufacturing builds a part by adding material layer by layer, which means that less material is wasted. Programming-controlled environment makes the realisation of complex heat exchangers Computer-Aided Designs (CADs) possible. Also, the whole part can be made in a single piece. This indicates that the individual parts do not have to be made separately like in the traditional processes,

so leakage problems can be mitigated [102]. Research on fluids for thermal management to increase the cooling effectiveness is also an important topic and many recent studies have aimed to determine whether **nanofluids** may be used as a substitute for the conventional coolants or not. Nanofluids, which are composed of nanoparticles suspended in base fluids, may offer superior thermal conductivity and heat transfer performance when compared to conventional coolants such as water and ethylene-glycol [103]. The increased overall heat flow rate in the presence of nanoparticle concentrations is due to a higher collision rate between nanoparticles and heat exchanger channel walls. Another important discussion topic to highlight is the use of **superconducting devices and cryogenic coolers**. Using high-temperature superconductors in electric machines or cables could reduce the size and voltage requirements of such components due to their high current carrying capacity [55]. The liquid state of hydrogen has a cryogenic temperature of 20-25 K, which permits its use to cool superconducting electrical devices [56]. When these components are cooled with liquid hydrogen, the evaporated hydrogen can be used to generate electricity (fuel cells). Therefore, using liquid hydrogen can help to cool the superconducting machines and, at the same time, create power reducing CO_2 emissions and improving engine performance. However, the space required to store the liquid hydrogen in the airplane is limited as discussed in Section 2.1. Thus, cryogenic technology for aircraft propulsion is unlikely to be available within 30 years [57].

2.3 Theoretical overview of research TMS architectures

Most of the technologies described in Section 2.2 are used in the current research on thermal management for electrified aircraft propulsion. Since the TMS represents a huge design challenge to enable future HEP in commercial aviation, many efforts have been carried out to integrate these two systems. Some of the most recent and relevant studies are covered in more detail in this section.

2.3.1 NASA University Leadership Initiative program

As stated in Section 2.1, a 76-passenger hybrid-turboelectric regional jet to enter service in the 2030s is being developed by a group of universities working together under NASA's ULI program [10, 104]. Since thermal management is revealed to be a critical difficulty for electric propulsion implementation, the ULI program has also focused attention on the development of these systems. The electric propulsion system design of this study is comprised of eight Integrated Motor Drives (IMD) that are powered by two generators and one battery.

The research group [10, 104] proposed two different thermal management systems. One is for the IMDs of the wing (inverter and motor) and the other is for the energy storage system (battery). Each IMD will be cooled by a fan-ducted air-cooled oil cooler, while the cooling of the battery module is done by integrating it with the existing environmental control system, so that any surplus air cooling capacity from the ECS could be exploited. The oil selected for the oil cooling loop was Polyalphaolefin (PAO). In spite of the high thermal inertia of the battery, the authors determined that the current ECS is sufficient to keep

the battery below the temperature limit if it operates at maximum speed throughout the entire flight. While this eliminates the weight the penalty (ECS is already part of the aircraft), the increased engine bleed air and ram air required to run it at maximum speed does result in a 1.4% increase in the block fuel burn. Figure 2.6 shows the full TMS.

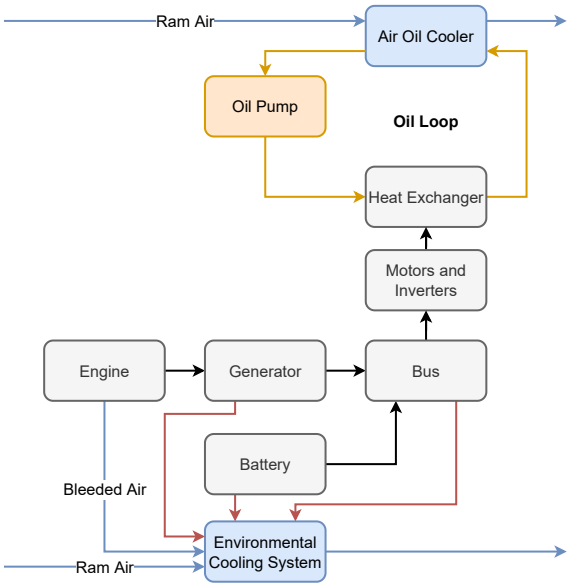

Figure 2.6: ULI aircraft proposed cooling system, adapted from [10, 104].

Shi et al. [105] continued this work by updating the TMS since it was recognised that the system may not be able to remove all the heat generated from the inverter and the motor during take-off and climb. This research proposed two solutions: (1) use extra PAO to absorb the excess heat not removed; (2) use a phase changing material, namely magnesium chloride hexahydrate and Urea-KCL. The work concluded that TMS with additional PAO has the largest weight and block fuel burn penalties since the large latent heat of the PCM makes it much lighter than PAO. Comparing the two TMS with PCMs, Urea-KCL presents a smaller weight penalty because it has larger latent heat and thermal conductivity.

2.3.2 NASA electrified aircraft programs

Chapman et al. [106] developed different thermal management systems for three NASA electrified aircraft propulsion concepts. The three vehicles are the STARC-ABL, RVLT tiltwing and PEGASUS, which have already been mentioned in Section 2.1. For sake of brevity, the RVLT tiltwing thermal management system will not be presented here since the VTOL aircraft concept is smaller and presents a rather different mission profile than the regional aircraft studied in the FutPrInt50 project.

For each concept, two power-plants and TMS systems were developed: a traditional one representing the state-of-the-art and an advanced one that accounts for electrical component technology progress. Baseline technology used a DC electric bus. The advanced electrified propulsion power system used a High Efficiency Megawatt Motor (HEMM), an efficient electrical transmission architecture and high efficiency converters. The HEMM worked with a superconducting rotor coil and cryogenic cooling to increase motor efficiency.

The STARC-ABL baseline TMS had an engine oil loop, rectifier loop, and BLI fan loop. The baseline generator was added to the engine oil cooling loop, which used engine bypass air and a fuel-to-oil cooler. The BLI fan motor and inverter were cooled using a propylene glycol mixture (PGW30). The fan air was only considered for cooling engine loop (Figure 2.7). The advanced TMS architecture is simple, with no oil loop, no rectifier load, and no engine air cooling loop (Figure 2.8).

Table 2.4 displays the simulation findings. They also simulated a corrected baseline TMS with the electric system only. In the advanced configuration, the coolant fluid was changed from PGW30 to Pure Silicone Fluid with a viscosity of 5cSt (PSF-5), reducing coolant specific heat and consequently increasing the required power due to PSF-5's higher viscosity. Despite the fact that the advanced TMS needs a greater amount of power than the reference, the weight and drag of the advanced TMS are one order of magnitude lower.

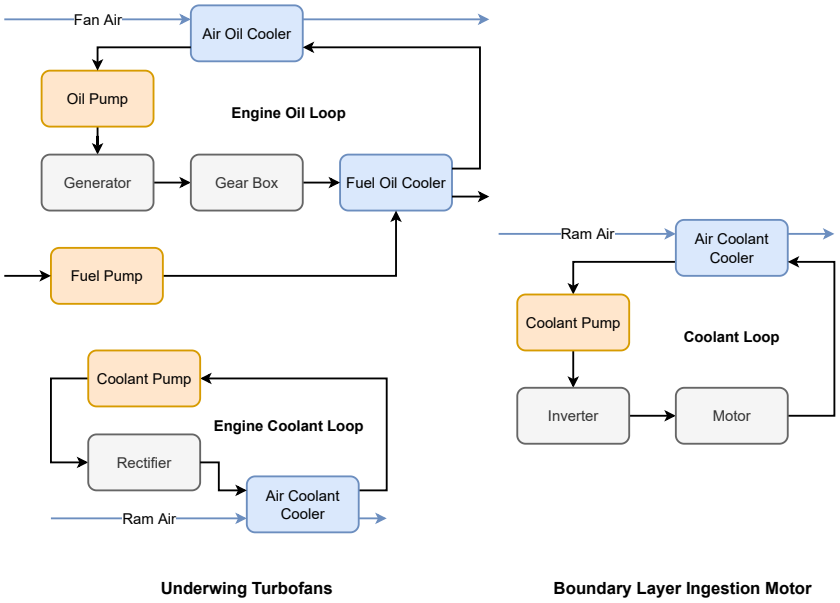

Figure 2.7: STARC-ABL baseline TMS architecture, adapted from [106].

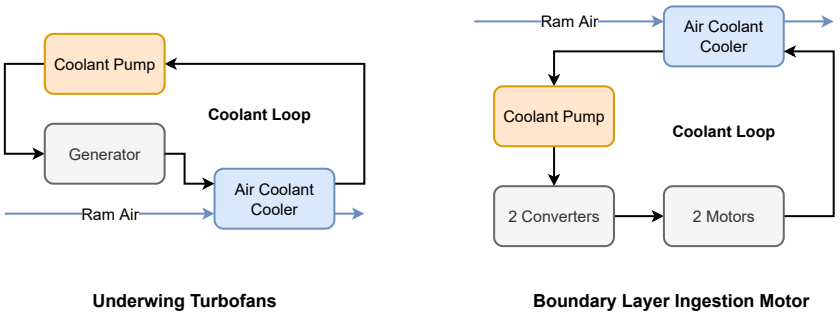

Figure 2.8: STARC-ABL advanced technology TMS architecture, adapted from [106].

Regarding PEGASUS, both baseline and enhanced designs for TMS were identical, since the battery was supplying DC power directly. The TMS design was modular, with two different types of loops. One contained an inverter and motor for the tip, inboard, and BLI components. While the other was only responsible for cooling the battery. PGW30 and PSF-5 were again used as coolants.

A 30% reduction in weight is achieved when comparing the advanced designs to the baseline, as seen in Table 2.4. Due to the higher viscosity of the coolant used in the advanced arrangement, more power is needed to run the TMS. However, the power consumption is still far below 1 kW. The decreased drag is in line with the need for less power rejection of the advanced configuration.

Table 2.4: TMS design metrics for NASA electrified aircraft, adapted from [106].

	Total TMS Loop	Baseline	Corrected Baseline	Advanced
STARC-ABL	Weight (kg)	197.97	109.33	50.77
	Power required (kW)	0.20	0.14	0.31
	Drag (lbf)	14.68	13.11	4.52
	Total TMS Loop	Baseline	Corrected Baseline	Advanced
PEGASUS	Weight (kg)	195.55	-	138.89
	Power required (kW)	0.22	-	0.30
	Drag (lbf)	17.64	-	12.67

2.3.3 Subsonic Single Aft eNgine

Recently, Heersema et al. [107] published a TMS study for the Subsonic Single Aft eNgine (SUSAN) Electrofan aircraft that is still ongoing. NASA's SUSAN is a concept for a 180-passenger regional aircraft that uses 20 MW of power with waste heat of the order of 1 MW [108]. The temperature limitations of the majority of electric components necessitate the rejection of waste heat at temperatures between 30 and 200 ^{o}C. Heersema et al. [107] projected three distinct thermal management loops that operate at temperatures appropriate for each thermal load. The first thermal management loop will service the battery system at a nominal temperature of 40 ^{o}C with outer mould line cooling. The second thermal management loop will service the electrical system at a nominal temperature of 60 ^{o}C. The electrical thermal management loop will be coupled with both an outer mould line surface heat exchanger and a liquid-ram air heat exchanger. The third thermal loop will serve the turbofan operating between 80 and 150 ^{o}C and consisting of a liquid-ram air heat exchanger and a fuel-liquid heat exchanger. The liquids used were PGW30 and PSF-50. Preliminary values for mass, power, and drag of conventional liquid/air heat exchangers were calculated. Also, by calculating the temperature of the fuel over the entire duration of the mission, the potential of using it as part of the TMS was evaluated. The preliminary conclusion drawn from this evaluation of the trade space is that none of the evaluated thermal management methods can realistically be used individually. A combination of methods will be required.

2.3.4 Summary of TMS research

A summary of the most relevant TMS architectures presented in this chapter for different heat transfer technologies is shown in Table 2.5, including the number of passengers and propulsion architecture.[1]

Table 2.5: Research TMS architectures.

Aircraft (Propulsion)	PAX	Cooling system	References
ECO-150R (TE)	150	Ram air and liquid	[40]
STARC-ABL (TE)	154	Engine fan air, ram air, fuel, liquid (oil+PGW30/PSF-5) and SHX	[69, 70, 106]
PEGASUS (PH)	48	Ram air, liquid (PGW30/PSF-5) and SHX	[69, 106]
SUSAN (TE)	180	Ram air, fuel, liquid (PGW30/PSF-5) and SHX	[107]
ULI (TE)	76	Ram air, PCM, ECS air and liquid (PAO)	[10, 104, 105]
Short-range aircraft (TE)	180	Ram air–based cooling system	[63]
Short-range aircraft (PH)	180	Fuel tank with internal heating and SHX	[90]

From this literature study, it is possible to draw the conclusion that several criteria influence the selection of TMS architecture design technologies. The kind of aircraft (hybrid or electric), the amount of heat produced/emitted by the various components, and the TRL of heat transfer technologies will all impact the performance and design of the TMS architecture.

Among all heat transfer systems with a greater TRL, liquid cooling, ram air cooling, outer mould line cooling, heat exchangers and using fuel as a heat sink are the most promising for TMS architectures. The majority of the TMS topologies researched for hypothetical aeroplanes presented in this literature overview are based on the technology of liquid-ram air cooling loops. This technique must be paired with a fluid that has a large thermal capacity, such as PAO, PGW30, or PSF-5 (and in the near future, nanofluids), in order to remove a substantial quantity of heat from the various components. This conclusion will be taken into account to build the thermal management system proposed in this work in Section 3.2.

[1] The FTMS proposed by several studies to a general aircraft can also be considered when designing the TMS [76, 83–87].

Chapter 3

Methodology

This chapter describes the development of the models and the simulation procedure. It starts by describing the reference aircraft and mission profile as well as the system requirements (Section 3.1). A general system description of the TMS architectures analysed is also provided in Section 3.2. Then, each component model for these architectures is documented in Section 3.3 and verified (comparing to reference data) in Section 3.4. The chapter concludes by presenting the simulation procedure (Section 3.5) as well as the optimisation model developed (Section 3.6).

3.1 Reference aircraft and mission

3.1.1 Hybrid-electric propulsion architecture

According to the architectures presented in Section 2.1, designing an air vehicle to be completely electric would result in no pollutant emissions during flight. However, due to the lower specific energy of the existing batteries when compared to conventional fuels, the range of such an aircraft would be very restricted [4]. A hybrid-electric idea addresses this problem by combining the benefits of both worlds, i.e. the range offered by conventional jets and the reduction of direct pollutant emissions by using an electrified engine with improved efficiency. For the purpose of assessing the possibilities of hybrid-electric propulsion, a reference aircraft design using sophisticated conventional technology was built within the scope of the FutPrInt50 project. The ATR42-600 was thought to represent the operational state of the art for this aircraft category [13]. Therefore, the reference configuration chosen is identical to the one implemented in the ATR42-600: a high wing, two turboprop engines beneath the wings, and a T-tail.

In the scope of the aforementioned project, several hybrid-electric architectures have been studied during this first phase of the project and the most promising ones can be surveyed in full detail in [109]. The base propulsion architecture used to design and size the thermal management system is a parallel hybrid architecture with two turboprop engines running on sustainable aviation fuel and coupled to an electric motor each. Powering the motors are also one or more battery packs. Wingtip propellers expand the power-plant and are powered by an electric motor and the battery packs. The power is managed by a Power Management and Distribution Unit (PMDU) and the fuel by a Fuel Management and Distribution

Unit (FMDU). Figure 3.1 illustrates this hybrid-electric design used for the TMS sizing [109]. The light grey elements serve as components that convert energy, such as motors, generators, gas turbines and fuel cells. Red lines and boxes stand for electric parts, such as cables, batteries and PMDU. The green elements represent all components that process chemical energy, such as the SAF tank, fuel lines and FMDU.

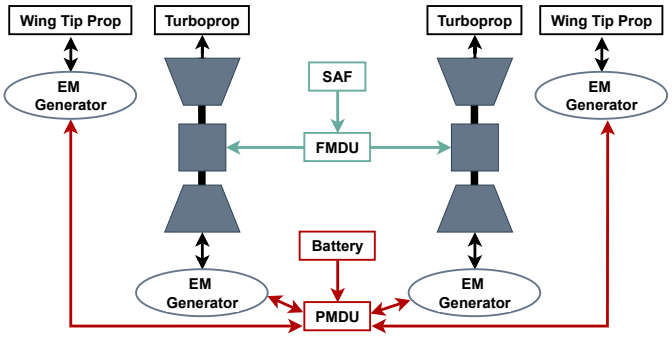

Figure 3.1: FutPrInt50 proposed HEP architecture, adapted from [109].

According to the [11], the TMS should be responsible to keep the batteries, motors, converters, and inverters, among other electric devices, in a certain temperature range. With this point in mind, an estimation of the total waste heat load created by these components and the temperature ranges that each component should operate was discussed. The minimum and maximum temperature reference values set during this phase of the project are presented in Table 3.1 [11] and the total heat load for each flight segment is shown in Table 3.2.

Table 3.1: Components temperature range.

Component	Max. temperature [°C]	Min. temperature [°C]	Nominal temperature [°C]
Battery packs	50-60	-20	25
Electric motor	120-180	-30	100
Power electronics	100	-20	50-70

Table 3.2: System heat load per mission segment.

Mission phase	Taxi-out	Take-off	Start/End Climb	Cruise	Descendent	Landing	Taxi-out
Heat load [kW]	119	237	119/147	88	0	197	119

The TMS will be designed to manage half of the total heat load according to the symmetry of the HEP architecture. To understand the total impact on the aircraft, the total mass, power consumption and the number of elements will be then multiplied by two. The estimations presented in Table 3.2 show that the critical heat waste load occurs during the take-off phase (237 kW). Since these heat load values are only initial guesses, a round number of 100 kW (200 kW/ 2) is considered as a generic heat load ($\dot{Q}_{equip}$) for the TMS sizing. In fact, considering the heat load as constant is a major important assumption, even if its value is conservative. However, having a constant heat load that needs to be managed makes it easier to figure out the different heat dissipation capacity of the components throughout the different stages of the

flight. The control temperature (T_{control}), i.e. the inlet liquid temperature on the heat load, will be limited by the battery pack since it has the lowest maximum allowable temperature. A value near the battery nominal temperature (305 K) is considered to guarantee the well-functioning of the component.

3.1.2 Top-level aircraft requirements and reference mission

FutPrInt50 defines close to 40 Top-Level Aircraft Requirements (TLARs) for a regional hybrid-electric 50-passenger aircraft in terms of flying performance, operational elements, market needs, environmental improvements, and regulatory standards [13]. The most relevant in the context of this work are presented in Table 3.3.

Table 3.3: TLRAs of FutPrInt50, adapted from [109] [110].

TLARs	Value/Range
Number of passengers	50
Maximum operating altitude	7620 m (25000 ft)
Design flight speed	450–550 km/h
Design range (design cruise speed, design payload)	400 km + reserve

The aircraft has a design range of 400 kilometres while carrying its full cargo. Additionally, reserves are designated as 185 kilometres and 30 minutes of extra holding [109]. According to project analyses, using a global flight database for the year 2019, this accounts for around 70% of regional turboprop flights within the European area [13]. As shown by the planned mission distance, the average length of a flight is rather short. Consequently, a design cruising speed of 450 to 550 km/h is specified. This is analogous to modern turboprop aircraft. Reducing this speed would eventually reduce the productivity of the aircraft by decreasing the number of daily flights. Moreover, FL 250[1] is defined as the maximum operating altitude, since for the typical turboprop mission duration of one hour, a higher cruise altitude is not required, as it will result in a longer climb segment. Figure 3.2(a) outlines a simplified mission profile for the reference flight without the alternate route. The cruise altitude was considered to be 7010 m. A velocity profile was also drawn for this mission as depicted in Figure 3.2(b) [111].

To obtain the performance of the design range mission by segment some assumptions were made taking into account some reference values of climb rate and fuel consumption of the baseline aircraft, i.e. the ATR42-600 [112]. Furthermore, a reserve fuel mass of 344 kg is also considered. The discussed values are presented in Table 3.4.

Table 3.4: Design range mission performance by segment.

Segment	Fuel [kg]	Time [min]	Distance [km]	Specific Range [km/kg]
Climb	148.1	14.6	87.4	0.590
Cruise	125.8	16.4	152.1	1.209
Descent	103.1	27.8	160.4	1.557
Total	**377**	**58.8**	**400**	**1.061**

[1] It is worth to note that FL stands for flight level and 250 denotes an altitude of 25000 ft.

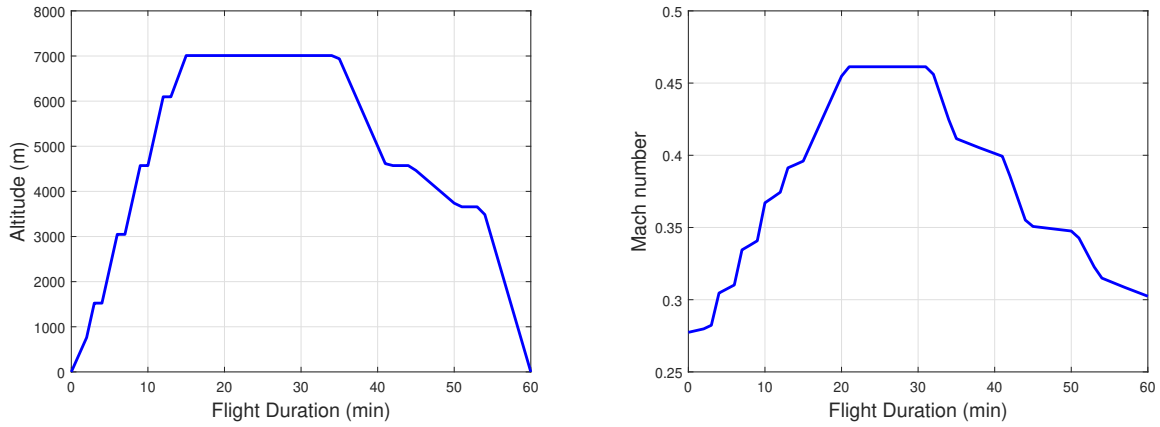

(a) Altitude. (b) Mach number.

Figure 3.2: Flight mission.

The components and systems precise location in the aircraft is still on study in this project phase. However, a first estimation of some general aircraft dimensional parameters was done, which will be important to obtain some reference measures for the fuel tank and system ducts. An overview of the aircraft initial outer mould line design and the relevant dimensions are presented, respectively, in Figure A.1 and Figure A.2 in Appendix A.1.

3.2 TMS architectures

Several TMS architectures inspired by some literature models presented in Section 2.3 were discussed during an initial phase of this work, within the scope of the FutPrInt50 project. With the intention of recurring to high TRL technologies and understanding if the current solutions can be applied to HEP, five schemes using liquid cooling, ram air, vapour systems and fuel are modelled. The choice of these technologies to integrate into the TMS systems enables a better estimation of the actual impact on the aircraft level. All five proposed architectures are presented in Figures 3.3, 3.4 and 3.5, following the same colour scheme.

In architecture 1, depicted in Figure 3.3(a), the heat is removed from the generic heat load by a liquid cooling cycle, outlined by the light blue arrows. The liquid is a mixture of 60% of Ethylene-Glycol and 40% of Water (EGW). The heat will then be transferred to a vapour compression system. The system is typically composed of an evaporator, compressor, condenser and expansion valve. The refrigerant used in the cycle, depicted by the orange arrows, is the R134a. Simply, R134a is heated on the evaporator, then compressed and cooled on the condenser by rejecting heat to the external air through an inlet (ram air, outlined by the dark blue arrows). Architecture 2, illustrated in Figure 3.3(b), is similar to architecture 1, only adding a skin heat exchanger, i.e. another heat rejection station before the evaporator. At the SHX, heat is rejected to the environment air through the aircraft surface. The remaining heat is transferred to the VCS and the following mechanism is the same as architecture 1.

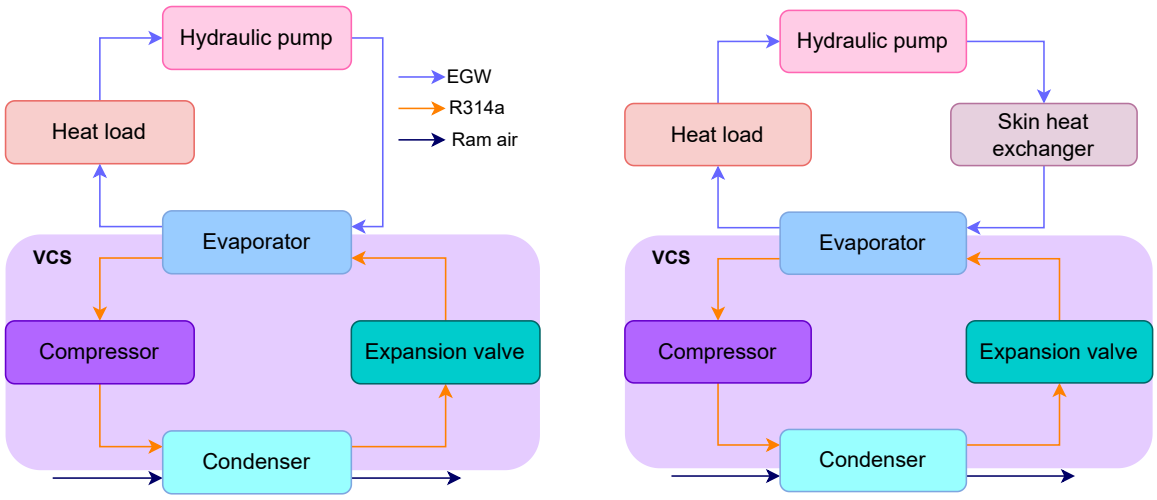

(a) Architecture 1 (A1). (b) Architecture 2 (A2).

Figure 3.3: Proposed TMS Architecture 1 (A1) and Architecture 2 (A2).

Both architectures 3 and 4, shown in Figure 3.4, only use liquid cooling and external air to reject the heat generated by the heat load. In architecture 3, the mixture of water and ethylene-glycol only transfers heat to a mass flow of ram air, while in architecture 4, the liquid passes first through the SHX, also rejecting heat to the air boundary layer.

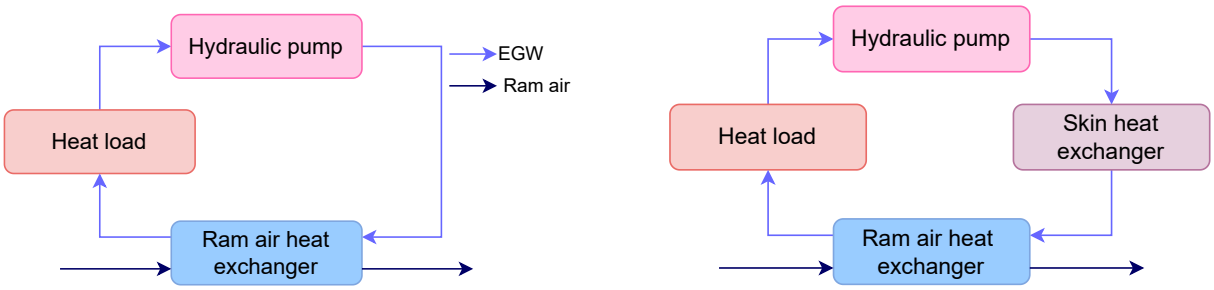

(a) Architecture 3 (A3). (b) Architecture 4 (A4).

Figure 3.4: Proposed TMS Architecture 3 (A3) and Architecture 4 (A4).

Architecture 5, presented in Figure 3.5, uses sustainable aviation fuel as a heat sink. Heat is again removed from the heat load by a liquid cooling cycle. This time, the heat is transferred to a Fuel Thermal System, via a Fuel Heat Exchanger (FHX) and the remaining to ram air, via a ram air heat exchanger. A mass flow of fuel leaves the tank to enter FHX where it collects heat from EGW. A proportioning valve splits the incoming fuel mass flow rate into an amount that is sent to the engine for combustion and propulsion purposes, and an amount that is recirculated back to the tank after it has rejected heat through SHX. The remaining heat is removed through ram air to ensure that the EGW temperature is controlled through the heat load.

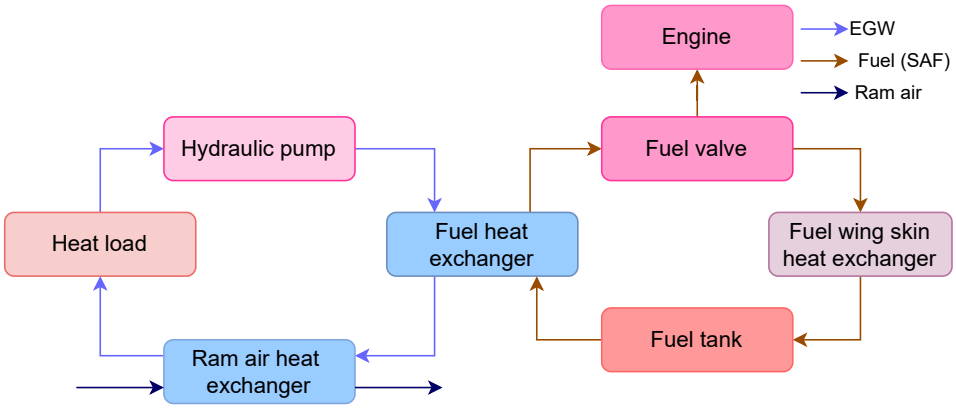

Figure 3.5: Proposed TMS Architecture 5 (A5).

3.3 Component model and formulation

This section covers the component level thermal/fluid modelling based on the TMS architectures presented in Section 3.2. The equations for thermal balance, pressure drop and mass estimation will be presented for each component. All model equations were created using Matlab/Simulink. It is worth to recall that the thermal management system is half-sized, so all the components should be duplicated in the aircraft system.

3.3.1 Heat load

Heat load represents all equipment to be cooled and is provided to the system as a heat transfer rate $\dot{Q}_{equip}$. The coolant outlet temperature can be calculated using the first law of thermodynamics (principle of conservation of energy) applied to a control volume with fluid crossing its boundary adapted to a simplified steady-flow thermal system [113]. The properties of the mixture of ethylene-glycol and water for different temperatures are obtained from tabulated data [114].

To calculate the required liquid mass flow rate, a norm from a SAE (Society of Automotive Engineers) report is used [115]. For liquid cooled avionics, flow rates range from 0.023 kg/s to 0.045 kg/s per kW (O_{liquid}) for coolants such as EGW mixtures. Due to the serial design of the liquid cooling loop, the mass flow rate of the coolant stays constant for each component. The numerical equations for the heat load and mass flow are given by:

$$\dot{Q}_{\text{equip}} = \dot{m}_{\text{liquid}} \cdot c_p \cdot (T_{\text{liquid},o} - T_{\text{liquid},i}) = \dot{m}_{\text{liquid}} \cdot c_p \cdot (T_{\text{liquid},o} - T_{\text{control}}) \tag{3.1}$$

$$\dot{m}_{\text{liquid}} = O_{\text{liquid}} \cdot \dot{Q}_{\text{equip}}, \tag{3.2}$$

where $\dot{Q}_{\text{equip}}$ represents the heat transfer rate from the heat load, T_{control} the maximum allowable temperature (305 K as aforementioned), $\dot{m}_{\text{liquid}}$ the liquid mass flow, c_p the specific heat at constant pressure and T the liquid temperature. The *i* and *o* subscripts distinguish between fluid entry and exit, respectively.

The liquid pressure drop across this stage is set to 5 kPa using project data (this parameter only influences the size and power consumption of the system hydraulic pump). The mass of the heat load that represents all the hybrid-electric propulsion sources is not considered in the thermal management system sizing since it is already accounted for in the power-plant design.

Figure 3.6 represents the steps of the heat modelling in sequential order.

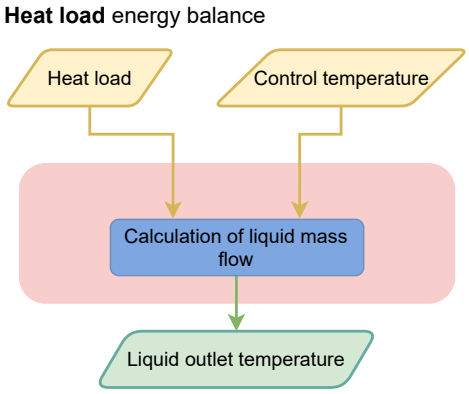

Figure 3.6: Heat load flowchart.

3.3.2 Liquid flow and ducts

Ducts are designed to transport fluid between two components. In this work context, circular aluminium pipes are used. Moreover, the duct surface is assumed to be adiabatic, so the coolant temperature is considered constant while the fluid is flowing through the duct. As a project input data, a maximum fluid velocity v_{liquid} of 2.5 m/s through the ducts is assumed. To calculate the ducts hydraulic diameter (D_h) so that the fluid reaches that velocity, the following equation is used:

$$D_h = \frac{4 \cdot \sqrt{A_{\text{crossducts}}}}{\pi} = \frac{4}{\pi} \cdot \sqrt{\frac{\dot{m}_{\text{liquid}}}{\rho_{\text{liquid}} \cdot v_{\text{liquid}}}}, \tag{3.3}$$

where ρ_{liquid} is the liquid density and $A_{\text{crossducts}}$ stands for the cross-sectional area of the ducts. The length (L) of the ducts is set and the value of its thickness (t) is also a system input, discussed in Chapter 4 in Table 4.2. The pressure drop throughout the system tells how much pumping power is needed. It is shown in Equation 3.4 that the pressure drop (Δp) for a routing duct is dependent on the length of the ducts, mass flow, hydraulic diameter and friction factor f [113].

$$\Delta p = \frac{8 \cdot L \cdot \dot{m}_{\text{liquid}}^2 \cdot f}{\rho \cdot \pi^2 \cdot D_h^2} \tag{3.4}$$

The friction factor is calculated using equations for different ranges of Reynolds (Re) values. This latter is a dimensionless parameter that correlates inertial and viscous loads considering a given length L (for this case, the hydraulic diameter), velocity v and fluid properties as follows:

$$Re_L = \frac{\rho \cdot v \cdot L}{\mu}, \tag{3.5}$$

where ρ and μ denote the considered fluid density and dynamic viscosity, respectively.

Petukhov came up with a correlation for a smooth surface that works for a wide range of Reynolds numbers Re_D [113]:

$$f = (0.790 \cdot \ln Re_D - 1.64)^{-2} \quad 3000 \leq Re_D \leq 5 \times 10^6. \tag{3.6}$$

The mass of the duct is calculated considering the geometrical parameters discussed above and the material density. Aluminium density is considered constant and equal to $\rho_{\text{al}} = 2780\, kg/m^3$. The total mass is given by $m_{\text{ducts}} = \rho_{\text{al}} \cdot \pi \cdot D_h \cdot L \cdot t$.

3.3.3 Pump

The ethylene-glycol and water mixture pump is designed to compensate for the entire pressure drop of the coolant as a result of its passage through the ducts, heat loads and heat sinks. Using an equation derived from the known value of pressure drop throughout the system (Δp), the fluid density and assuming a constant efficiency ($\eta_{\text{pump}} = 0.5$), the pump power may be estimated [116]:

$$W_{\text{pump}} = \frac{\dot{m}_{\text{liquid}} \cdot \Delta p}{\rho_{\text{liquid}} \cdot \eta_{\text{pump}}}. \tag{3.7}$$

Fluid temperatures are also examined as part of the pump model where $W_{\text{pump}} \cdot (1 - \eta_{\text{pump}})$ represents the heat loss from the pump to the working fluid (fuel or EGW mixture):

$$W_{\text{pump}} \cdot (1 - \eta_{\text{pump}}) = \dot{m}_{\text{liquid}} \cdot c_p \cdot (T_{\text{liquid},o} - T_{\text{liquid},i}). \tag{3.8}$$

Pump mass is calculated through a component regression curve relating the maximum liquid flow rate/power required to a weight value, using data from different global manufacturers. The component mass characteristic curve is presented in Figure A.4 in Appendix A.3.

The flowchart representing the hydraulic pump modelling is shown in Figure 3.7.

3.3.4 Heat exchangers

Two sorts of heat exchanger challenges are faced on a daily basis. On the one hand, there is the design challenge, where the temperatures and flow rates of the fluids entering the heat exchanger are specified, as are the intended hot or cold fluid exit temperatures. Subsequently, the issue with the design is then the choice of a certain kind of heat exchanger and its size. On the other hand, there is the performance challenge, where an existing heat exchanger may be used to estimate its performance. Additionally, the heat transfer rate and fluid output temperatures of the heat exchanger are measured and recorded [113]. In this conceptual phase, a numerical algorithm for heat exchangers is employed to calculate the outlet temperatures and the possible heat transfer rate transferred in each HEX using a performance approach.

The primary variables of a heat exchanger are its heat transfer rate $\dot{Q}_{\text{HEX}}$ [W], surface exchanger area

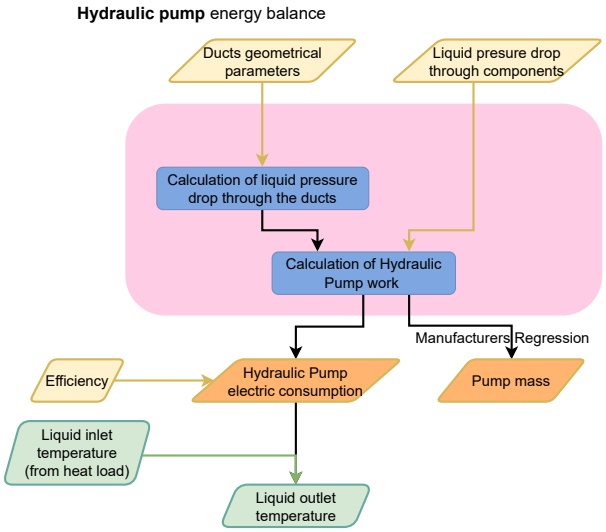

Figure 3.7: Hydraulic pump flowchart.

A_{HEX} [m^2], heat capacity rates $C(\dot{m} \cdot c_p)$ [W/K] and total heat transfer coefficient U [W/Km^2]. To determine the heat transfer rate, the first law of thermodynamics, in the same conditions as those presented in Section 3.3.1 (steady flow energy equation), is applied on hot and cold fluid sides:

$$\dot{Q}_{\text{HEX}} = \dot{m}_h \cdot c_{p,h} \cdot (T_{h,i} - T_{h,o}) \,, \tag{3.9}$$

and

$$\dot{Q}_{\text{HEX}} = \dot{m}_c \cdot c_{p,c} \cdot (T_{c,o} - T_{c,i}) \,, \tag{3.10}$$

where subscripts *h* and *c* distinguish between hot and cold fluids, respectively.

Newton's cooling law may be extended by using the global heat transfer coefficient U and an adequate mean temperature difference T_{lm} as follows:

$$\dot{Q}_{\text{HEX}} = U \cdot A_{\text{HEX}} \cdot \Delta T_{lm}. \tag{3.11}$$

In the above equation, the area A_{HEX} denotes the contact surface between a fluid and a wall; and it calls for the greater of the two areas when the areas on each side of the wall are different. It is worth mentioning that no correction factor was applied. The appropriate average temperature difference is a Log Mean Temperature Difference (LMTD) and the heat exchanger analysis may be performed using this approach [117]:

$$\Delta T_{\text{lm}} = \frac{\Delta T_2 - \Delta T_1}{\ln\left(\Delta T_2 / \Delta T_1\right)} = \frac{\Delta T_1 - \Delta T_2}{\ln\left(\Delta T_1 / \Delta T_2\right)}, \tag{3.12}$$

where ΔT_1 and ΔT_2 represent the terminal temperature differences between the two fluids. A counter-flow heat exchanger is chosen since it has a higher log mean temperature difference for identical intake and output temperatures than parallel flow HEX. For a counter-flow heat exchanger, the values of ΔT_1 and ΔT_2 are given by Equations 3.13.

$$\left[\begin{array}{l} \Delta T_1 \equiv T_{h,1} - T_{c,1} = T_{h,i} - T_{c,o} \\ \Delta T_2 \equiv T_{h,2} - T_{c,2} = T_{h,o} - T_{c,i} \end{array} \right]. \tag{3.13}$$

To design the ram air-EGW and fuel-EGW HEXs, a value of 10 K for ΔT_1 is used as a project design requirement. The influence of this design parameter will be taken into account in the optimisation design presented in Section 3.6. Even though some typical UA values could also be considered, the use of reference values of ΔT_1 between the two fluids that guarantee a good heat transfer rate is assumed a better approach since the impact of the HEX area and mass is a study topic. The three-equation system (Equations 3.9, 3.10, and 3.11) is then solved to obtain the heat transfer rate, the HEX conductance (UA_{HEX}), the outlet temperatures or the ram air mass flow required (RHX case).

For the mass estimation of heat exchangers in the conceptual phase, the total heat transfer surface area is needed. The detailed calculation of the global heat transfer coefficient was not considered in this project. Instead, reference overall heat transfer coefficients for the different flows [118, 119] are used. Using the result values of (UA_{HEX}) and reference U, the surface area can be estimated (A_{HEX}). Assuming compact heat exchangers [98, 120], their mass (m_{HEX}) and volume (V_{HEX}) are obtained according to the following equations, respectively:

$$m_{\text{HEX}} = \rho_{\text{HEX}} \cdot V_{\text{HEX}} \cdot (1 - \sigma)\,, \tag{3.14}$$

$$V_{\text{HEX}} = \frac{A_{\text{HEX}}}{\beta}. \tag{3.15}$$

In the above expressions, the porosity factor (σ) and surface density (β) values are estimated based on provided references. According to [95, 98], for FHX, aluminium shell-and-tube structures are ideal and frequently used in the aerospace sector for fuel preheating. Shell-and-tube exchangers can also be both compact and tiny and, in the aerospace sector, can reach surface density values up to 1500 m^2/m^3. For RHX, an aluminium plate-fin exchanger would be the most suited option since it is already used in environmental control exchangers. Plate-fin heat exchangers have typical porosity ranges of 0.6–0.75 depending on the alloy. The values described in Table 3.5 are the ones considered in the calculations.

Table 3.5: HEX design parameters [95, 98].

Heat Exchanger	Type	U [W/m^{2}K]	σ [-]	β [m^2/m^3]
FHX	Shell-tube	300	0.65	500
RHX	Plate-fin	500	0.65	800

In order to simplify the model and according to project data, the pressure drop is again not calculated in detail in this phase. The liquid flow pressure drop across the heat exchanger is considered constant and equal to 5 kPa.

Figure 3.8 represents the above described modelling procedure for both ram air-EGW and fuel-EGW heat exchangers.

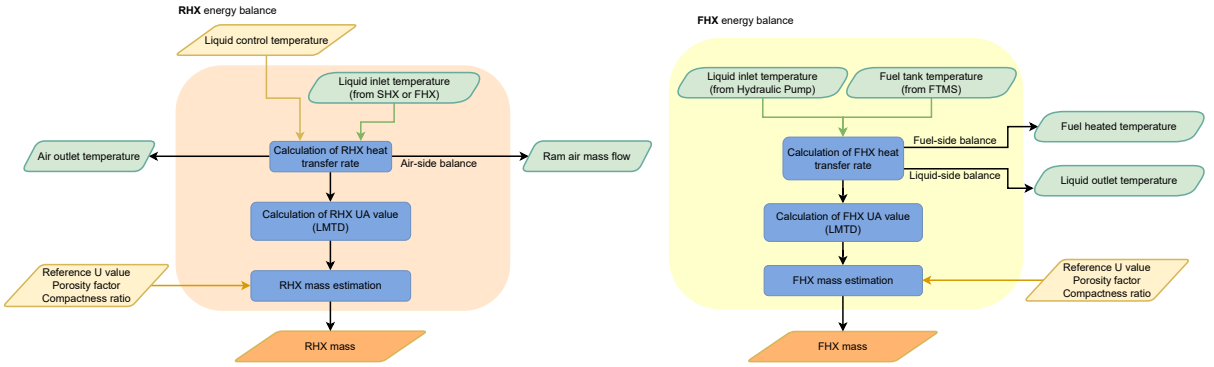

(a) RHX. (b) FHX.

Figure 3.8: Heat exchangers flowchart.

3.3.5 Ram air inlet/outlet

A ram air intake and an outtake are employed to gather the needed air flow and expel it to the ambient. The standard ideal isentropic relations are used to compute the ram air pressure and temperatures [121]:

$$T_{\text{ram,i}} = T_\infty \cdot \left(1 + \frac{\gamma - 1}{2} \cdot M_\infty^2\right), \tag{3.16}$$

$$p_{\text{ram,i}} = p_\infty \cdot \left(1 + \frac{\gamma - 1}{2} \cdot M_\infty^2\right)^{\frac{\gamma}{\gamma-1}}, \tag{3.17}$$

$$M_{\text{ram,o}} = \sqrt{\frac{2}{\gamma - 1}\left[\left(\frac{p_{\text{RHX,o}}}{p_\infty}\right)^{\frac{\gamma-1}{\gamma}} - 1\right]}, \tag{3.18}$$

$$T_{\text{ram,o}} = \frac{T_{\text{RHX,o}}}{1 + \frac{\gamma-1}{2} M_{\text{ram,o}}^2}, \tag{3.19}$$

$$v_{\text{ram,o}} = M_{\text{ram,o}} \cdot \sqrt{T_{\text{ram,o}} \cdot \gamma \cdot R}, \tag{3.20}$$

where $T_{\text{RHX,o}}$ and $p_{\text{RHX,o}}$ represent the air temperature and pressure, respectively, when exiting the ram air heat exchanger, γ is the ratio of specific heat (for air, γ = 1.4), R is the gas constant (287 J/kgK) and M_∞ is the Mach number of the aeroplane. The ambient static temperature T_∞ and pressure p_∞ are obtained using the International Standard Atmosphere (ISA) atmospheric model.

$T_{\text{RHX,o}}$ is calculated through the thermal balance previously described (Equations 3.9, 3.10, and 3.11). In what concerns the pressure estimation, a pressure increase of 1.5% passing through the fan and a pressure decrease of 3% passing through the heat exchanger are set as a project requirement for this kind of systems. The drag penalty for this system is estimated by Equation 3.21, where $\dot{m}_{\text{ramair}}$, η_n and $v_{\text{ram,o}}$ represent, ram air mass flow, nozzle efficiency coefficient and ram air outlet speed, respectively [120].

$$D = \dot{m}_{\text{ramair}} \cdot (\eta_n \cdot v_{\text{ram,o}}), \tag{3.21}$$

To get the drag coefficient C_D, the drag force is divided by the wing area A_{wing} and p_∞.

$$C_D = \frac{D}{A_{\text{wing}} \cdot p_\infty}. \tag{3.22}$$

Since a low-fidelity model is used to measure the ram drag, the system gives more of an indication of how much ram air the cooling system needs than a precise drag force impact. Nevertheless, the approach followed here yields a conservative drag estimation (without the Meredith effect). The approach applied to model the ram air inlet and outlet is described in the flowchart of Figure 3.9.

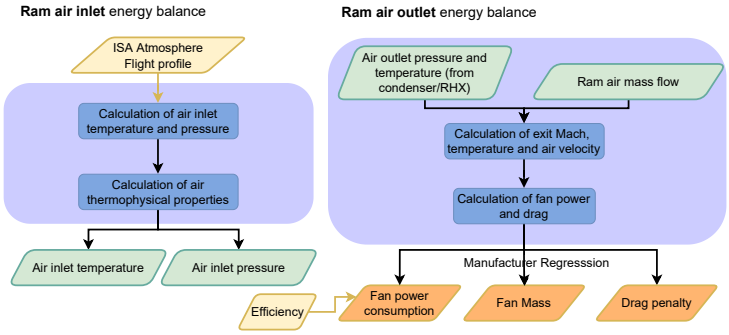

Figure 3.9: Ram air inlet and outlet flowchart.

3.3.6 Fan

To compensate for a lack of ram air created by the aircraft during take-off and landing, the fan is activated. In those phases, the fan will be responsible for increasing the air pressure by 1.5% and for ensuring the required ram air flows through the ram air heat exchanger. Similar to the hydraulic pump, the power electric consumption is given by:

$$W_{\text{fan}} = \frac{\dot{m}_{\text{ramair}} \cdot \Delta p}{\rho_{\text{ram,i}} \cdot \eta_{\text{fan}}}, \tag{3.23}$$

where η_{fan} is the fan efficiency. A usual value of fan efficiency of 0.5 is used in this phase. The ram air density is calculated through,

$$\rho_{\text{ram,i}} = \frac{p_{\text{ram,i}}}{R \cdot T_{\text{ram,i}}}. \tag{3.24}$$

The fan mass is calculated using the same approach as in the liquid pump and the regression curve is presented in Figure A.5 in Appendix A.3.

The fan modelling flowchart is similar to the hydraulic pump flowchart presented in Figure 3.7.

3.3.7 Vapour compression system

A vapour compression system is used for cooling the solution of ethylene-glycol and water in TMS Architectures 1 and 2. As mentioned before, the cycle working refrigerant is R314a. The properties of saturated and super-heated Refrigerant 134a are taken from Shapiro et al. [116]. As a common VCS, the

system is composed of an evaporator, a compressor, a condenser and an expansion valve, as portrayed in Figure 3.10. Each component is modelled by the principles introduced in [116].

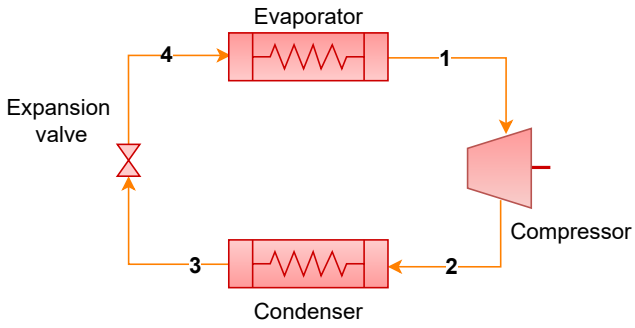

Figure 3.10: Vapour compression cycle.

As the refrigerant flows through the evaporator, heat transfer from the area being cooled causes the refrigerant to vaporise. For a control volume surrounding the refrigerant side of the evaporator, the heat transfer rate to the flowing refrigerant ($\dot{Q}_{\text{evap}}$) is given by:

$$\dot{Q}_{\text{evap}} = \dot{m}_{\text{ref}} \cdot (\text{h}_1 - \text{h}_4)\,, \tag{3.25}$$

where $\dot{m}_{\text{ref}}$ is the refrigerant mass flow and h is the enthalpy per unit mass at each stage. The refrigerant is then compressed, exiting the compressor to a relatively high pressure and temperature. Mass and energy rate balances for a compressor enclosing control volume produce the following formula for compressor work W_{comp} considering that there is no heat transfer:

$$(W_{\text{comp}})_{\text{isen}} = \dot{m}_{\text{ref}} \cdot (\text{h}_{2\text{isen}} - \text{h}_1) \tag{3.26}$$

where the subscript isen represents the state obtained by an isentropic evolution. The previous approach does not describe the actual compression performance. Irreversible compression must be considered. Considering an isentropic compressor efficiency η_{isen}, the irreversible compression is described by:

$$\eta_{\text{isen}} = \frac{(W_{\text{comp}})_{\text{isen}}}{(W_{\text{comp}})} = \frac{\text{h}_{2\text{isen}} - \text{h}_1}{\text{h}_2 - \text{h}_1} \tag{3.27}$$

The compressor electric consumption taking into account the equipment efficiency (η_{comp}) is given by $W_{\text{elect}} = W_{\text{comp}}/\eta_{\text{comp}}$.

The refrigerant then flows into the condenser, where the heat is transferred from the refrigerant to the surrounding colder environment (ram atmospheric air). The rate of heat transfer from the refrigerant to the ram air is presented as $\dot{Q}_{\text{cond}}$,

$$\dot{Q}_{\text{cond}} = W_{\text{comp}} + \dot{Q}_{\text{evap}} = \dot{m}_{\text{ref}} \cdot (\text{h}_2 - \text{h}_3)\,. \tag{3.28}$$

Finally, in state 3, the refrigerant enters the expansion valve and expands to the evaporator pressure.

This procedure is often depicted as a throttling procedure where:

$$h_3 = h_4. \tag{3.29}$$

In this irreversible adiabatic expansion process, the refrigerant pressure falls and there is an associated rise in specific entropy. At state 4, the refrigerant leaves the valve as a mixture of liquid and vapour at the evaporation reference temperature.

In a vapour compression system, net power input equals compressor power as the expansion valve has no input or output. Thus, the efficiency of the vapour compression refrigeration system is measured by the so-called Coefficient Of Performance (COP), given by:

$$\text{COP} = \frac{\dot{Q}_{\text{evap}}}{W_{\text{comp}}}. \tag{3.30}$$

Regarding the compressor mass, its estimated following the same approach as the hydraulic pumps: based on component typical regression curves. The data used is presented in Figure A.6 in Appendix A.3. The pressure drop of 5 kPa in each equipment is considered constant as previously described. To calculate the mass of the evaporator and condenser, as for the heat exchangers, Equations 3.14 and 3.15 are used. The evaporator is considered a shell-tube as the FHX and the condenser a plate-fin as the RHX. Typical values of heat transfer coefficient between the different fluids are again assumed [95, 98]. Table 3.6 summarises these considerations.

Table 3.6: Condenser and evaporator design parameters [95, 98].

Heat Exchanger	Type	U [W/m^{2}K]	σ [-]	β [m^2/m^3]
Evaporator	Shell-tube	450	0.65	500
Condenser	Plate-fin	450	0.65	800

Table 4.2 also presents the parameters used to size the VCS ducts. Finally, the vapour compression system flowchart used in this modelling is shown in Figure 3.11.

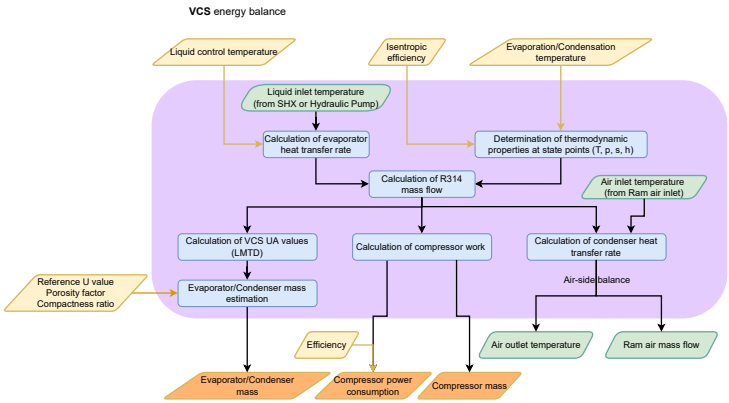

Figure 3.11: VCS flowchart.

3.3.8 Skin heat exchanger

The heat transferred through the skin heat exchanger, in similarity with the approach followed for the HEX, is given by:

$$\dot{Q}_{\text{SHX}} = U \cdot A_{\text{SHX}} \cdot \Delta T_{lm}. \tag{3.31}$$

Unlike the modelling approach of the HEX, where the UA values are determined, for the SHX modelling, the global heat transfer coefficient is calculated and the surface is a system input according to the available skin area of the aircraft (A_{SHX}). The global heat transfer coefficient neglecting the wall thermal resistance, radiation effects and fouling factors is defined in terms of convective individual heat transfer coefficients h_{ext} and h_{int}:

$$U = \frac{1}{\frac{1}{h_{\text{ext}}} + \frac{1}{h_{\text{int}}}}. \tag{3.32}$$

So the convection correlations for both internal and external flows to determine h_{int} and h_{ext} are respectively used.

Internal Flow

The Nusselt number Nu is the dimensionless surface temperature gradient and measures convective heat transfer. From the knowledge of Nu, it is possible to calculate the average convection coefficient h_{int}. For a circular tube, the relation between Nu_D and h_{int} is given by:

$$Nu_D = \frac{h_{\text{int}} \cdot D_h}{\kappa} = f\left(Re_D, Pr\right), \tag{3.33}$$

where κ is the thermal conductivity coefficient. For a given geometry, the Nusselt number must be some universal function of Reynolds Re_D, and Prandtl Pr numbers.

Considering a turbulent flow in circular tubes, Gnielinski provides a correlation for smooth tubes throughout a wide Reynolds number range, including the transition zone [113, 122]:

$$Nu_D = \frac{(f/8) \cdot (Re_D - 1000) \cdot Pr}{1 + 12.7 \cdot (f/8)^{1/2} \cdot \left(P_r^{2/3} - 1\right)}. \tag{3.34}$$

This correlation is valid for $0.5 \leq Pr \leq 2000$ and $3000 \leq Re_D \leq 5 \cdot 10^6$. The Reynolds and Prandtl numbers are calculated in steady-state conditions using the usual relations (Equations 3.35 and 3.5, respectively):

$$Pr = \frac{\mu \cdot c_p}{\kappa} \tag{3.35}$$

The fluid properties (constant pressure specific heat, viscosity and thermal conductivity) are considered constant besides the temperature variation and the friction factor is calculated using the relation presented in Equation 3.6.

External Flow

In order to calculate the external convective heat transfer coefficient, some considerations must be taken into account. During flight, cold ambient air adjacent to the outer surface of the aircraft increases in relation to the static temperature through ram effects [123]:

$$T_{aw} = T_{\infty} \cdot \left(1 + r \cdot \frac{\gamma - 1}{2} \cdot M_{\infty}^2\right), \tag{3.36}$$

The recovery factor for the turbulent boundary layer (r) is given by $r = Pr^{1/3}$, where Pr is the Prandtl number for air. It represents the fraction of total temperature recovered in the boundary layer as air molecules rest on the surface. T_{aw} is the adiabatic wall temperature.

Using a flat-plate analogy, the external heat transfer coefficient may be calculated at any location on the fuselage or wing, considering a Reynolds within $10^7 < \mathrm{Re}_x < 10^9$ [123]:

$$h_{\text{ext}} = \rho_{\infty} \cdot c_p \cdot v_{\infty} \cdot 0.185 \cdot (\log 10(Re_X))^{-2.584} \cdot Pr^{-2/3}, \tag{3.37}$$

where v_{∞} is the aeroplane airspeed and Re_X is the Reynolds number, considering X the distance along the fuselage/wing from its nose/leading edge to the point of interest. The thermophysical properties of the air (c_p, μ, and Pr) are obtained using the tables from [113]. ρ_{∞} and T_{∞} are again obtained by the ISA atmosphere model. The Reynolds number is calculated using Equation 3.5 and aeroplane velocity can be estimated by the following expression:

$$v_{\infty} = M\sqrt{\gamma R T_{\infty}}, \tag{3.38}$$

$\rho_{\infty}, v_{\infty}, \mu$ are evaluated at reference T^*:

$$T^* = \frac{T_{aw} + T_{\infty}}{2} + 0.22\,(T_{aw} - T_{\infty})\,. \tag{3.39}$$

Energy Balance

As described for the heat exchangers, after calculating the global heat transfer coefficient the following system of three non-linear equations is solved:

$$\begin{cases} \dot{Q}_{\text{SHX}} = \dot{m}_{\text{air}} \cdot c_p \cdot (T_{\text{air,o}} - T_{aw}) & \text{(air-side balance)} \\ \dot{Q}_{\text{SHX}} = \dot{m}_{\text{liquid}} \cdot c_p \cdot \left(T_{\text{liquid,i}} - T_{\text{liquid,o}}\right) & \text{(liquid-side balance)} \\ \dot{Q}_{\text{SHX}} = U \cdot A_{SHX} \cdot \Delta T_{\text{lm}} = U \cdot A_{SHX} \cdot \dfrac{\Delta T_2 - \Delta T_1}{\ln\left(\Delta T_2 / \Delta T_1\right)} & \text{(general balance)} \end{cases}, \tag{3.40}$$

where $\Delta T_1 = T_{\text{liquid,i}} - T_{\text{air,o}}$ and $\Delta T_2 = T_{\text{liquid,o}} - T_{aw}$.

The air mass flow that is heated passing through the aircraft surface is calculated by Equation 3.41:

$$\dot{m}_{\text{air}} = t_{bd} \cdot L_{\text{SHX}} \cdot v_{\infty} \cdot \rho_{\infty}, \tag{3.41}$$

where t_{bd} represents the air boundary layer thickness and L_{SHX} the flow characteristic length. The characteristic length is considered equal to the SHX area, assuming a unitary width (1 m) for the contact surface. For the boundary layer thickness, a reference value of 0.01 m is used as a project suggestion based on past experiments. Although this value is hard to predict due to the boundary layer chaotic behaviour, Pang et al. [67] also state that for actual flying conditions, the thermal boundary layer thickness of the air flowing through the aircraft skin is less than 0.05 m.

Mass

The impact of the structure mass of the skin heat exchanger is also an important topic in this study. The mass is calculated according to the experiment setup structure carried by Pang et al. [67], however considering circular ducts instead of rectangular ones. The SHX is considered to be an aluminium block with 7.6 mm of thickness and face area equal to the area considered as an input in the SHX system (A_{SHX}). The block also has circular tubes with a diameter of 6 mm and with a surface area equal to half of the SHX area ($A_{\text{SHX}}/2$). The total skin heat exchanger volume is obtained by subtracting the volume of the channel from the block volume, as:

$$V_{SHX} = \left(A_{\text{SHX}} \cdot 7.6 \cdot 10^{-3}\right) - \left(\frac{A_{\text{SHX}}}{2} \cdot \frac{6 \cdot 10^{-3}}{2}\right). \tag{3.42}$$

The mass of the skin heat exchanger may be estimated as $m_{\text{SHX}} = \rho_{\text{al}} \cdot V_{\text{SHX}}$. The aluminium density (ρ_{al}) is presumed constant and again equal to 2780 kg/m^3.

The model can be described by the flowchart shown in Figure 3.12.

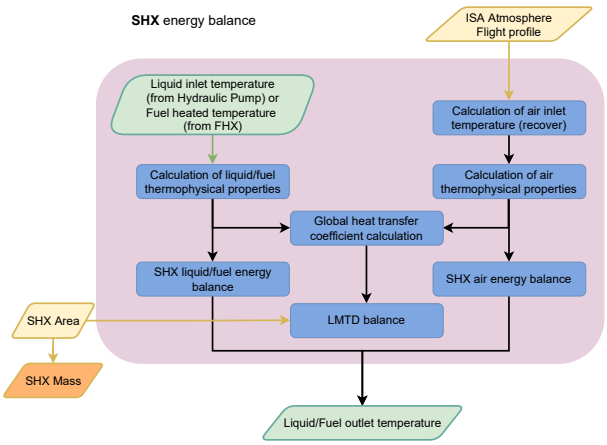

Figure 3.12: SHX flowchart.

3.3.9 Fuel system

The fuel system used for the thermal management in architecture 5 is presented in Figure 3.13 with all the nomenclatures used in the following explanation.

As discussed in Section 2.1.2, some proposed sustainable aviation fuels adhere to the exact specifications set forth in the ASTM D7566 standard. Gevo has created technology that integrates with and

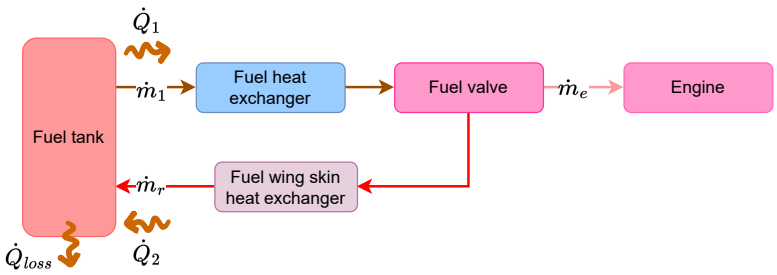

Figure 3.13: Fuel thermal management system.

makes use of the infrastructure already in place in the fermentation industry, such as ethanol production [124]. Alcohol-to-jet fuel produced by Gevo is derived from isobutanol, which may be produced in already-existing ethanol plants. The effectiveness of this strategy has already been proven by Gevo in a considerable number of airports throughout the globe. Not all sustainable aviation fuels integrate as well with infrastructure. This is the reason why a mixture of Gevo with Jet Propellant 8 is used in this phase. The properties of GEVO-JP-8 are taken from a US air force research laboratory report [125].

Fuel tank

The fuel tank can be modelled in several different ways depending on the application and the data that needs to be analysed. Different modelling approaches were presented in Table 2.2. Since the focus of this study is more on the energy balances and thermal interactions side, the fuel tank is modelled as a control volume with recirculation. The main governing equation of the fuel tank will be given by [87, 89]:

$$\frac{dE_{cv}}{dt} = \dot{Q}_2 - \dot{Q}_1 - \dot{Q}_{\text{loss}}. \tag{3.43}$$

The energy of the control volume may be represented using the following equation:

$$E_{cv} = m_T \cdot c_p \cdot (T_T - T^*)\,, \tag{3.44}$$

where T_T and m_T represent the instantaneous temperature and mass of the fuel in the tank, respectively. T^* is a reference temperature and c_p is again the constant pressure specific heat of the fuel. At any given time, the temperature of the fuel coming out of the tank is the same temperature as the fuel inside the tank. The heat transfer rate $\dot{Q}_1$ is given by:

$$\dot{Q}_1 = \dot{m}_1 \cdot c_p \cdot (T_T - T^*)\,, \tag{3.45}$$

Additionally, $\dot{m}_1$ is the mass flow of fuel out of the fuel tank in kg/s that will change during the different flight phases (climb, cruise and descent), attending to the values of Table 3.4.

After going through the wing skin heat exchanger, the fuel enters the tank at a given temperature T_c. The heat transfer rate $\dot{Q}_2$ is given by:

$$\dot{Q}_2 = \dot{m}_r \cdot c_p \cdot (T_c - T^*)\,, \tag{3.46}$$

where $\dot{m}_r$ represents the recirculation fuel mass flow. Note that $\dot{m}_1 = \dot{m}_e + \dot{m}_r$, where $\dot{m}_e$ is the rate at which fuel is fed to the engine for propulsion purpose. $\dot{m}_e$ is related to the instantaneous fuel mass in the tank as follows:

$$\frac{dm_T}{dt} = -\dot{m}_e. \tag{3.47}$$

To calculate the heat loss of the fuel through the tank walls to the environment the following expression is used:

$$\dot{Q}_{\text{loss}} = U_{\text{wall}} \cdot A_{\text{wall}} \cdot (T_T - T_{aw}), \tag{3.48}$$

where U_{wall} measures the thermal resistance between the fuel all the way up to the ambient air. A reference project design value for U_{wall} of 40 W/(m^{2}K) is used. A_{wall} represents the portion of the tank wall both exposed to external flow and the fuel in m^2 and is estimated as follows:

$$A_{\text{wall}} = \frac{m}{m_{0,\max}} \cdot A_s + A_b. \tag{3.49}$$

Since the actual size of the tank is still unknown in this project phase, an estimation of the side wall area of the tank A_s and the tank bottom area A_b based on the geometrical parameters presented in Figure A.2 is carried out. Typically, a commercial aircraft presents a tank up to 85% of wing-span (b) [126], within a wing-box confined between 12% and 71% of chord (c) [127] and has a thickness to chord ratio of around 14% [128]. In this work, the fuel tank is assumed to go up to 70% of the wing span with a width of 25% of the chord. These values are used in the following calculations:

$$\begin{aligned} A_s &= (0.7 \times \tfrac{b}{2}) \times (0.14 \times c) = 2.8298\text{m}^2, \\ A_b &= (0.7 \times \tfrac{b}{2}) \times (0.25 \times c) = 5.0531\text{m}^2. \end{aligned} \tag{3.50}$$

The final fuel tank balance equation results in:

$$\frac{d\left(m_T \cdot c_p \cdot (T_T - T^*)\right)}{dt} = \dot{m}_r \cdot c_p \cdot (T_c - T^*) - \dot{m}_1 \cdot c_p \cdot (T_T - T^*) - U_{\text{wall}} \cdot A_{\text{wall}} \cdot (T_T - T_{aw}). \tag{3.51}$$

The fuel tank mass is not considered in this phase since it is already integrated into the airborne power-plant design.

Fuel-EGW heat exchanger and fuel skin heat exchanger

The fuel-EGW heat exchanger is a preheating stage for the fuel before engine combustion. The modelling of FHX was previously described in Section 3.3.4. The fuel wing SHX follows the same modelling approach as described in Section 3.3.8, just taking into consideration the internal fluid properties for fuel and a slightly different position for the SHX (i.e. different reference value of X and considering the leading edge as a reference flow for the flow length). Moreover, since the internal fluid has a lower thermal resistance and does not impact much on the global coefficient, the U value was considered to be 80% of the external convection coefficient ($0.8 \cdot h_{\text{ext}}$) [87]. The temperature of the heated fuel is referenced as T_h. The mass of fuel SHX is calculated using the equation presented in Section 3.3.8.

Fuel system lines and pump

The fuel pump of A5 is designed only to guarantee the recirculation of the fuel to the tank. The fuel pump responsible for the fuel line maintenance between the fuel tank and the engine is already part of the aircraft and it is not being taken into account when designing the TMS. With the focus on calculating the power consumption of the fuel pump, some typical pump data for an aircraft is considered, in particular, a reference pressure drop value ($\Delta p_{\text{pump}} = 1200\,\text{lb/in}^2$) and efficiency ($\eta_{\text{pump}} = 0.5$) [89]. Once again, the power consumption of the fuel is given by equation 3.7. The heating of the fuel due to pump inefficiency is given by equation 3.8. To estimate the recirculation fuel pump mass, a regression curve presented in Figure A.7 in Appendix A.3, is used. The fuel lines are not taken into account in the mass estimation, since they are already incorporated in the mass of the aircraft structure. The FTMS flowchart is presented in Figure 3.14.

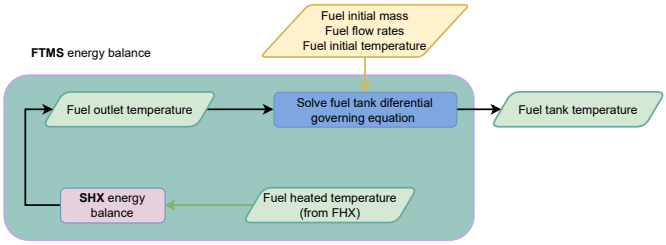

Figure 3.14: FTMS flowchart.

3.4 Component verification

3.4.1 Heat exchangers and VCS

The counter-flow heat exchanger described in Section 3.3.4 is verified through the typical hot and cold fluid temperature distributions associated with this type of HEX [113]. Considering steady-state conditions and constant properties, the temperature difference between the hot and cold fluids is obtained for a specific flight point.

The VCS is benchmarked using the temperature–entropy ($T - s$) diagram of an actual VCS [116] showing a good match.

3.4.2 Skin heat exchanger

The SHX modelling approach is similar to the one followed in the heat exchanger section. The main difference is that, in this phase, the global heat transfer coefficient is calculated through fluid and air flow properties. Since the external convection has more impact on the heat transfer, the calculation of the external heat transfer coefficient is the critical parameter in the modelling process. To calculate the heat transfer coefficient Equation 3.37 is used [123]. Since there is no public experimental data for the SHX external heat transfer coefficient, the only way to verify the model, is to use a different approach for the calculation of the heat transfer coefficient and compare it to the reference one. Mao et al. [62] presented a different equation in order to obtain h_{ext}. Additionally, another semi-empirical model, from Incropera et

al. [113], was included to compare with the implemented one and the one from the article. Applying the three equations to the project mission segment, the results presented in Figure 3.15 for the external heat transfer coefficient are obtained.

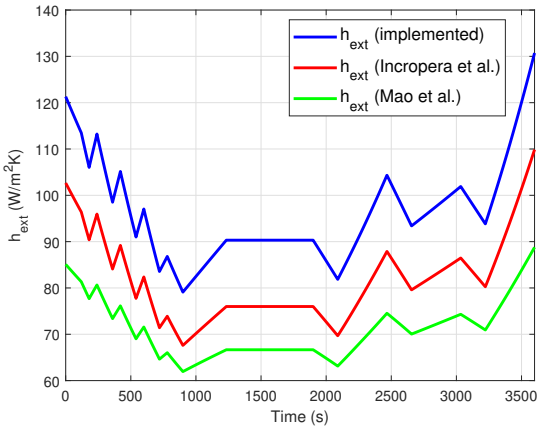

Figure 3.15: SHX external coefficient verification with semi-empirical expressions from Incropera et al. [113] and Mao et al. [62].

The difference between the three external coefficients during the whole mission is quite significant since these are distinct semi-empirical models that had different bases in the experimental evidence. It is also worth to note that the implemented model provides a higher heat transfer coefficient than the others, which can potentiate the SHX usage. Therefore, care should be taken in the future design stages to evaluate this coefficient with higher fidelity tools.

3.4.3 Fuel system

As described in Section 3.3.9, the fuel thermal management system is created based on the model developed by Manna et al. [87] combined with some details introduced by Pang et al. [89]. To verify the FTMS and as a first design phase, the model introduced by Manna was replicated. The system of FTMS is similar to the one proposed in the scope of this project. The main components are a fuel tank, with fuel at T_T inside; a high-temperature heat exchanger (heater) that represents the heat source rejecting heat at a rate $\dot{Q}_h$. At the outlet, the fuel is at a temperature of T_h, while the surface of the high-temperature heat exchanger is at T_{source}. A value for the heater conductance is assumed constant $U_h A_h$. The system also has a fuel valve and low temperature heat exchanger (cooler) at a temperature T_{sink} where the recirculation fuel passes through. The fuel temperature is T_c as it leaves the low temperature heat exchanger. A flat-plate model of the external surface of the cooler is used to determine its heat transfer coefficient.

Different modes of operation are considered in the study, but only mode 1 (constant heat sink temperature) was reproduced in this phase. The temperature curve results presented by Manna et al. [87] are shown in Figure 3.16(a). Compared to our design model, presented in Figure 3.13, the heater represents a simpler and equivalent fuel-EGW heat exchanger version; while the cooler is a similar wing skin heat exchanger version since it also considers a flat-plate with external flow to calculate

the global heat transfer coefficient. Given the fact that the method used for the calculation of the heat transfer coefficient is not detailed in the aforementioned article (missing data of the characteristic length considered to calculate the external Reynolds number and external heat transfer coefficient), the global heat transfer coefficient was calculated using the same method described by Equation 3.37. The enthalpy of the fuel, assumed to be Jet-A fuel, is obtained from a report which documents the library of thermodynamic data used by the NASA Glenn computer program CEA (Chemical Equilibrium with Applications) [129]. The results obtained are presented in Figure 3.16(b). The shape of the curves is similar in both plots. Although the difference is small, it can be possibly explained by the different global heat transfer coefficients considered in the cooler.

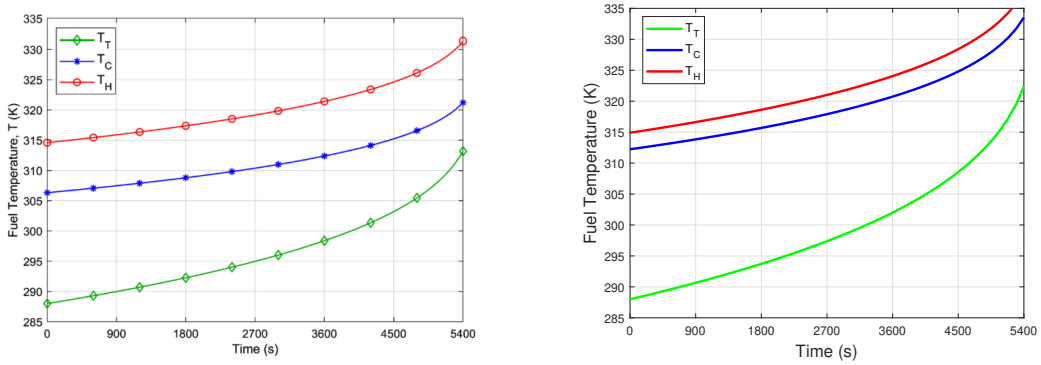

(a) Changes over time for the fuel temperature of the fuel thermal management system [87].

(b) Changes over time for the fuel temperature of the replicated fuel thermal management system.

Figure 3.16: FTMS verification.

3.5 Simulation procedure

The simulation is done using Simulink/Matlab interface with a simulation time of 3600s, representing the flight duration according to Figure 3.2(a). The architectures schemes are obtained by placing each Simulink block in series taking into account the corresponding architecture layout. The Simulink blocks diagram of A5 can be found in Figure A.3 of the Appendix A.2. For illustrative purposes, the complete flowchart of architecture 5 is also presented in Figure 3.17. The remainder of the architectures is in Appendix A.4.

3.6 Optimisation model

For engineers, the design process involves a series of iterations. This iterative design approach may be replaced with design optimisation to shorten the design cycle and improve the quality of the final product. Design optimisation involves a formal description of the optimisation method including the design variables to be adjusted, the objective to be reduced, and the constraints to be fulfilled. During the TMS conception, many variable values were estimated. Since some of them have a large impact on the final results and different performance metrics, an optimisation study is carried out in this phase.

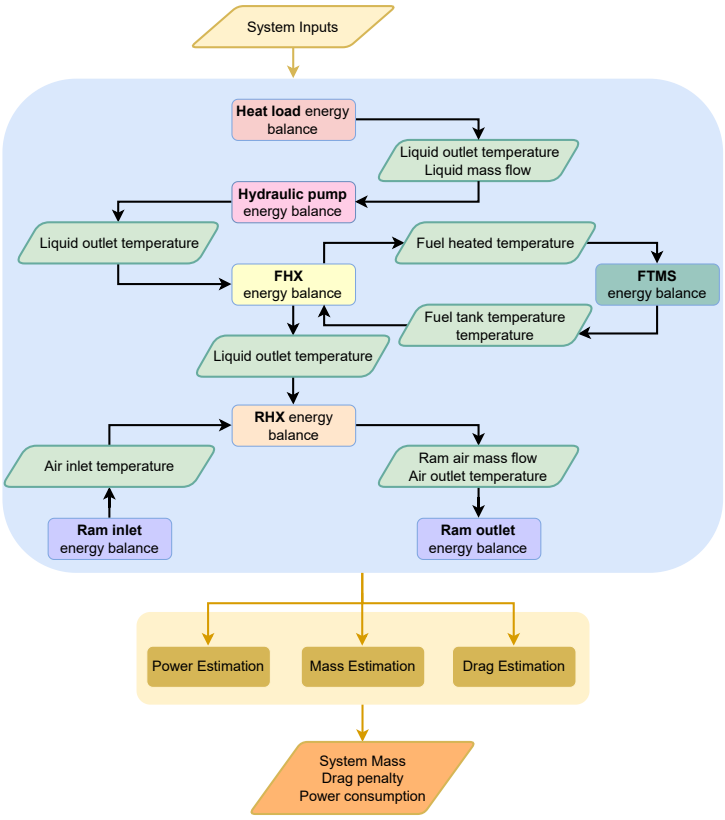

Figure 3.17: Architecture 5 flowchart.

3.6.1 Multi-objective optimisation

The optimisation design first step involves drafting a description of the design challenge, including a system description and a list of all the goals and criteria to be fulfilled. The next step is to choose the variables that characterise the system, i.e. the design variables - x. The dimension of the optimisation problem is determined by the number of design variables and the challenge is to set their lower and upper limits. A summary of all the design variables considered for each architecture and their corresponding limits are presented in Table A.1 in Appendix A.5.

Then, the objective function - $g(x)$, which is a metric that decides if one design is superior to another, must be established. This function must be a computable scalar for the specified vector of design variables. The goal function may be minimised or maximised within the set of prescribed constraints, depending on the task. In the great majority of real design optimisation problems, there are function constraints. However, because the purpose of this research is to determine the actual effect of HEP and TMS on a future aircraft, no constraints are imposed. With this in mind, the optimisation problem statement can be defined as: minimise/maximise the objective function by varying the design variables within their bounds [130].

There is no universally efficient optimisation strategy for solving all sorts of problems. Thus, it is essential to identify the optimisation challenge and comprehend the properties of optimisation algorithms in order to pick the optimal method for solving the problem at hand. The main optimisation methods may be categorised in [130]:

- Gradient-free algorithms, where the user only needs to supply the models that calculate the objective and constraint values for every given set of permitted design variables.
- Gradient-based algorithms, which use gradients of both the objective and constraint functions with respect to the design variables.

When gradients are unavailable, such as in the case of "black-box functions" or, in this case, Simulink models, gradient-free methods may be advantageous. Additionally, unconstrained problems, can also be treated by using gradient-free algorithms. One key benefit of a gradient-free algorithm is that it does not presume function continuity. Having to balance a number of different goals at once is another common justification for switching to an approach that does not rely on gradients since it allows a better exploration of the design space [130]. In this work, a gradient-free multi-objective function is used. Firstly, it is difficult to guarantee that the Simulink models behave as continuous functions. Secondly, there are various contradicting targets that cannot be simply incorporated into a single purpose, namely, drag penalty, total mass and energy consumption. These three parameters are the ones set as the objective functions to be minimised in the TMS optimisation problem, which can be mathematically stated as follows:

$$\begin{aligned} &\text{minimise} && g(x) = [\text{Energy Consumption}\,(x)\,,\ \text{Mass}\,(x)\,,\ \text{Drag}\,(x)] \\ &\text{with respect to} && x \end{aligned} \quad . \tag{3.52}$$

With multiple objectives, we have to reconsider what it means for a point to be optimal. In a multidisciplinary design optimisation, we use the concept of Pareto optimality [130]. If one design is better than another in every metric, we say that design dominates. If no other assessed points have dominance over it, then that point is said to be non-dominated. Pareto optimal refers to the optimal point that is non-dominated by any other point in the entire domain. It only indicates that no other point is dominant over it; however, it does not imply that this point is the most dominant of all. The Pareto set is the collection of all possible optimum solutions (x^*), while the Pareto front is the set of all possible optimum functions ($g(x^*)$). Pareto front can be optimal or sub-optimal as illustrated in Figure 3.18. Considering the complexity involved and the high-dimensionality of some optimisation issues, a really optimum Pareto Front is often not attained.

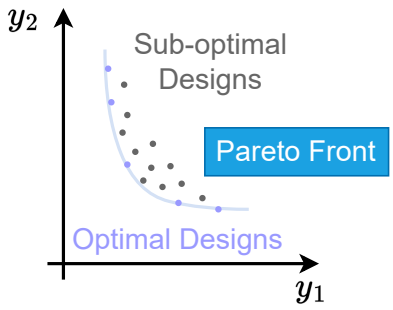

Figure 3.18: Example of optimal and sub-optimal Pareto fronts.

Multi-objective design problems may be solved using weighted-sum, epsilon-constraint, normal boundary intersection, and evolutionary algorithms [130]. Genetic algorithms (GAs) are the most popular

and well-known sort of evolutionary algorithms, and the solution chosen for this problem since it has a low computational cost and it is adequate for covering the entire design space.

GAs are population-based, being characterised by a global search [131]. Rather than a single beginning point, the optimisation begins with a group of design points (population), and each optimisation iteration (generation) modifies this set. Each point is represented by a chromosome with the values for every design variable. Each variable in the design is represented by a gene. Using an algorithm inspired by biological reproduction and evolution, GAs develop the population via three primary steps: (1) selection, (2) crossover, and (3) mutation. Reproduction and mutation stages remain the same in the multi-objective form of the GA compared to the single-objective variant. The fundamental distinction is in the fitness evaluation and selection method. In this work, the elitist Non-dominated Sorting Genetic Algorithm (NSGA-II) introduced in 2002 by Deb et al. [132], as provided in [133], is used.

An algorithmic step of NSGA-II involves locating a non-dominated set (i.e., the current approximation of the Pareto set). In addition to defining the non-dominated set using NSGA-II, the goal also passes through sorting all members of the population by their dominance depth, also known as non-dominated sorting. All non-dominated points in the population (i.e., the current approximation of the Pareto set) are ranked 1 according to this method. The next group of non-dominated points is assigned a rank of 2, and so on, as presented in Figure 3.19. Using the provided NSGA-II algorithm and after setting up the optimisation design variables and objective functions, the Pareto Front for the TMS architectures can be obtained.

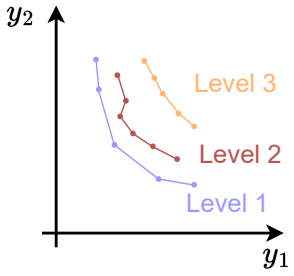

Figure 3.19: An illustrative example of Rank 1, 2 and 3 of NSGA-II.

3.6.2 Optimisation under uncertainty

Uncertainty is a part of every practical engineering challenge. It can come from a variety of sources and it is always present throughout the engineering process. In the aeronautical sector, aerodynamic loads, flying speed, angle of attack and tolerances on dimensions and shapes are some examples of these uncertainties [134]. Uncertainties in design variables and simulation models are ignored by a deterministic optimisation approach. When x is labelled as "uncertain," it is no longer a deterministic input. Instead, it is a probability-distributed random variable [130].

Changing the typical deterministic problem is necessary to incorporate uncertainties into the design optimisation process. Robust Design Optimisation (RDO) and Reliability Based Design Optimisation (RBDO) are two of the most popular approaches that account for uncertainty [135]. A design is considered robust if its performance is less susceptible to inherent variation. "Performance" in this context is directly

associated with the objective function in optimisation. Consequently, the objective function of a robust design is less sensitive to variations in the random design variables and parameters. This can be accomplished by formulating an objective function that takes these variations into account and reflects uncertainty. There are numerous formulation options for robust design optimisation problems. The most typical objective is to minimise the expected value of the objective function. Variance, or standard deviation, is an additional frequently used metric. These two measurements represent a compromise between risk (variance) and return (mean) [130]. Thus, a RDO problem can be formulated by:

$$\begin{aligned} &\text{minimise} && G\left(\mu_g(x), \sigma_g(x)\right) \\ &\text{subjected to} && P\left(x_k^{LB} \leq x_k \leq x_k^{UB}\right) \geq P_{\text{bounds}} \quad k = 1, ..., n_{DV}, \end{aligned} \tag{3.53}$$

where μ_g is the mean value, σ_g the standard deviation, x the deterministic design variable, n_{DV} the number of design variables, and P the probability. Now, the robust objective (G) is a function of the mean and standard deviation of the objective (g), which in turn depends on the probabilistic distribution of the variables.

Several methods are available for computing the mean and standard deviation analytic integration. Among these is the Sigma Point (SP) method. SP is based on the principle that it is simpler to match an input distribution (typically a normal distribution) than to linearise (or approximate) a non-linear mapping. To compute integrals in SP, a process similar to Gaussian integration is used, but the sample locations and weights are optimised to match the first moments of the input probability distribution [136].

In this work, an in-house RDO code with the SP method was adapted for solving the optimisation problems under uncertainty. The variables carrying uncertainty are the ambient temperature at sea level and the external flow boundary layer thickness. Therefore, the performance of the different architectures will be less sensitive to inherent variability in the external temperature (counting for hotter and cooler days) and in the external boundary layer and its chaotic behaviour.

3.6.3 Coupled TMS and HEP optimisation

In order to simulate the thermal management system with different propulsive architectures, different energy sources and with a more realistic heat load value instead of a 100 kW generic one, in a further study, the TMS A5 was coupled with a series, parallel and turboelectric propulsion computational models developed by Iara [18]. A multi-objective optimisation using the same NSGA-II algorithm is conducted in this phase with the goal of minimising the total system mass (TMS and HEP) and CO_2 emissions. The design variable is the hybridisation factor, which expresses the percentage (from 0 to 1) of total power that comes from the electric system (battery). The emissions are evaluated using Equation 3.54.

$$m_{CO_2} = \left(\frac{e_{\text{bat},p}}{2000} + e_{\text{bat},re}\right) E_{\text{bat}} + e_{f,p} \times m_{T0} \times e_f^* + ef_{f,cs} \times m_{T0} \; + \frac{e_{\text{liquid},p}}{2000} \times m_{\text{liquid}}, \tag{3.54}$$

where e stands for emission factor, bat for battery, f for fuel, p for production, re for recharge, cs for

consumption, E for energy, m for mass, and e^* for energy density. The constant 2000 represents the number of cycles between battery replacements. The emission factors considered are detailed in Table A.2 for an optimistic and pessimistic environmental scenario.

Increasing the hybridisation factor will increase the battery load and mass and decrease the CO_2 emissions. The power dissipated by each architecture component will be different for each hybridisation factor, as well as the fuel mass flow required by the internal combustion engine. These parameters will influence the behaviour of the thermal management system. The results are discussed in the next chapter. It is worth mentioning that no feasibility limitation to the mass of the entire system is posed, thus care should be taken when analysing the results since the same aerodynamic characteristics are being considered.

Chapter 4

Results

With the implementation of the different thermal management system architectures completed, in this chapter, the results of each architecture are presented, compared and discussed. After presenting the baseline scenario used to simulate the different TMS in Section 4.1, the baseline results are shown in Section 4.2. A physical interpretation of these is carried out, as well as a critical discussion and comparison between the different architectures analysed. The impact of the TMS baseline solutions on mass, drag and energy consumption is also a subject of evaluation. In Section 4.3, a parametric study is conducted to investigate how a selection of different operating conditions and parameters impacts the performance of the baseline thermal management systems. The overall influence and impact of these variables are assessed both quantitatively and qualitatively. Lastly, in Section 4.4, the multi-objective optimisation Pareto fronts with and without uncertainty variables are shown.

4.1 Problem baseline scenario

The baseline simulation scenario for all the thermal management architectures is defined in Table 4.1.

For the baseline results, some geometric parameters of the ducts are also considered and described in Table 4.2. The reference values for the fuel tank wetted areas were presented in Equation 3.50. The parameters used in the heat exchangers sizing were also already introduced in Tables 3.5 and 3.6.

4.2 Baseline results

The results displayed in this section represent the baseline scenario for each architecture using the baseline references described above. Different flight phases are considered in the discussion, including Take-Off (TO), Cruise (CR) and Landing (L). In Section 4.2.1, the results will be split, presented and discussed into three different families based on the heat transfer technologies employed: (1) liquid cooling, RA and VCS (A1 and A2); (2) liquid cooling and RA (A3 and A4); (3) liquid cooling, RA and FTMS (A5). Then, a comparison supported by a critical discussion of those families is carried out in Section 4.2.2. Section 4.2.3 studies the overall impact of each architecture on mass, drag and power consumption.

Table 4.1: Conditions for the baseline scenario of all TMS architectures.

Parameter	Value/Range	TMS architecture
Flight altitude profile	Figure 3.2(a)	All
Mach number profile	Figure 3.2(b)	All
Duration of flight	3600 s	All
Equipment heat load $\dot{Q}_{\text{equip}}$	100 kW	All
Mass flow rate of liquid per kW O_{liquid}	0.045 kg/skW	All
EGW velocity in the ducts	2.5 m/s	All
Equipment maximum allowable temperature T_{control}	305 K	All
Pump efficiency η_{pump}	0.5	All
Fan efficiency η_{fan}	0.4	All
Temperature difference HEX ΔT_1	10 K	All
Condensation Temperature T_{cond}	325.3 K	A1, A2
Evaporation Temperature T_{evap}	278 K	A1, A2
Compressor efficiency $\eta_{\text{comp}}/\eta_{\text{isen}}$	0.8/0.8	A1, A2
SHX Area A_{SHX}	5 m^2	A2, A4, A5
Thermal boundary layer thickness t_{bd}	0.01 m	A2, A4, A5
Distance along the fuselage/wing to SHX X	18 m/0.5750 m	A2, A4/A5
Initial tank fuel temperature T_{T0}	288 K	A5
Initial tank fuel mass m_{T0}	721 kg	A5
Mass flow rate of fuel to the engine $\dot{m}_e$	Table 3.4	A5
Mass flow rate of recirculation fuel $\dot{m}_r$	0.15 kg/s	A5

Table 4.2: Ducts geometrical parameters.

	Duct length - L [m]	Duct Thickness - t [m]	Duct diameter - D_h [m]
EGW flow	20	0.0025	-
R314 flow	10	0.00117	0.0254
Fuel flow	5	0.0025	-

4.2.1 Family architecture baseline results

Architectures 1 and 2 Architectures 1 and 2 are presented in Figures 3.3(a) and 3.3(b), respectively. Both use a liquid cooling loop, a vapour compression system and a ram air inlet to cool the equipment. The difference between the two is that, in architecture 1, the heat is only removed via the evaporator to the vapour cycle, while, in architecture 2, before transferring heat to the VCS, the liquid rejects heat to the ambient air through a skin heat exchanger.

The results of the variation of the EGW temperature at different points of the liquid cooling loop are presented in Figure 4.1(a). In both cases, the equipment heat waste (100 kW) warms the EGW mixture approximately in 7 K: from 305 K (that is considered the control temperature) to approximately 312 K. In architecture 1, the evaporator will be responsible for rejecting all the heat load and cooling down the liquid again from 312 K until 305 K. In architecture 2, the liquid is cooled in two sections. The yellow line in Figure 4.1(a) represents the outlet EGW mixture temperature after passing through the SHX. The SHX cooling capacity is expected to be higher at cruise altitude, according to [71] and confirmed in

Figure 4.2(a), due to the lower ambient air temperature. According to the ISA model, the atmospheric air temperature for the mission profile is presented in Figure 4.1(b).The small peaks in the temperature profile are related to changing Mach at a constant altitude or changing altitude at a constant Mach. The fluid outlet temperature is also lower in CR. During take-off and landing, since the atmospheric temperature is unfavourable, the liquid exits the SHX at a higher temperature.

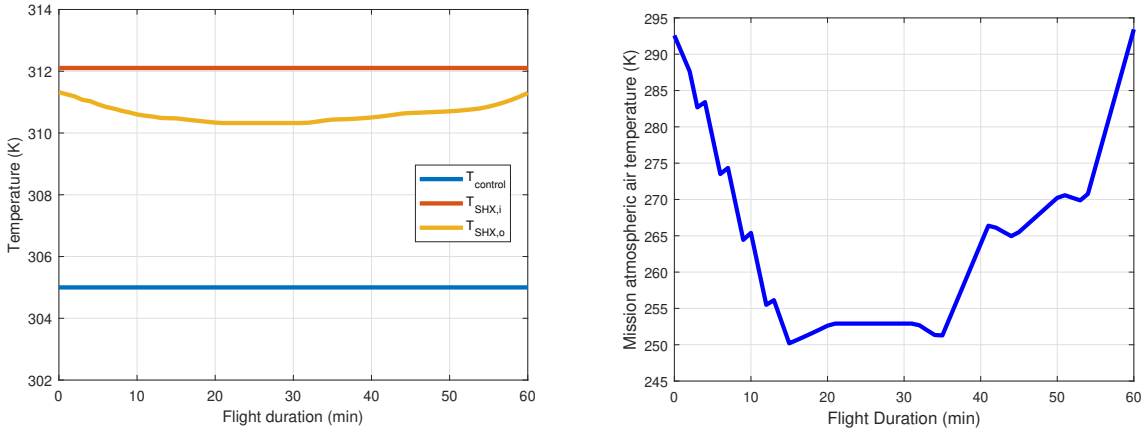

(a) EGW temperature (Architecture 2).

(b) Mission atmospheric temperature profile.

Figure 4.1: EGW temperature at different liquid cooling circuit points (A1 and A2) and atmospheric air temperature profile.

The heat transfer rates for A1 and A2 in the different stations can be seen in Figure 4.2.

For A1, the heat that needs to be rejected by the evaporator (green line in Figure 4.2(b)) is the total equipment waste and the additional heat introduced by the hydraulic pump (almost negligible). To guarantee the VCS energy equilibrium, the heat load exchanged in the condenser is the sum of the evaporator heat transfer rate with the compressor work. This way, the condenser of the vapour cycle will reject approximately 128 kW to the ram air. The heat transfer rate exchange in the condenser and the VCS compressor work are highlighted by the green line, respectively, in Figures 4.2(c) and 4.3(b). It is interesting to note that, unlike A2, the heat transfer rate exchanged by all the components in A1 is constant since it only depends on the heat load, control temperature and evaporation and condensation temperatures that are considered constant throughout all the mission.

In A2, the heat transfer rates in the different stations will vary since the system behaviour depends on the ambient temperature used to cool the liquid in SHX. As previously mentioned, SHX cooling capacity is higher during cruise, with 25% of the heat being rejected through it in this phase (approximately 25 kW), as highlighted in Figure 4.2(a). During take-off, SHX is only capable of rejecting approximately 11kW due to the higher ambient temperature. An important note taken from this is that, although SHX seems a feasible and interesting solution in this context, medium to long-haul flights with a longer cruise phase may be more appropriate.

The variation of the heat transferred to the VCS through the evaporator is the opposite of the variation of the heat transfer rate across SHX since the sum of both results in the total heat load that enters the system (ensuring the system energy equilibrium). Since the heat rejected to VCS is at its minimum during cruise (red line in Figure 4.2(b)), the required compressor work (red line in Figure 4.3(b)) and the heat

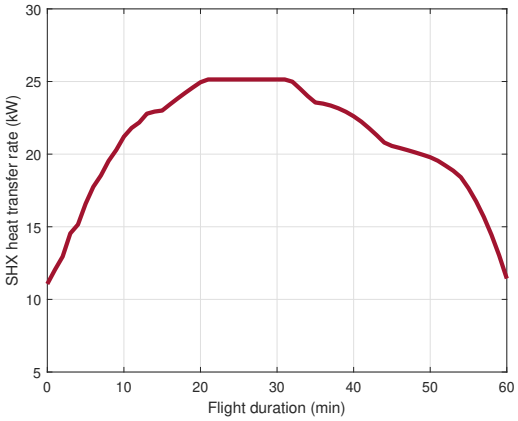

(a) SHX heat transfer rate.

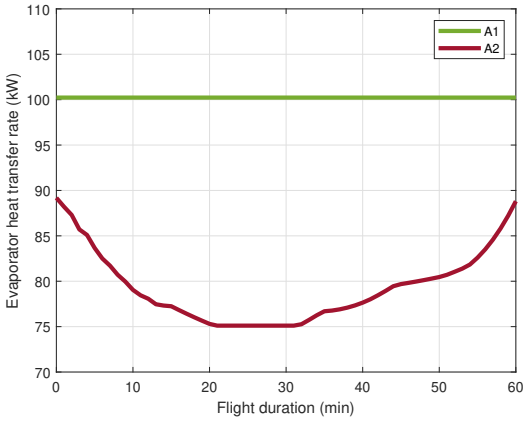

(b) Evaporator heat transfer rate.

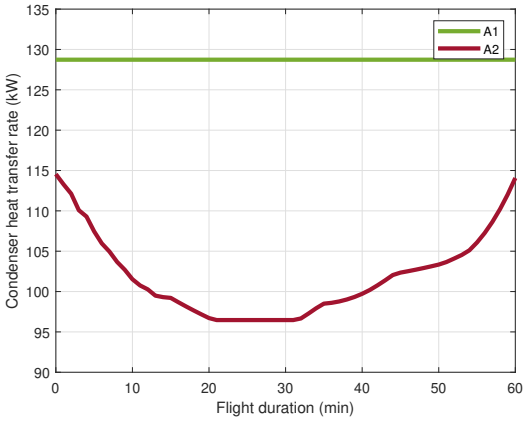

(c) Condenser heat transfer rate.

Figure 4.2: Heat transfer rate results (A1 and A2).

rejected at the condenser (red line in Figure 4.2(c)) are also lower during CR.

Due to the favourable cooling properties of ram air during cruise, less mass flow is required in CR, setting TO and L as the critical points in terms of ram inlet flow in both cases (Figure 4.3(d)). The ram air mass flow required is higher in case 1 (green line) since more heat is transferred at the condenser level. The difference in RA required between both architectures is more visible during CR because, as previously mentioned and shown in Figure 4.2(c), for architecture 2, the heat transferred to the ram air is even lower in this phase. Regarding the fan, this device is only used during take-off and landing to ensure that the required mass flow of RA enters the aircraft. The fan work is 2 kW higher in case 1 (15 kW represented by the green line in Figure 4.3(c)) when compared to case 2 (13 kW represented by the red line) since more RA mass flow needs to be pulled. About the electric consumption of the hydraulic pump represented in Figure 4.3(a), since the pressure drop through the liquid cooling loop is roughly estimated, the value is only indicative and used to compare the different architectures. In this case, the pump work required is higher in case 2 (approximately 0.5 kW) since more heat transfer stations are considered, namely, the SHX, resulting in a greater pressure drop.

The R314 temperature and entropy in the different VCS loop points were already presented in Figure **??**. It is worth to mention that the vapour compression system COP is around 2.8 for the operating

conditions. This value is in the range of refrigerators typical experimental performance [137].

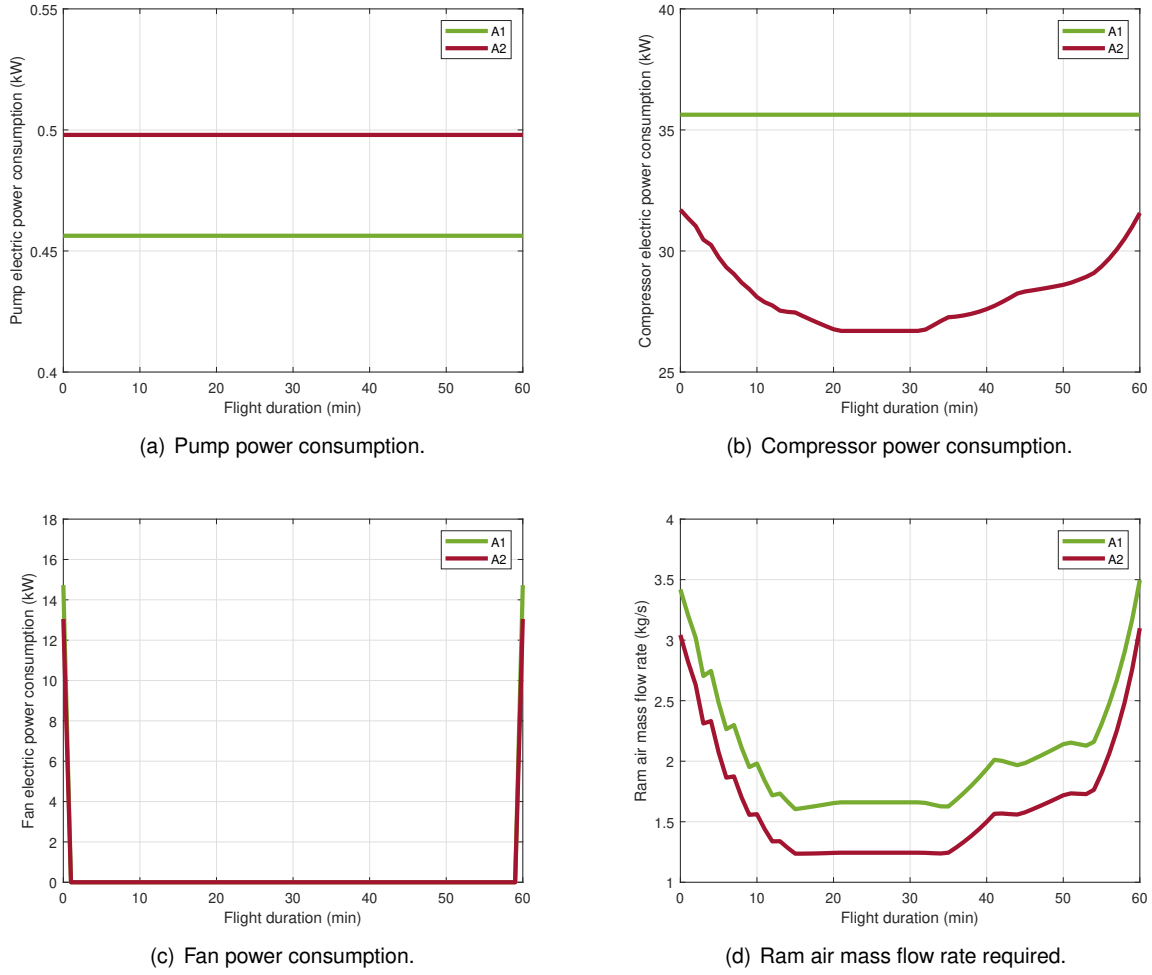

(a) Pump power consumption.

(b) Compressor power consumption.

(c) Fan power consumption.

(d) Ram air mass flow rate required.

Figure 4.3: Power electric consumption and ram air mass flow rate results (A1 and A2).

Architectures 3 and 4 Architectures 3 and 4 are presented in Figures 3.4(a) and 3.4(b), respectively. Both use a liquid cooling loop and ram air inlet to cool the equipment. The difference between the two is that, in architecture 3, the heat is only removed via a RHX, while in architecture 4, before rejecting heat to a ram air mass flow, the liquid transfers heat to the ambient air through a skin heat exchanger. It is possible to note that case A3 basically corresponds to A1 but replaces the VCS with a RHX, while A4 matches A2 but again replacing VCS with a RHX.

Using the same operating conditions, the SHX in A4 will have the same behaviour and effect in the system as in A2, as it is possible to prove by comparing Figure 4.2(a) to Figure 4.4(a). This can be explained by the fact that the air outside temperature is the same, the inlet EGW temperature is the same and the reference area used to cooled (A_{SHX}) is equal in both cases. This way, the evolution of EGW temperature in the circuit is the same as described in Figure 4.1(a).

Moreover, it is important to look at the RHX heat transfer rate in Figure 4.4(b). Again, the variation in both A3 and A4 is the same variation described at the evaporator level for A1 and A2. The difference is that instead of having an evaporator rejecting heat to a refrigerant and, only then, a condenser rejecting

heat to a ram air flow, in cases 3 and 4, the heat is rejected directly to the RA. However, the heat transfer rates of RHX and evaporator at stake are the same when comparing the A1 to A3 and A2 to A4.

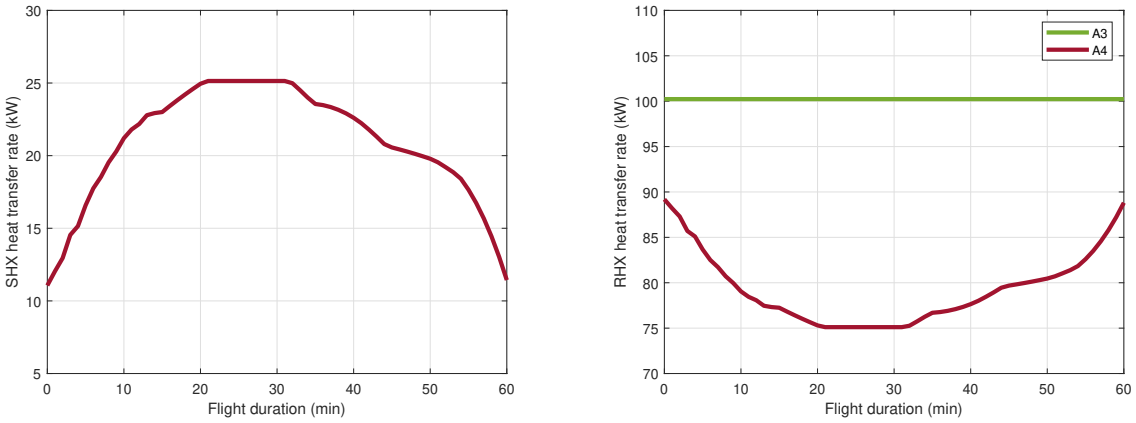

(a) SHX heat transfer rate.

(b) RHX heat transfer rate.

Figure 4.4: Heat transfer rate results (A3 and A4).

The graph presented in Figure 4.5(b) that describes the ram air mass flow variation throughout the flight has the same behaviour as previously described. The lower ambient temperature (in both cases) and the lower heat transfer rate required in CR (in A4) result in less mass flow needed for that phase. Although the ambient conditions are considered the same, more heat is expected to be rejected via the RHX in A3. This way, the mass flow is slightly higher in A3 with 2.025 kg/s of RA required (green line) during CR, when compared to 1.575 kg/s of RA for A4 (red line). The fan work presented in Figure 4.5(a) also has the same response as described for A1 and A2 (Figure 4.3(c)). Again, the necessary fan work is higher for A3 than A4 since more air flow needs to be pulled inside the aircraft.

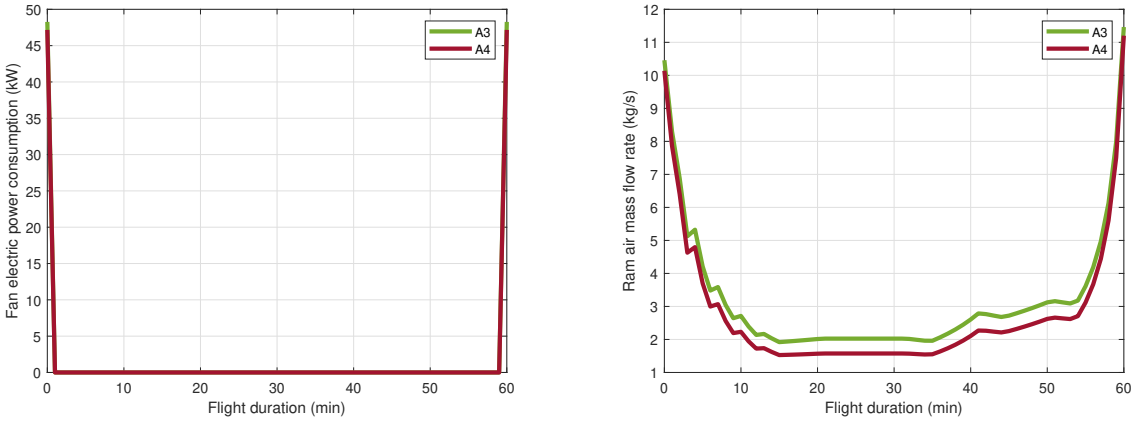

(a) Fan power consumption.

(b) Ram air mass flow rate required.

Figure 4.5: Power electric consumption and ram air mass flow rate results (A3 and A4).

Architecture 5 Architecture 5, presented in Figure 3.5, differs from the other schemes since it also uses fuel as a heat sink. To use fuel as a heat sink, a fuel thermal management system is developed and the fuel is heated via a fuel heat exchanger and cooled using the skin heat exchanger concept.

As the other counter-flow heat exchangers, the FHX is designed to guarantee a temperature difference (Δ_T) between the EGW mixture inlet and the fuel outlet of 10 K. This way, since the equipment heats the EGW mixture from 305K (blue line in Figure 4.6(a)) until 312K (orange line in Figure 4.6(a)), the liquid inlet temperature is going to be constant, as well as the heated fuel temperature with a reference value of approximately 302K (orange line in Figure 4.6(b)). This value is far from the maximum fuel temperature allowable for GEVO-JP-8, which is considered to be between 318.150 K and 323.150 K according to [124]. With that said, the concept of thermal endurance will not be evaluated in this work since the fuel will not be overheated under the effect of heat loads during the flight.

After passing through the fuel heat exchanger, the recirculation fuel is cooled through a skin heat exchanger. Again, as in the previous cases, for a constant inlet temperature, since the outside air temperature is lower at the cruise phase, the skin heat exchanger cooling capacity is at its maximum (Figure 4.7(a)) and the temperature of the cooled fuel will be lower in CR (yellow line in Figure 4.6(b)). Comparing the minimum fuel temperature (263.526 K) to the GEVO-JP8 freezing point (195.150 K [124]), no freezing issues are raised in these operating conditions.

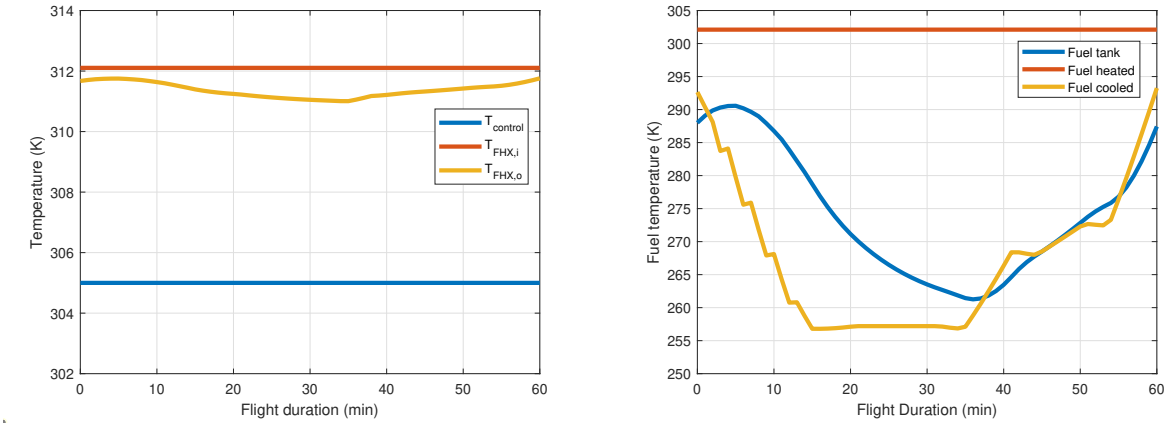

(a) EGW temperature at different liquid cooling circuit points.

(b) Fuel temperature at different FTMS circuit points.

Figure 4.6: EGW temperature at different liquid cooling circuit points and fuel temperature at different FTMS circuit points (A5).

The recirculation fuel temperature will decrease until the cruise phase, so the fuel temperature in the tank (blue line in Figure 4.6(b)) is also expected to decrease. The first initial increase described by the blue line can be explained by two factors. Firstly, in the first flight section, the outside air temperature is higher than the fuel temperature. The tank walls, a usual medium of heat loss from the fuel to the air, favour the exchange from the outside air to the fuel, increasing the temperature inside the tank. Secondly, the temperature of the cooled fuel in the first flight segment is superior to the initial temperature of the fuel in the tank according to the described operating conditions. After that small temperature increase until the end of the cruise segment, the heat loss through the tank walls and the lower cooled fuel temperature (both due to a lower atmospheric temperature) explain the temperature decrease of the fuel in the tank.

After the cruise phase, the outside air temperature increases. Again, this has two main effects on the FTMS: (1) a decrease in the skin heat exchanger cooling efficiency; (2) a decrease in the heat losses through the tank walls. Having a higher recirculation fuel temperature from the SHX (higher than the

actual fuel temperature in the tank) and less heat being transferred to the surroundings of the tank, an increase in the fuel tank temperature is registered until the end of the flight.

The $\dot{Q}_{\text{loss}}$ evolution depends on the temperature of the fuel in the tank and at the same time has an influence on it. In the first segment of the flight, the negative values of $\dot{Q}_{\text{loss}}$ reveal that the outside air temperature is higher than the fuel temperature, i.e., heat is being transferred from the outside air to the fuel. After, the temperature of the atmospheric air starts decreasing as well as the fuel temperature. However, the outside temperature decreases at a higher rate so the difference between the two increases, leading to more heat being rejected through the tank walls. During the cruise phase, since the aeroplane is flying at the same altitude and at the same velocity, the outside temperature remains constant, as shown in Figure 4.1(b). The system determines that the fuel temperature decreases until the end of cruise, which causes the temperature difference between the outside air and the fuel to decrease and less heat to be rejected in the tank section in this phase. After the cruise, the outside temperature begins to rise as well as the fuel temperature. The difference between the two varies, leading to the less clear variation shown in the last section of the flight (from 35 minutes onwards).

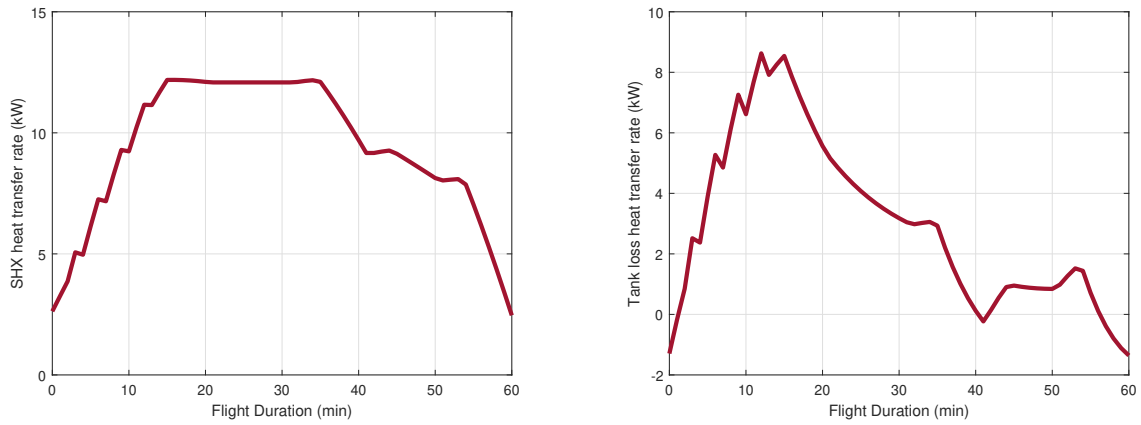

(a) SHX heat transfer rate.

(b) Tank loss heat transfer rate.

Figure 4.7: Heat transfer rate results(A5).

Since the inlet temperature and the mass flow rate of the EGW mixture through the FHX is constant, the heat transferred in this section only depends on the fuel temperature in the tank and the fuel mass flow. The variation in the temperature of the fuel in the tank was previously described and justified (blue line in Figure 4.6(b)). Regarding the mass flow rate, according to Table 3.4, it is constant through each flight phase (climb, CR and descent), decreasing from segment to segment. A lower fuel tank temperature provides a better fuel heat exchanger performance, and consequently, a lower outlet EGW mixture temperature in this stage. However, the mass fuel flow rate decrease is unfavourable to the heat exchange through the FHX. The increase of the fuel temperature in the tank at the beginning of the flight will lead to a decrease in the heat transfer rate through the FHX in the first flight portion, as described in Figure 4.8(a). After that, the decrease of the fuel temperature in the tank until the end of CR potentiates the heat transfer, and although when passing to CR the mass flow rate of fuel decreases, the heat transfer rate continues to increase. Then the fuel temperature in the tank starts to increase during the descent

phase and there is a massive break in the fuel mass flow going to the engine which causes the FHX heat transfer rate to decrease and a visible peak of the heat transfer rate of approximately 35 minutes after TO.

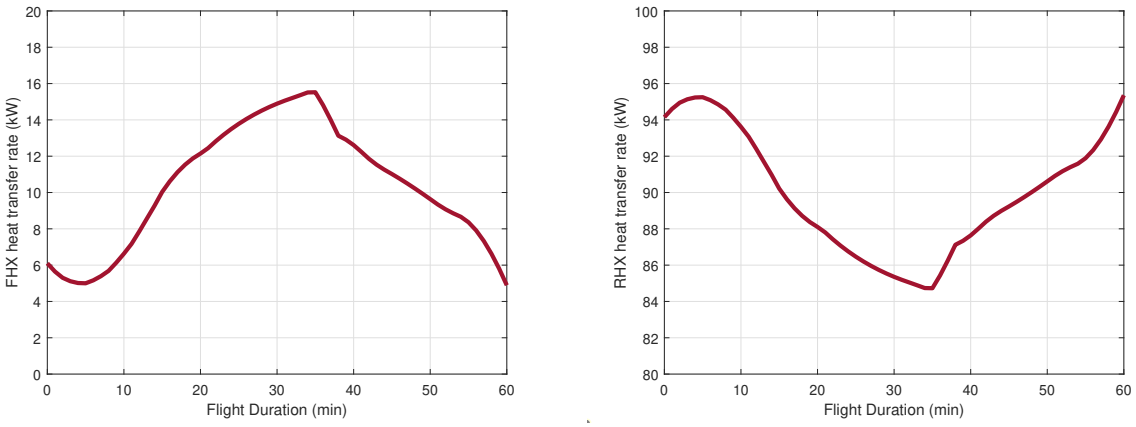

(a) FHX heat transfer rate.

(b) RHX heat transfer rate.

Figure 4.8: Heat transfer rate results (A5).

Looking at the liquid cooling loop, since the heat transfer rate through the FHX has the behaviour described above, in order to dissipate the constant heat load of 100 kW transferred from the equipment and the hydraulic pump load (248 W) to the EGW mixture, the ram air exchanger exhibits the reverse behaviour. In other words, when the heat capacity of the fuel heat exchanger is at its maximum, there is less heat that needs to be removed by the RA. This way, according to Figure 4.8(b), it is possible to see that the variation of the heat transfer rate in the RHX throughout the flight is the opposite of the one described for the FHX, and if we sum both contributions the system dissipates the total load of approximately 100 kW (hydraulic pump load is almost negligible). Regarding the outlet EGW mixture temperature at the fuel heat exchanger shown by the yellow line in Figure 4.6(a), increasing the heat transfer rate through the fuel heat exchanger means that the liquid can be cooled until lower temperatures, so it is possible to identify a minimum after the cruise corresponding to the maximum of the heat transfer rate registered for the FHX too.

It is also worth to note that the heat transfer rate required from the RHX is decreasing at CR, the same phase where the ambient air conditions are favourable to the transfer given the low ambient air temperature. This way, the ram air mass flow required to cool the liquid mixture is lower during CR due to these two contributing factors, as is possible to see in Figure 4.9. The RA required is not constant during cruise (in fact it is slightly decreasing) because the RHX heat transfer rate is not constant in this phase as it was for the previous architectures. Regarding the power consumption, the results for both the hydraulic pump and fan follow the same behaviour described before and for this reason these components results are not presented herein. The hydraulic pump work is constant and equal to 497.941 W. The fan consumes approximately 47.822 kW during take-off and landing phases. The fuel pump power consumption is assumed to be constant and as mentioned in Section 3.3.9, a typical pressure drop passing the fuel lines is assumed according to [138]. The fuel pump power consumption value is 3.220 kW throughout the whole flight since the recirculation mass flow of fuel does not change.

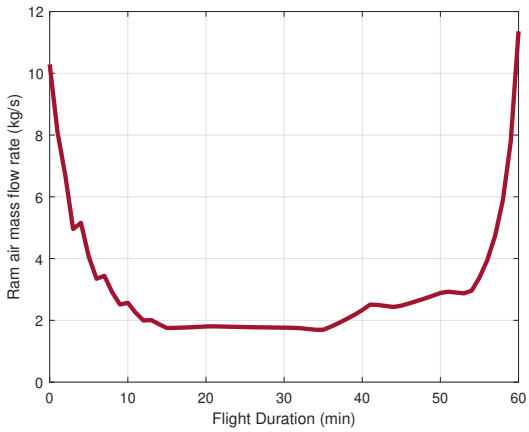

Figure 4.9: Ram air mass flow rate results (A5).

4.2.2 Comparison between different family architecture baseline results

Heat transfer rate results Table 4.3 summarises the most important heat transfer rate results for some important flight stages.

Table 4.3: Comparison between heat transfer rate results.

Results	A1	A2	A3	A4	A5
CR SHX heat transfer rate (kW)	-	25.140	-	25.140	12.083
TO SHX heat transfer rate (kW)	-	11.061	-	11.061	2.627
CR Evaporator heat transfer rate (kW)	100.228	75.108	-	-	-
TO Evaporator heat transfer rate (kW)	100.228	89.187	-	-	-
CR Condenser heat transfer rate (kW)	128.731	96.467	-	-	-
TO Condenser heat transfer rate (kW)	128.731	114.550	-	-	-
CR RHX heat transfer rate (kW)	-	-	100.228	75.108	84.731 (min)
TO RHX heat transfer rate (kW)	-	-	100.228	89.187	94.147
CR FHX heat transfer rate (kW)	-	-	-	-	15.518 (max)
TO FHX heat transfer rate (kW)	-	-	-	-	6.102
CR Tank heat loss (kW)	-	-	-	-	8.653 (max)
TO Tank heat loss (kW)	-	-	-	-	-1.294

As mentioned before, $\dot{Q}_{\text{SHX}}$ is equal in architectures A2 and A4 due to the similar operating conditions. $\dot{Q}_{\text{SHX}}$ is lower in architecture 5 because, first, the SHX fuel inlet temperature is lower compared to SHX EGW inlet temperature in A2 and A4. Second, the fuel specific heat at constant pressure is inferior to the c_p value of the EGW in the same range of temperatures. According to the first law of thermodynamics in these operating conditions, a higher specific heat is associated with a higher heat transfer rate. Also, the mass flow rate of the fuel is one order of magnitude lower than the EGW mass circulating in the liquid loop, which will also affect the cooling capacity of the SHX. Besides, the number of Reynolds of the external flow is inferior to the other cases since the reference length considered in the wing is smaller. This will lead to an increase in the overall heat transfer coefficient (U) according to Equation 3.37, however, it does not recompense the heat transfer rate penalty induced by the factors described.

Moreover, according to Table 4.3, it is worth to confirm the comparison done previously: there is a similarity between the evaporator in A1 with the ram air heat exchanger in A3, and between the evaporator in A2 and RHX in A4. Regarding the RHX heat transfer rate, its value is, as expected, higher in A3 since in this architecture only the ram air heat exchanger is used to cool the equipment waste heat load. Comparing the A4 to the A5, the first heat dissipation station in A4 (SHX) has a superior cooling potential than the first heat dissipation station in A5 (FHX). Therefore, in architecture 5, more heat needs to be removed by the second heat dissipation station (RHX).

Power consumption and ram air mass flow rate results Table 4.4 summarises the most important power consumption and ram air flow results in some important flight stages.

Table 4.4: Comparison between power consumption and ram air flow results.

Results	A1	A2	A3	A4	A5
Hydraulic pump electric consumption (W)	456.286	497.941	456.286	497.941	497.941
TO Fan electric consumption (kW)	14.726	13.049	48.267	47.164	47.822
CR Compressor electric consumption (kW)	35.628	26.699	-	-	-
TO Compressor electric consumption (kW)	35.628	31.703	-	-	-
Fuel pump electric consumption (kW)	-	-	-	-	3.220
CR ram air mass flow rate (kg/s)	1.660	1.244	2.025	1.575	1.766
TO ram air mass flow rate (kg/s)	3.419	3.043	10.457	10.139	10.289

Since the pressure drop is simply assumed, the hydraulic pump electric consumption only depends on the number of heat sink/source stations. Thus, on the liquid cooling side, cases 1 and 3 only integrate a heat source and a heat dissipation station, resulting in lower liquid pressure drop across the loop and consequently less pumping work required. Architectures 2, 4 and 5 have one heat source and two heat dissipation stations resulting in a superior hydraulic pump work as presented in Table 4.4.

The fan electric consumption is related to the RA mass flow required in both TO and L phases. The major difference is due to the outlet ram air temperature. Since the heat exchangers were designed to guarantee a 10 K difference between the outlet air temperature and the inlet fluid temperature, the hotter the inlet fluid is, the hotter the ram air can exit the RHX. The refrigerant R314a in the VCS from A1/A2 reaches higher temperatures (condensation temperature is 325.3 K) than the EGW in the liquid cooling loop and, accordingly, the ram air will exit the aircraft at higher temperatures for A1 and A2. Besides the larger heat transfer rate transferred to the RA in A1 and A2 (condenser heat transfer rate values in Table 4.3), the higher air outlet temperature leads to a lower mass flow rate required at this level. Therefore, the fan electric consumption in A1 and A2 is inferior when compared to the rest of the architectures.

4.2.3 Impact of the baseline results

Table 4.5 presents the total mass, drag and power consumption impacts of each architecture. The **total mass** of each architecture is estimated by summing each contributing component mass. As mentioned in Section 3.3.4, the mass of the heat exchangers is estimated using formulas for compact heat exchangers

[98], and their values depend on the HEX conductance (UA). In turn, this value depends on the difference in temperature of the working fluids and on the exchanged heat transfer rate (LMTD method). The heat exchangers mass values obtained for the baseline operating conditions range around 5 kg to 20 kg depending on their heat transfer rate and on the type of heat exchanger considered. Regarding the SHX mass, its value is the same for all the architectures and slightly higher than what was expected. The reason behind this result is that the mass calculation is based on experimental construction that implements an aluminium slab with a total area of 5 m^2 with embedded ducts [67]. In a real situation, the slab will not exist, and the structure will be composed of the ducts and the actual aircraft frame (part of the existing structure). The value obtained for SHX mass using the reference area is 80.74 kg and it is only indicative since it is believed to be overestimated. The literature [90] [70] estimations for the SHX mass were about 120 kg but considered a significant larger surface area (all wing or all fuselage). Regarding the electric components, namely the compressor, pump and fan, their mass is estimated using semi-empirical expressions based on data from manufacturers that depend on the power or mass flow being managed. The fan used to pull the ram air has the largest impact (around 90 kg for A3, A4 and A5). The mass of the liquid and the refrigerant circulating is also calculated according to the working mass flow and the ducts size.

From Table 4.5, the final mass values indicate that architecture 5 is the heaviest one (596.208 kg), because, when compared for example with architecture 4, A5 adds the fuel recirculation tubes and the fuel recirculation pump. It also has three heat exchangers (FHX, SHX and RHX) which increase the overall mass. The major difference between architecture 1 and 2 mass is justified by the SHX addition, and the same applies to the difference between architectures 3 and 4. Since the SHX mass is believed to be overestimated, in a real simulation this difference would not be so evident. Based on these initial simulations, A1 is the lightest (388.157 kg) because, first, although it incorporates a VCS cycle, the fan is downsized due to the lower ram air mass flow required during take-off and landing and second, it does not incorporate a SHX. A3 also shows lower mass, but the required mass flow during the considered phases leads to a much heavier fan. It is relevant to note that some structures are not taken into account in the total mass since they are already part of the aircraft (fuel tank, fuel lines, main fuel pump, etc.). The valves and accumulators that may be needed in a real system case are also neglected.

Table 4.5: Total mass, drag and power consumption of each TMS.

Results	A1	A2	A3	A4	A5
Mass (kg)	388.157	536.936	396.797	556.713	596.208
Energy consumption (MJ)	261.575	207.833	9.077	9.245	32.511
CR Drag penalty (N)	255.267	191.291	297.916	230.950	263.448
TO Drag penalty (N)	297.711	264.916	871.209	843.582	856.549

Regarding the **electric energy consumption**, the value is obtained by summing all the electric power consumption contributions and integrating it throughout the whole mission time. A1 and A2 have the biggest energy impact (around 200 MJ) since they have three electric components: the compressor (which has the largest impact as presented in Figure 4.3(b)), the fan and the hydraulic pump. Case 5 also

has a considerable energy consumption (32.511 MJ) due to the fuel recirculation pump which adds an extra power contribution. A3 and A4 are favourable regarding the energy consumption since they only sum the fan and hydraulic pump power inputs.

In this work context, the **drag penalty** is directly related to the ram air required at the RHX level. As during the take-off and landing the mass flow is higher, the expected drag is also superior in TO and L when compared to the cruise phase. The larger drag penalty values are associated with superior RA mass flow projections. The mission drag breakdown design was done in parallel with the mission profile presented in Figures 3.2(a) and 3.2(b). The value of the drag coefficient in take-off, cruise and landing for the FutPrInt50 aircraft and mission are detailed in Table 4.6 [111].

Table 4.6: Design range mission drag breakdown.

Results	TO	CR	L
C_D	0.049072617	0.03243787	0.049742932

Using Equation 3.22, the values obtained for A3, A4 and A5 (the ones which have higher drag impact) are two orders of magnitude lower than the reference C_D mission values. Values around 3×10^{-4} and 2×10^{-4} are the results for TO and CR, respectively. Although the estimation of the drag is done using a low-fidelity model, from these non-precise C_D results, it is possible to conclude that the impact of the ram air inlet on drag is not high considering the aircraft level. An important aspect of this RA design phase is that, although the mass of the RHX was calculated in a first approach considering a large compact heat exchanger, in a real situation, the RA required for take-off and landing cannot be handled with only one conventional heat exchanger. A rearrangement of tiny RHXs could be a possible solution.

4.3 Parametric study

A parametric study has been conducted to investigate the sensitivity of TMS architectures with a selection of different operating conditions including the liquid mass flow rate (Figures 4.10 and 4.11), the skin heat exchanger area (Figure 4.12), the SHX position (Figure 4.13), the designed temperature difference for HEX (Figures 4.14 and 4.15), the recirculation mass flow rate of fuel (Figure 4.16) and the tank parameters (Figure 4.17).

EGW mass flow rate

In section 3.3.1, a norm to determine the mass flow required was introduced. SAE states that flow rates range from 0.023 kg/s to 0.045 kg/s per kW for coolants such as EGW mixtures [115]. The reference value, as depicted in Table 4.1, is considered to be 4.5 kg/s since the systems deal with a total heat load of 100 kW. Three different values within this range are tested and compared in this phase for the A2 case considering the 100 kW load: $\dot{m}_{\text{liquid}}$=2.3 kg/s, $\dot{m}_{\text{liquid}}$=3 kg/s, and $\dot{m}_{\text{liquid}}$=4.5 kg/s (Reference - R). Given the similar behaviour found for the remainder of the architectures, only the A2 case is shown here as an illustrative example.

Decreasing the mass flow rate will result in a larger outlet temperature of the liquid passing the equipment. This way, the liquid temperature entering the SHX will be higher for the case of $\dot{m}_{\text{liquid}} = 2.3$ kg/s. This can be noticed from Figure 4.10(a) comparing the horizontal green line (related to $\dot{m}_{\text{liquid}} = 2.3$ kg/s) and the horizontal red line (related to $\dot{m}_{\text{liquid}} = 4.5$ kg/s).

Using the log-men temperature difference method, the heat transfer rate through the SHX ends up being superior for the case of higher liquid inlet temperature and a lower circulating mass flow, i.e, for $\dot{m}_{\text{liquid}}$=2.3 kg/s. The simulation registered an increase of SHX cooling capacity of 32% and 10% during take-off and cruise phases, respectively, when comparing the extreme cases of liquid mass flow rate (Figure 4.10(b)). The superior cooling capacity and the lower mass flow rate both contribute to a higher temperature difference between the liquid inlet and outlet in this station. This way, looking at Figure 4.10(a), when comparing the two green lines describing the case of $\dot{m}_{\text{liquid}}$=2.3 kg/s, the difference between the inlet temperature (the horizontal line) and outlet temperature (curved line) is higher than the difference registered between the blue lines ($\dot{m}_{\text{liquid}}$=3 kg/s) and the red lines ($\dot{m}_{\text{liquid}}$=4.5 kg/s). Besides the temperature difference being larger, the outlet temperature is around 5 K higher when comparing $\dot{m}_{\text{liquid}}$=2.3 kg/s with $\dot{m}_{\text{liquid}}$=4.5 kg/s.

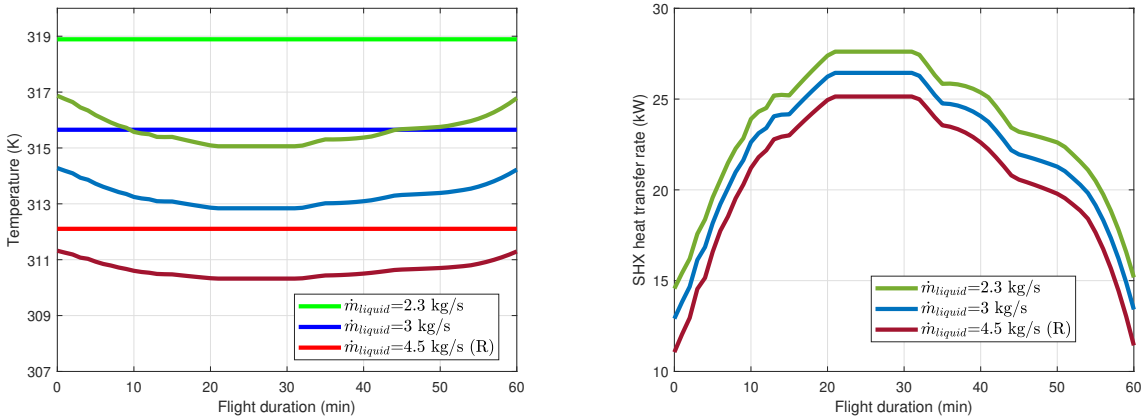

(a) SHX inlet and outlet temperatures.

(b) SHX heat transfer rate.

Figure 4.10: Sensitivity analysis of the EGW mass flow rate for A2.

The heat transfer rate exchanged in the evaporator for the different conditions is presented in Figure 4.11. Even though for a recirculating mass flow rate of $\dot{m}_{\text{liquid}}$=2.3 kg/s, the temperature difference that needs to be managed by the evaporator (to achieve the control temperature) is higher, the lower mass flow rate pays for this advantage and the heat transfer rate exchange at the evaporator level ends up being inferior for this case (green line in Figure 4.11). This can also be seen from a different but equivalent point of view: since more heat is rejected at the SHX level, less heat needs to be dissipated in this phase to guarantee the equilibrium of the system. The evaporator exchanges only 4.0% less heat with $\dot{m}_{\text{liquid}}$=2.3 kg/s comparing to the baseline. This will influence the heat transmitted at the condenser level, the power used by the compressor and the ram air inlet flow required. The differences are insignificant in all parameters. However, it is worth concluding that a lower mass flow has slight advantages over the baseline operating conditions.

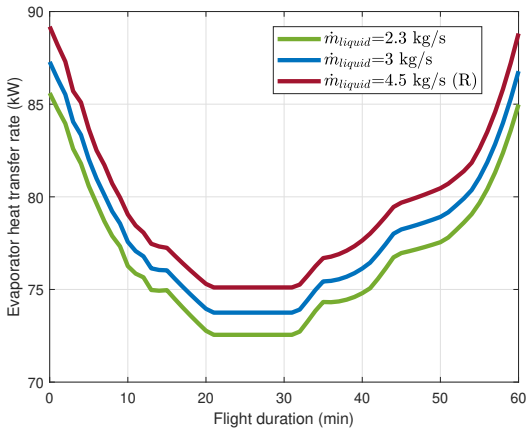

Figure 4.11: Sensitivity analysis of the EGW mass flow rate on evaporator heat transfer rate for A2.

At the same time, having a larger mass flow rate circulating implies more pumping work. Thus, a 34% reduction in the power required by the hydraulic pump is achieved when circulating the lowest flow rate in the range.

The final results on mass, energy consumption and drag comparing the three cases of mass flow rate applied to A2 are presented in Table 4.7. The maximum reduction column percentage refers to the comparison between the best case scenario with the baseline/reference solution.

Table 4.7: Sensitivity analysis of the EGW mass flow rate on mass, drag and energy consumption for A2.

Results	$\dot{m}_{\text{liquid}}$=2.3 kg/s	$\dot{m}_{\text{liquid}}$=3 kg/s	$\dot{m}_{\text{liquid}}$=4.5 kg/s (R)	Max. reduction
Mass (kg)	464.674	489.415	536.936	14%
Energy consumption (MJ)	199.484	203.234	207.833	4%
CR Drag penalty (N)	184.780	187.830	191.291	3%
TO Drag penalty (N)	254.268	259.264	264.916	4%

The maximum reduction in all parameters is registered for $\dot{m}_{\text{liquid}}$=2.3 kg/s . The considerable reduction of the pump, liquid mass and liquid ducts dimension can explain the large difference registered in terms of mass. The reduction of the energy consumption is again justified by the lower pumping power required since the fan and compressor do not show significant changes. The mass flow does not influence considerably the induced drag since the ram air mass flow being pulled inside the aircraft is not significantly changed (maximum difference of 4% during take-off).

SHX Area

As referenced in Chapter 2, according to the study carried out by Kellerman [71] about the potential of using aircraft surfaces for cooling, the SHX heat rejection capacity increases when the surface area increases. Thus, when A_{SHX} is expanded, the heat transfer through the SHX is expected to improve. In order to prove that statement, A4 is used to test the effect of different SHX areas on the system performance. Figure 4.12 shows the results obtained for $A_{\text{SHX}} = 2$ m^2, $A_{\text{SHX}} = 5$ m^2 (R) and $A_{\text{SHX}} = 7$ m^2.

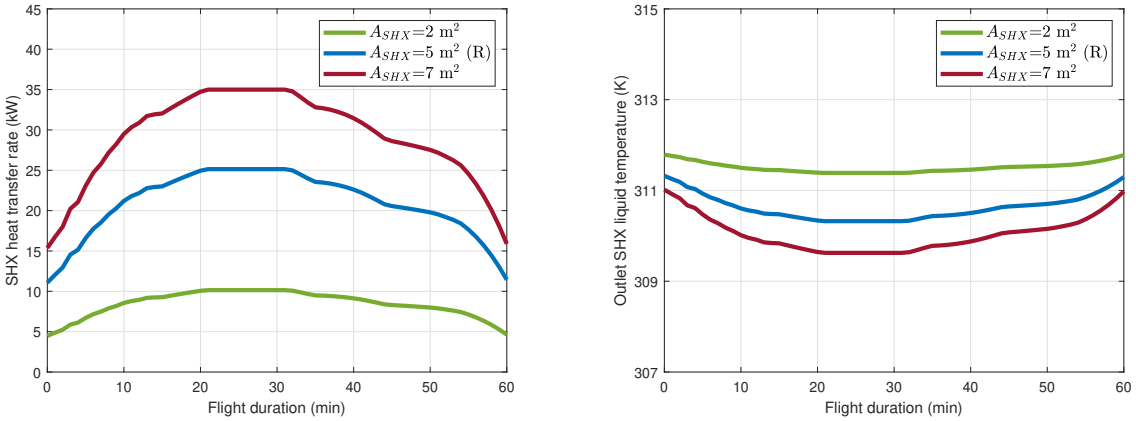

(a) SHX heat transfer rate.

(b) SHX liquid outlet temperature.

Figure 4.12: Sensitivity analysis of the SHX area for A4.

As predicted, the use of a greater heat transfer area results in a higher heat transfer rate represented by the red line in Figure 4.12(a). This will be followed by a decrease in the liquid outlet temperature as represented by the red curved line in Figure 4.12(b). In the overall TMS, this change impacts in the way that less heat needs to be removed by the following stations, namely, the ram air heat exchanger in case 4. The following table summarises some of the most important system results.

Table 4.8: Sensitivity analysis of the SHX area on the mass, drag and energy consumption for A4.

Results	A_{SHX}=2 m^2	A_{SHX}=5 m^2 (R)	A_{SHX}=7 m^2	Max. reduction
Mass (kg)	460.830	556.713	620.523	17%
Energy consumption (MJ)	9.327	9.245	9.186	0.6%
CR Drag penalty (N)	271.468	230.950	203.414	12%
TO Drag penalty (N)	860.596	843.582	831.493	1%

Analysing the results presented in Table 4.8, the increase in skin heat exchanger area will lead to a higher mass and lower energy consumption and drag penalty comparing to the reference case. The decreases in drag penalty and energy consumption can be explained by the fact that less ram air is required in the RHX station, since more heat is rejected in SHX. Besides, a reduction of 17% in mass can be accomplished using 2 m^2 of surface for cooling. As mentioned before, the skin heat exchanger mass is believed to be overestimated, so the difference in mass may in reality be lower. Either way, the increase of the skin heat exchanger area would lead to more ductwork needed to exchange the heat between the liquid and atmospheric air. More ductwork implies more mass and, although the fan will be downsized due to the lower mass flow of ram air being injected into the aircraft, the total system mass ends up being higher for $A_{\text{SHX}} = 7$ m^2.

SHX fuselage/wing position

The position of the skin heat exchanger will have an impact on the Reynolds number of the external flow and consequently on the external heat transfer coefficient. The higher the external heat transfer

coefficient, the higher the global heat transfer coefficient and more heat can be exchanged in this station. The external heat transfer coefficient is related to the Reynolds number using the empirical relation presented in Equation 3.37. Thus, increasing the Reynolds results in a decrease in the external heat transfer coefficient. It is also known that the Reynolds number is directly related to the characteristic length of the flow. For the same ambient conditions, if the skin heat exchanger is positioned nearby the aircraft nose (in case of a fuselage SHX) or the leading edge of the wing (in case of wing SHX), the Reynolds number is low. As a consequence, the heat transfer coefficient increases and the overall heat transfer rate is also expected to increase. For A4 different positions of the SHX (different distance from the nose - X) are analysed and the most important results are presented in Figure 4.13.

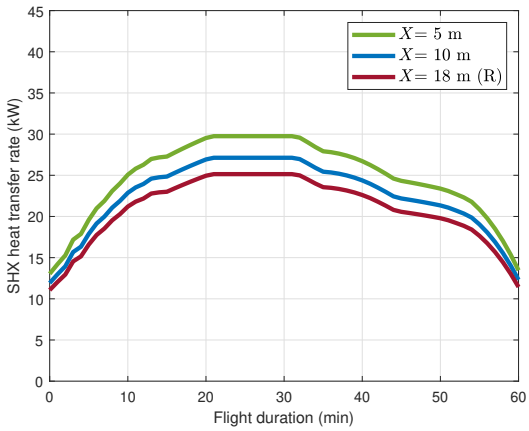

Figure 4.13: Sensitivity analysis of the SHX position for A4.

Although no significant differences are found, the change in position results in the described trend: the further away from the aircraft nose, the lower the skin heat exchanger cooling capacity as presented by the red line in Figure 4.13. The placement will not influence the total mass, drag end energy in a considerable way. There are only marginal reductions in the energy consumption of the fan and in the mass of the ram air heat exchanger (less than 1%) since the ram air required is inferior for $X = 5$ m^2. Thereby, the position of the skin heat exchanger has a small influence on the overall TMS system but a lower value of X results in slightly better results.

HEX temperature difference

The ram air heat exchanger and the fuel heat exchanger are designed using a fixed temperature difference (10 K) for ΔT_1 according to the nomenclature introduced in Equation 3.12. In order to quantify the effect of this variable on the overall system behaviour, analysis using 6 K and 12 K differences are conducted in this phase. With this in mind, important system results of A5, namely SHX and FHX heat transfer rates, are presented in Figure 4.14.

In the FHX, the decrease in the design temperature difference will lead to a higher heated fuel temperature, since the EGW inlet temperature is constant for a constant heat load. Having a higher heated fuel temperature, using the LMTD method, will lead to a better exchange at the SHX level. Thus, the heat transfer rate in this station will be higher as seen by the green curved line in Figure 4.14(a)).

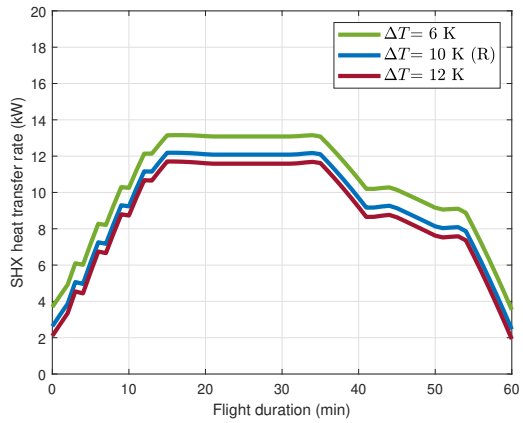

(a) SHX heat transfer rate.

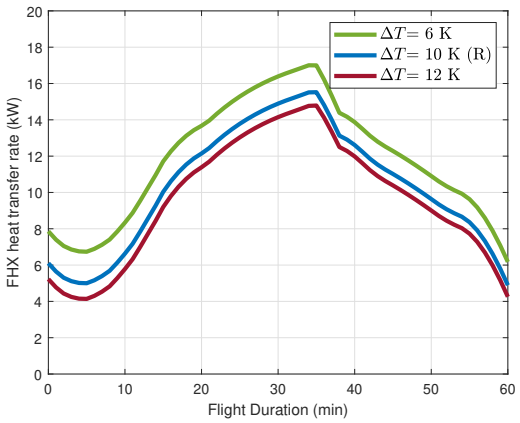

(b) FHX heat transfer rate.

Figure 4.14: Sensitivity HEX designed temperature difference for A5.

Although the inlet temperature is superior, the higher quantity of heat exchanged will result in an almost unchangeable fuel temperature after the skin heat exchanger station. Thus, there will be no significant differences in the temperature of the fuel in the tank. Since the temperature of the tank will remain basically constant for the different cases, the FHX heat transfer rate will only be influenced by the design temperature difference. This way, having an identical fuel inlet temperature (from the tank) and a higher designed fuel outlet temperature (for $\Delta T_1 = 6$ K), the heat transfer rate through the FHX will be slightly higher for this case as presented by the green curved line in Figure 4.14(b). Only a small difference of less than 1 K in the FHX liquid outlet temperature is registered.

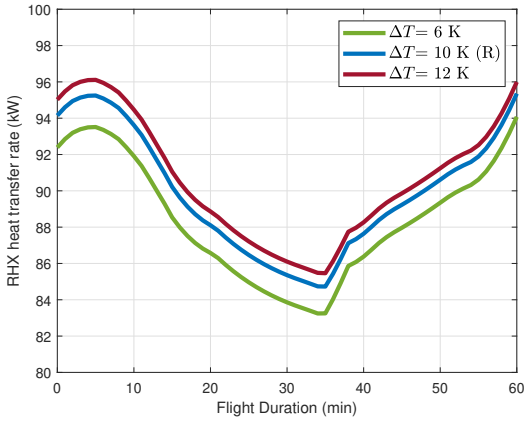

(a) RHX heat transfer rate.

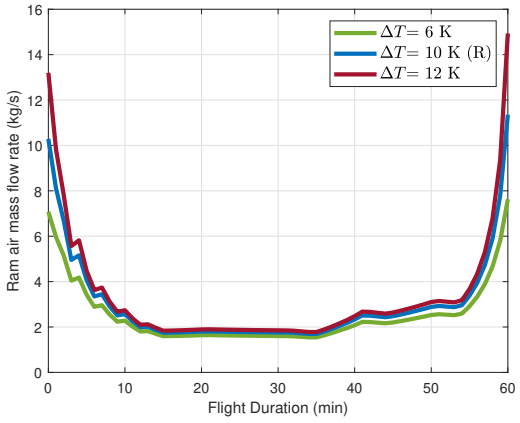

(b) Ram air mass flow rate.

Figure 4.15: Sensitivity HEX designed temperature difference for A5.

The RHX behaviour will be influenced not only by the heat that has already been dissipated in the FHX but also by the different design temperature difference. For $\Delta T_1 = 6$ K, the heat rejected in the FHX is superior and consequently less heat needs to be removed by the ram air inlet (green curved line in Figure 4.15(a)). Since the difference in EGW (coming from FHX station) inlet temperature is negligible (less than 1 K), for $\Delta T_1 = 6$ K, a greater ram air outlet temperature can be achieved (around 3 K higher when compared to the baseline). The lower amount of heat being transferred to the ram air and the higher

air design outlet temperature both contribute to a reduction in the ram air mass flow required for the case of $\Delta T_1 = 6$ K, especially during take-off and landing (green curved line in Figure 4.15(b)).

The impact of this design parameter is presented in Table 4.9. The difference in the system mass (reduction up to 9%) is mainly due to the fan contribution. Because of the smaller amount of ram air mass flow during TO and L for $\Delta T_1 = 6\ K$, this case will have lower fan mass and lower overall system mass. Again, the energy consumption and drag notorious decrease for $\Delta T_1 = 6\ K$ can be explained by the fact that a considerable lower amount of RA is being pulled into the aircraft.

Table 4.9: Sensitivity analysis of the HEX temperature difference on the mass, drag and energy consumption for A5.

Results	ΔT_1= 6 K	ΔT_1= 10 K (R)	ΔT_1= 12 K	Max. reduction
Mass (kg)	545.527	596.208	653.380	9%
Energy consumption (MJ)	30.72	32.511	34.270	6%
CR Drag penalty (N)	241.109	263.448	275.989	8.5%
TO Drag penalty (N)	593.046	856.549	1095.293	30%

Recirculation fuel flow rate

The mass flow rate recirculating to the fuel tank influences the behaviour of the system stations of architecture 5. In this stage, different fuel mass flow rates are considered, specifically $\dot{m}_r = 0.15$ kg/s, $\dot{m}_r = 0.17$ kg/s and $\dot{m}_r = 0.2$ kg/s, to quantify its influence.

Rising the recirculation mass flow to $\dot{m}_r = 0.2$ kg/s, will increase the SHX cooling capacity as presented by the red curved line in Figure 4.16(a). However, the mass flow that needs to be cooled is higher. These two conflicting contributions result in a small increase in the cooled fuel temperature for this operating condition. For the tank, an increase in both the mass flow entering and the entry temperature is verified. The effect is going to be an increase in the fuel temperature in the tank during the whole flight (red curved line in Figure 4.16(b)).

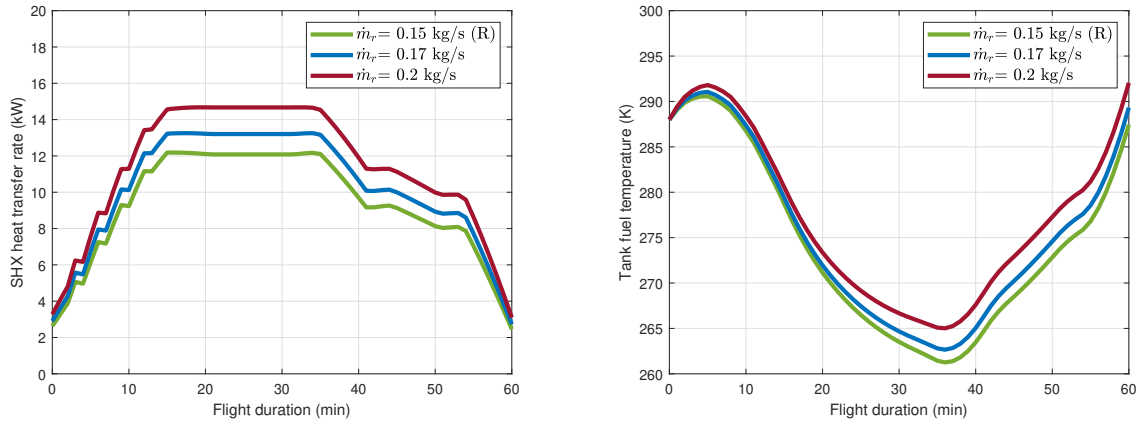

(a) SHX heat transfer rate.

(b) Tank fuel temperature.

Figure 4.16: Sensitivity analysis of the fuel recirculation mass flow rate for A5.

Regarding the FHX, for the case of $\dot{m}_r = 0.2$ kg/s, the mass flow is larger (favourable for heat transfer), but the tank temperature is higher (unfavourable for heat transfer). The contradictory trends result in a small increase in the heat transfer capacity of the FHX for larger recirculation mass flow rates. Increasing the heat that is transferred from the EGW to the fuel means that the RHX required cooling capacity is lower and the same applies to the ram air mass flow.

Table 4.10 highlights the most important results of this parametric study. Since the variation of $\dot{m}_r$ in the range considered results only in small changes in the heat transfer rate of the different heat stations and in the ram air mass flow required, no significant impact is registered in terms of mass and drag. The main contributions for the mass increase for $\dot{m}_r = 0.2$ kg/s are the up-sized fuel pump and fuel ducts. In terms of drag, a smaller impact is registered for $\dot{m}_r = 0.2$ kg/s since less RA is needed as stated before. Regarding energy consumption, in this case, it is mainly influenced by two components: the fan and the fuel pump. The work required by the fan to pull the ram air is inferior using $\dot{m}_r = 0.2$ kg/s. However, the work to pump a larger fuel mass flow is superior. The total system energy ends up being 9% higher for $\dot{m}_r = 0.2$ kg/s (fuel pump has a major contribution).

Table 4.10: Sensitivity analysis of the recirculation fuel mass flow rate on the mass, drag and energy consumption for A5.

Results	$\dot{m}_r = 0.15$ kg/s (R)	$\dot{m}_r = 0.17$ kg/s	$\dot{m}_r = 0.2$ kg/s	Max. reduction [1]
Mass (kg)	596.208	597.495	599.487	-0.55%
Energy consumption (MJ)	32.511	35.604	40.246	-23.8%
CR Drag penalty (N)	263.448	261.140	258.290	2%
TO Drag penalty (N)	856.549	855.234	853.241	0.3%

Tank parameters

For the fuel thermal management system of A5, the fuel tank dimensions and parameters, namely its dimensions and the overall heat resistance of the tank walls, affect the fuel temperature in the tank and consequently all the TMS behaviour. To study the influence of the tank design variables three parametric studies are conducted: one regarding the global heat transfer coefficient of the tank walls and the others taking into account the overall dimensions (chord occupancy percentage and wingspan occupancy percentage).

The results of the sensitivity analysis of the tank heat transfer coefficient are presented in Figure 4.17.

By increasing the global heat transfer coefficient between the fuel in the tank and the atmospheric air (U_{wall}), the thermal wall resistance decreases and the heat transfer between the fuel and the air is enhanced. With that said, it is expected that the absolute value of $\dot{Q}_{\text{loss}}$ is higher for U_{wall} =50 W/Km^2. The red curved line in Figure 4.17(a) shows this:

- For negative values of $\dot{Q}_{\text{loss}}$, i.e., in cases where the fuel in the tank is receiving heat from the atmospheric air, U_{wall} =50 W/Km^2 presents more negative (higher absolute) values;

[1] To note that the negative values of reduction represent the maximum increase of the metrics since no reduction compared to the reference case can be obtained in terms of drag and mass.

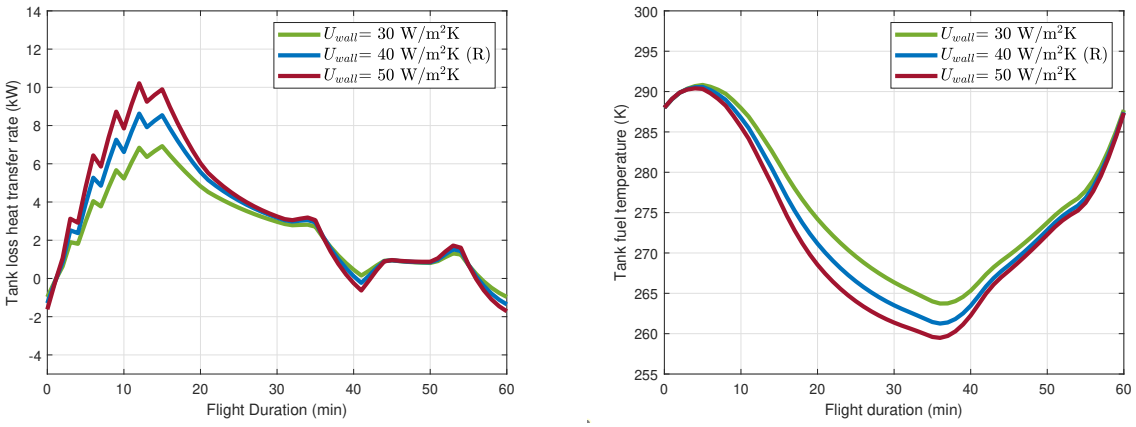

(a) Tank loss heat transfer rate.

(b) Tank fuel temperature.

Figure 4.17: Sensitivity analysis of the fuel recirculation mass flow rate for A5.

- For positive values of $\dot{Q}_{\text{loss}}$, i.e., in cases where fuel is losing heat for the atmospheric air, U_{wall} =50 W/Km^2 presents higher tank loss heat transfer rate values.

The evolution of the fuel temperature in the tank is presented in Figure 4.17(b). Since both $\dot{Q}_{\text{loss}}$ and fuel temperature are related it is expected that the fuel temperature for the case of U_{wall} =50 W/Km^2 is slightly higher when the fuel is receiving heat and lower when the fuel is rejecting as depicted in the graph. Only small differences are registered in terms of the temperature of the fuel in the tank and, although this will slightly influence the heat exchanged at FHX level, the overall impact on the mass, energy consumption and drag penalty is negligible.

There are other tank parameters that were set as design variables at the beginning of the simulation. The conceptual FutPrInt50 aircraft design still does not have a clear and precise fuel tank position and dimension. This way, the chord and wing occupancy percentages for the fuel tank were estimated based on some reference values. Shifting these values will cause the contact area between the fuel and atmospheric air to change. Consequently, different heat losses through the tank walls are expected. Increasing both chord and wingspan percentages is similar to increasing the value of U_{wall} but leads to slightly different magnitude results. Due to the high degree of similarity between these results and those of U_{wall}, they are not presented here.

Other parameters

In parallel with the above sensitivity analyses, there are other design variables, namely the length and thickness of the ducts, whose system impact is predictable, but must also be considered. Increasing the length of the ducts will, firstly, increase the total system mass and, secondly, increase the pressure drop of the fluids through their path. Accordingly, the pump work that needs to be done to ensure an unconstrained circulation is going to be higher. The thickness of the ducts only has an influence on the system mass, so it is expected to use thicker ducts to minimise the TMS mass impact.

4.4 Optimisation results

According to the parametric study presented in Section 4.3, the choice of some design variables has a great impact on the overall system. In this context, a multi-objective optimisation design problem is set up as described in Section 3.6. The objectives to minimise are the ones presented before: mass, energy consumption and drag. The drag results are estimated by integrating the drag profile throughout the whole mission time. A 3-D Pareto front was obtained for A2, A4 and A5 using the design variables described in Table A.1. For sake of brevity, only the results of cases 2 and 4 are presented in this section. Plots of 2D slices of the 3D problem are presented in Figures 4.18, 4.19 and 4.20 for a better understanding. Each figure compares A2 to A4.

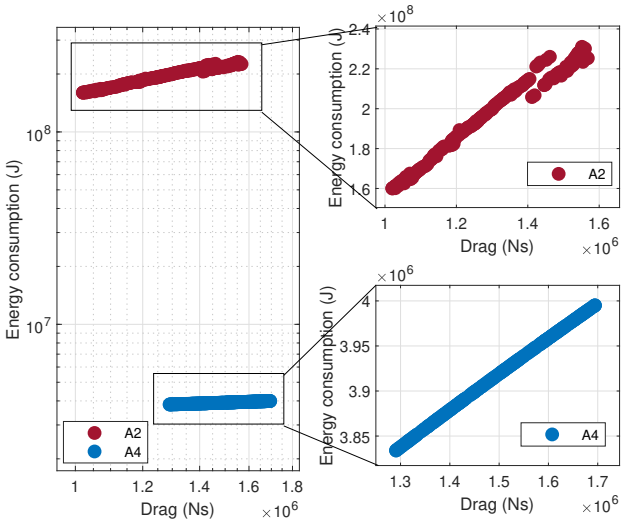

Figure 4.18: Pareto front for drag penalty and energy consumption (A4 versus A2).

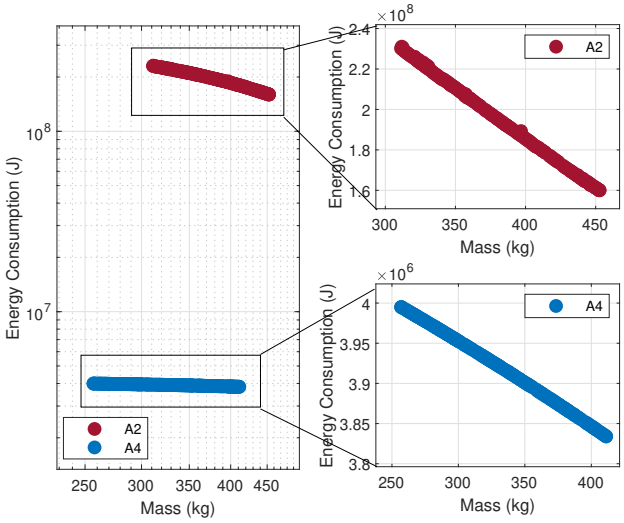

Figure 4.19: Pareto front for total mass and energy consumption (A4 versus A2).

According to the reference values presented in Table 4.4, the energy consumption in A2 is expected to be two orders of magnitude higher when compared to A4, due to the double compressor contribution

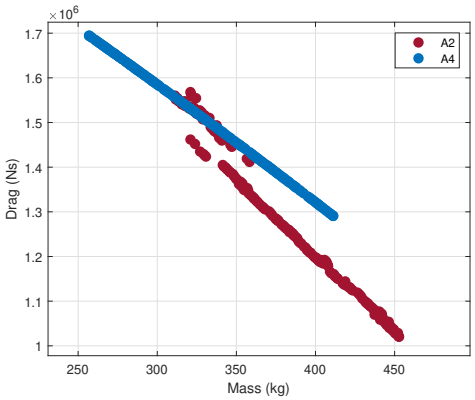

Figure 4.20: Pareto front for mass and drag penalty (A4 versus A2).

(one VCS for each side of the aircraft). This way the Pareto fronts related to the minimisation of energy consumption are presented in a logarithmic scale to better understand the difference between cases. A closer look at each case is also presented to clearly highlight the system behaviour.

The trade-off in the optimal layouts is the one expected. In the parametric studies was concluded that the variation of the three objective functions followed the same trend for most of the design variables, i.e, changing one design variable led to an increase or a decrease of all three functions. Only the skin heat exchanger area had the reverse effect: by increasing the skin heat exchanger area, the mass would increase, but both drag and energy consumption would decrease. With that said, all the design variables except the A_{SHX} tend to one of the limits of the range considered. Consequently, the Pareto fronts presented are mostly influenced by A_{SHX}.

Comparing the two architectures, looking at Figure 4.18, case A2 (identified by the red colour) can reach lower values of drag penalty for some design layouts, but has a much superior energy consumption. Figure 4.19 shows that, in terms of mass, A4 (identified by the blue colour) can reach lower values for much lower energy consumption. Lastly, Figure 4.20 validates the results presented before: A4 can be lighter but with a higher drag penalty when compared to A2. Therefore, the use of A4 to dissipate the hybrid-electric propulsion waste heat seems to be advantageous in terms of mass and energy consumption but creates a larger ram drag.

After the deterministic optimisation study, some variables carrying uncertainty were added to the problem to illustrate their importance in the design. First, the take-off temperature was considered raging between ISA$\pm$10 K. Secondly, the thickness of the external flow boundary layer was set to carry uncertainty due to the not well known behaviour of the boundary layer in flight. A variation of 5% with respect to the reference value was accounted. For clarity, only the results obtained for A4 are presented in Figures 4.21, 4.22 and 4.23. As expected, since the design is more robust, i.e, its performance is less sensitive to inherent variability, the maximum values obtained in the three domains are higher when compared to the deterministic results. This more effective strategy takes into account the unpredictability of operational conditions and optimises the predicted performance over a wide range of scenarios. The robust TMS design achieves a good performance even with uncertainty in the outside temperature and in the boundary layer thickness of the external flow.

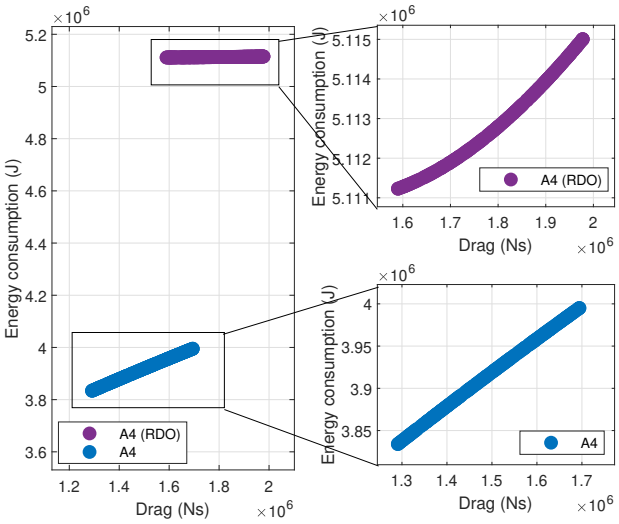

Figure 4.21: Pareto front for drag penalty and energy consumption (A4 versus A4 with uncertainty).

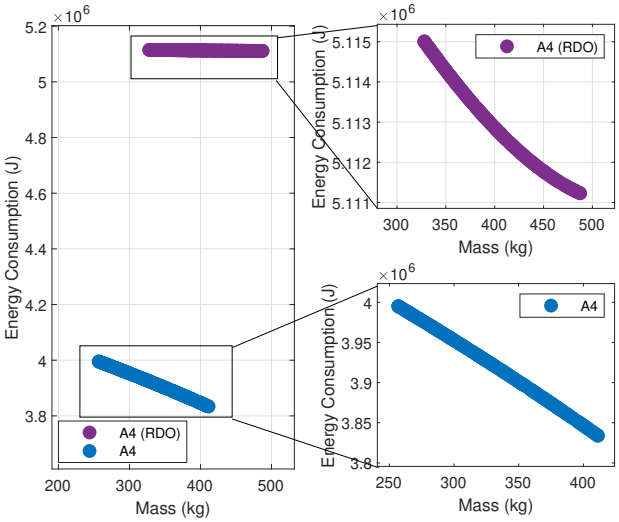

Figure 4.22: Pareto front for total mass and energy consumption (A4 versus A4 with uncertainty).

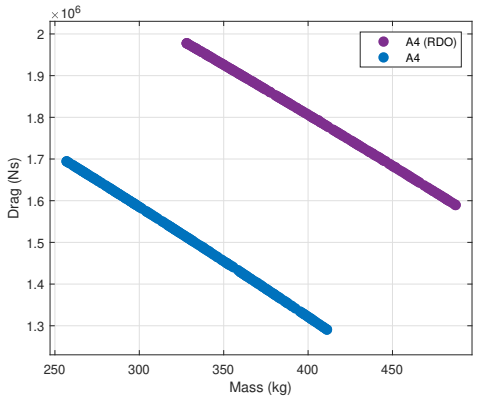

Figure 4.23: Pareto front for mass and drag penalty (A4 versus A4 with uncertainty).

In a further analysis, A5 was coupled with propulsive computational models created by Iara [18] and different optimisation studies were conducted. The optimisation models use the hybridisation factor as design variable and the series, parallel and turbo-electric architectures for propulsion (as presented in Figure 2.1). The optimisation is set to minimise: (i) the CO_2 emissions associated with the energy source and EGW production/recharge/consumption; and (ii) the combined mass of the HEP and TMS. Different hybridisation factors influence the power required by the various components in the powertrain and consequently the power dissipation values throughout the flight and the mass flow of fuel required by the engine, which are used as inputs of the TMS. Figure 4.24 shows the NSGA-II optimisation results for a population of 50 individuals. Three different cases are presented here and a more detailed analysis of this topic can be found in [18]:

- **Case 1 (green marks):** Using SAF in an optimistic scenario, described in Table A.2, where EGW is obtained from biomass and the battery is recharged in Sweden. The TMS manages the heat from the battery, the electric motor/generator and the gearbox.
- **Case 2 (red marks):** Using SAF in a pessimistic scenario, described in Table A.2, considering EGW from coal and the electric grid of the European Union. The TMS handles the heat from the battery, the electric motor/generator and the gearbox.
- **Case 3 (blue marks):** The same considerations as for Case 1, except for the fact that now the TMS is also responsible for managing the power dissipated by the ICE.

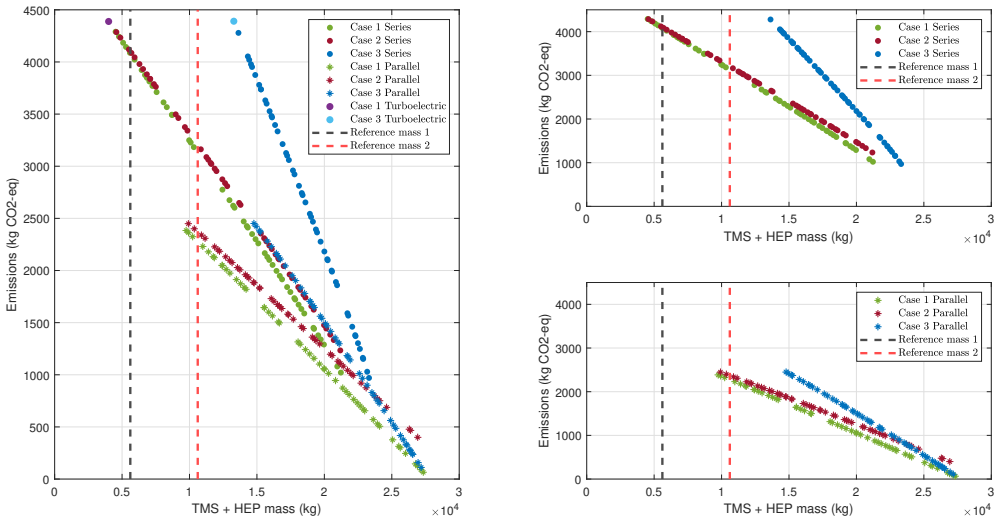

Figure 4.24: Pareto front for HEP and TMS (A5) total mass and CO_2 emissions mass - Overall, series and parallel cases.

To explain the overall Pareto behaviour, it is worth mentioning that the battery pack has the largest influence in terms of mass, while the fuel flowing to the ICE has the largest influence in terms of CO_2 emissions. A greater hybridisation factor, will increase the power required from the battery. This will lead to a large mass penalty, while bringing an advantage in terms of CO_2 emissions (less impact in terms of fuel production and consumption on the ICE level).

Comparing both green and red trends corresponding to the optimistic (Case 1) and pessimistic (Case 2) scenarios, respectively, the result is the one expected. For the pessimistic scenario, an increase in emissions for the same mass of HEP and TMS is registered. This increase is greater for a higher hybridisation factor, due to the greater dependence on fossil energy for recharging the batteries.

Looking at the different propulsive architectures, important remarks can be made. Even though the parallel powertrain is preferable when compared to the series case in terms of emissions, it has a higher mass penalty. This, again, can be justified by the battery impact. According to Figure 2.1 and to the electrical branch chain, the power required to the battery pack is higher for the parallel case. This way, the system will be heavier for all the hybridisation factors and the turboshaft will be downsized leading to fewer emissions. The turboelectric architecture is similar to the series architecture but does not include a battery in the powertrain. When comparing the turboelectric case and the lowest hybridisation factor series case, it can be seen that the CO_2 emissions and the overall mass are identical. This is because the series case for a hybridisation factor of 0% corresponds to the turboelectric architecture. In the optimisation simulation, the random design space ended up not including a hybridisation factor of 0%. Otherwise, the corresponding series result would coincide with the turboelectric result.

In Case 3, the turboshaft efficiency is around 30% as in a typical thermodynamic cycle. For this scenario, the TMS has significantly more heat that needs to be managed for lower hybridisation factors. The current externally exposed turboshafts already have efficient refrigeration systems. However, the shift to an electric powertrain might lead to the integration of the ICE into the fuselage, making it harder for the heat generated to be removed. Thus, the TMS mass and the liquid production CO_2 impact become higher when compared to Case 1 or Case 2 in all propulsive architectures. The TMS trend in terms of mass and emissions is the reverse of the one shown in Figure 4.24 for Case 3, but not significant enough to impact the contribution of battery and fuel and invert the Pareto front evolution.

Two important mass references are added to this analysis. The reference mass represented by the black dashed line indicates the propulsion mass for a similar aircraft. This value was set to 31% of the MTOW of FutPrInt50 aircraft [111], considering the mass of the engines, propellers and fuel of the ATR42-600. The zone on the right side of the reference line gives ambitious values of CO_2 emissions by increasing the power required by the battery, but unrealistic values in terms of the maximum propulsive mass. Only the series architecture can reach the realistic zone (left side of the black dashed line) for hybridisation factors ranging between 0 and 9%. The red dashed line represents a corrected mass feasible zone for the HEP+TMS system in the case that the 5000 kg of passengers payload is eliminated and the propulsive and thermal system mass can reach higher values. For this case, both series and parallel architectures remain in the acceptable zone for a hybridisation factor of 36% and 6%, respectively. To design a coupled HEP and TMS system it is advisable to use hybridisation factors that keep both objective functions in the realistic zone. Noting that there is no mass constraint imposed on the system as a whole, these findings should be analysed with care, since the same aerodynamic properties are being evaluated and the mass is rising. This leads to the conclusion that a multidisciplinary effort with other relevant aircraft design disciplines, namely aerodynamics and structures is of extreme importance.

Chapter 5

Conclusions

This chapter contains the final conclusions of this thesis, its major accomplishments, and recommendations for future work.

5.1 Achievements

Design for sustainability is becoming one of the primary motivators for the next generation aircraft. Providing adequate thermal management is anticipated to be a significant design challenge for future aircraft using electric propulsion. The objective of FutPrInt50 project is to explore and find answers to these challenges. Thus, within this context, the goal of this study was to design and implement several potential thermal management architectures for a more electric propulsion system, while addressing the key research questions outlined in Chapter 1.

The research started by reviewing several models for calculating the cooling capabilities of different heat sinks in order to assist the design and optimisation of the TMS for the increasingly severe thermal management challenges of current hybrid-electric aircraft. The three main heat dissipation components include fuel, ram air and the use of the aircraft skin. Using the identified main heat sinks (atmosphere and fuel), five different thermal management architectures using multiple heat transfer technologies have been proposed. The modelling and simulation of the systems were conducted on Matlab and Simulink and were based on the physics of heat transfer within a closed channel system with EGW as the principal fluid. Newton's cooling law, the log-mean temperature difference method for designing heat exchangers, first law of thermodynamics and external flow empirical methods are some examples of the modelling principles used. Also, validation and evaluation of the methodology proposed and developed were conducted using data available in the open literature.

The systems were analysed based on the heat transfer rate potential and the managed fluid temperatures were determined at each heat sink station and compared. The overall system mass, drag penalty and energy consumption for each are also analysed. This research revealed that a heat sink is more desirable when its cooling capacity is greater while its mass, drag, and power impact are smaller. The cooling capacity of each heat sink is also not only dependent on its design characteristics and thermophysical states, but also on the flight conditions.

Regarding the main three components considered, it is important to highlight the following findings:

(1) **Fuel** is one of the most significant heat sinks in current aircraft but its cooling capacity is restricted by the mass of the tank. Given the trends of less on-board fuel and high thermal loads, it is going to be hard to meet the cooling requirements and safety issues may arise;

(2) **Ram air** has a great cooling capacity, since large external air mass flows can be theoretically pulled into the aircraft. The problem is that it will inevitably introduce an additional drag penalty depending on the thermal loads being dissipated. Also, the current heat exchangers can not manage large mass flows as the initial mass flow required to cool the load considered in this work. A rearrangement of multiple RHXs would be needed;

(3) **SHX** is insufficient itself for advanced modern aircraft due to limits in the fuselage size and available area for the mission here considered. It would be more beneficial for long and medium hauls with longer cruise phases when the atmospheric properties are favourable to the heat transfer. Simultaneously, the increasing use of composite airframes has decreased the likelihood of removing excess heat waste through the aeroplane skin, because the thermal conductivity of these materials is typically lower when compared to the metallic materials.

The next phase passed through a parametric study that provided a comprehensive sensitivity analysis of the design variables in order to increase the performance of each architecture, facilitating the integration of the TMS in future hybrid propulsion aircraft. With the insights from the parametric study, a multi-objective optimisation model using a genetic algorithm was then formulated. The established method describes how a design can be optimised to minimise TMS drag, weight, and energy consumption. The results showed a more clear comparison between the different architectures in terms of the three objective functions. The five architectures were compared and the following conclusions can be drawn.

(1) A1 and A2 have large power consumption penalties because they introduce two vapour compression systems and the compressor work in each of them is considerable. Besides, these two architectures seem a good option in terms of both drag penalty and mass, especially A1 because it does not consider the SHX (adds additional mass). In terms of ram air, the value is relatively low when compared to the other architectures given the higher working temperature of the refrigerant.

(2) Configurations A3 and A4 present good results in terms of energy consumption and drag penalty (especially during cruise). The problem with these systems is the high ram air mass flow rate required during take-off and landing, making it hard to manage using only one exchanger and setting these flight phases as critical points. This also creates a higher drag penalty during these segments.

(3) The difference between A2 and A4 (from different cooling families) was emphasised during the optimisation study. The use of A4 to dissipate the hybrid-electric propulsion architecture heat load seemed advantageous in terms of mass and energy consumption, reaching lower values for some design variables, but creating a larger drag penalty. It is worth mentioning the importance of considering uncertainty in the design in order to make it robust.

(4) Configuration A5, due to the higher number of components, has a greater impact on the overall mass. Additionally, with the design conditions used, the fuel heat exchanger does not have much heat rejection capacity leading to a high quantity of ram air required during both take-off and landing at the RHX level. The power consumption is slightly higher compared to A3 and A4 because there is a need for a fuel pump to recirculate fuel again to the fuel tank. The use of the SHX in the wing also seems a worse option when compared to the fuselage location due to the influence of the external Reynolds number on the overall convective heat transfer coefficient.

From this study, it was found that none of the investigated architectures performs ideally across all of the studied metrics. Thus, when designing the TMS for future HEA, different architectures must be analysed and the different objective functions must be evaluated so they can be prioritised according to the different power requirements and design needs. The direct integration in early design phases of the TMS and HEP system, as done in the last section of this work, is of extreme importance to study the feasibility of this aircraft concept. A multidisciplinary effort with other relevant aircraft design disciplines, including aerodynamics and structures, must also be conducted.

5.2 Future work and recommendations

Several assumptions and simplifications have been made in this research to restrict its scope. The corresponding limitations have led to the following suggestions and recommendations for future work:

- **Develop a high fidelity model for the ram air system** to obtain a more accurate estimation of the drag coefficient penalty of RA systems, and consequently, the impact on fuel consumption.
- **Integration of the TMS closely with the propulsive architecture** to benefit from synergies between each other and obtain a more precise estimation of the heat load. Multidisciplinary analyses addressing aerodynamics and structures may also be accounted for.
- **Model the liquid pressure losses through the different components adequately** to achieve a more reliable impact on the pumping power consumption.
- **Model the volumetric representation and positioning of the aircraft components in more detail**. By imposing restrictions on where components can be put and taking installation regulations into consideration, a more accurate volumetric and mass impact can be achieved.
- **Evaluate aircraft heat flux distribution through CFD simulations** instead of using semi-empirical external flow heat transfer models.
- **Implementing a phase change material as a thermal management system** to evaluate if it is possible to eliminate the need for a heat exchanger or pump in the system, and compare the system performance to the already implemented architectures.
- **Comparative study under the model developed with different coolants** and, eventually, using novel fluids, such as nanofluids, and additives to enhance the heat transfer.

Bibliography

[1] B. Graver, D. Rutherford, and S. Zheng. CO_2 Emissions from Commercial Aviation 2013, 2018, and 2019. International Council on Clean Transportations, 2020. URL `https://theicct.org/sites/default/files/publications/CO2-commercial-aviation-oct2020.pdf`.

[2] European Commission. *Flightpath 2050 vision for European aviation*. Publications Office of the European Union, Luxembourg, 2011. ISBN 978-92-79-19724-6.

[3] D. Lee, D. Fahey, A. Skowron, M. Allen, U. Burkhardt, Q. Chen, S. Doherty, S. Freeman, P. Forster, J. Fuglestvedt, A. Gettelman, R. De León, L. Lim, M. Lund, R. Millar, B. Owen, J. Penner, G. Pitari, M. Prather, R. Sausen, and L. Wilcox. The contribution of global aviation to anthropogenic climate forcing for 2000 to 2018. *Atmospheric Environment*, 244:117834, 2021. doi:10.1016/j.atmosenv.2020.117834.

[4] M. A. Rendón, C. D. Sánchez R., J. Gallo M., and A. H. Anzai. Aircraft Hybrid-Electric Propulsion: Development Trends, Challenges and Opportunities. *Journal of Control, Automation and Electrical Systems*, 32:1244–1268, 2021. doi:10.1007/s40313-021-00740-x.

[5] F. Afonso, M. Sohst, C. M. A. Diogo, S. S. Rodrigues, A. Ferreira, I. Ribeiro, R. Marques, F. F. C. Rego, A. Sohouli, J. Portugal-Pereira, H. Policarpo, B. Soares, B. Ferreira, E. Fernandes, F. Lau, and A. Suleman. Strategies towards a more sustainable aviation: a systematic review. Submitted to *Progress in Aerospace Sciences*, 2022.

[6] B. J. Brelje and J. R. Martins. Electric, hybrid, and turboelectric fixed-wing aircraft: A review of concepts, models, and design approaches. *Progress in Aerospace Sciences*, 104:1–19, 2019. doi:10.1016/j.paerosci.2018.06.004.

[7] R. Jansen, C. Bowman, S. Clarke, D. Avanesian, P. Dempsey, and R. Dyson. NASA electrified aircraft propulsion efforts. *Aircraft Engineering and Aerospace Technology*, 92(5):667–673, 2020. doi:10.1108/AEAT-05-2019-0098.

[8] A. Barke, C. Thies, S. P. Melo, F. Cerdas, C. Herrmann, and T. S. Spengler. Comparison of conventional and electric passenger aircraft for short-haul flights – a life cycle sustainability assessment. *Procedia CIRP*, 105:464–469, 2022. doi:10.1016/j.procir.2022.02.077.

[9] A. N. Srinath, Álvaro Pena López, S. A. Miran Fashandi, S. Lechat, G. di Legge, S. A. Nabavi, T. Nikolaidis, and S. Jafari. Thermal Management System Architecture for Hydrogen-Powered

Propulsion Technologies: Practices, Thematic Clusters, System Architectures, Future Challenges, and Opportunities. *Energies*, 15(1):304, 2022. doi:10.3390/en15010304.

[10] C. Perullo, A. Alahmad, J. T. Wen, M. D'Arpino, M. Canova, D. N. Mavris, and M. Benzakein. Sizing and Performance Analysis of a Turbo-Hybrid-Electric Regional Jet for the NASA ULI Program. In *2019 AIAA/IEEE Electric Aircraft Technologies Symposium (EATS)*, Indianapolis, IN, USA, 2019. doi:10.2514/6.2019-4490.

[11] A. van Heerden, D. Judt, S. Jafari, C. Lawson, T. Nikolaidis, and D. Bosak. Aircraft thermal management: Practices, technology, system architectures, future challenges, and opportunities. *Progress in Aerospace Sciences*, 128:100767, 2022. doi:10.1016/j.paerosci.2021.100767.

[12] W. Affonso, R. Gandolfi, R. J. N. dos Reis, C. R. I. da Silva, N. Rodio, T. Kipouros, P. Laskaridis, A. Chekin, Y. Ravikovich, N. Ivanov, L. Ponyaev, and D. Holobtsev. Thermal management challenges for HEA – FUTPRINT 50. *IOP Conference Series: Materials Science and Engineering*, 1024(1): 012075, 2021. doi:10.1088/1757-899x/1024/1/012075.

[13] D. Eisenhut, E. Windels, R. Reis, D. Bergmann, C. Ilário, F. Palazzo, and A. Strohmayer. Foundations towards the future: FutPrInt50 TLARs an open approach. *IOP Conference Series: Materials Science and Engineering*, 1024(1):012069, 2021. doi:10.1088/1757-899x/1024/1/012069.

[14] J. Hoelzen, Y. Liu, B. Bensmann, C. Winnefeld, A. Elham, J. Friedrichs, and R. Hanke-Rauschenbach. Conceptual Design of Operation Strategies for Hybrid Electric Aircraft. *Energies*, 11(1):217, 2018. doi:10.3390/en11010217.

[15] N. Madavan, J. Heidmann, C. Bowman, P. Kascak, A. Jankovsky, and R. Jansen. A NASA perspective on electric propulsion technologies for commercial aviation. In *ESARS-ITEC 2016, Toulouse, France*, November 2016. URL `https://ntrs.nasa.gov/api/citations/20180008723/downloads/20180008723.pdf`.

[16] A. Schwab, A. Thomas, J. Bennett, E. Robertson, and S. Cary. Electrification of Aircraft: Challenges, Barriers, and Potential Impacts. *National Renewable Energy Laboratory (NREL)*, 2021. doi:10.2172/1827628.

[17] W. Affonso, R. Tavares, F. R. Barbosa, R. Gandolfi, R. J. N. dos Reis, C. R. I. da Silva, T. Kipouros, P. Laskaridis, H. B. Enalou, A. Chekin, A. Kukovinets, K. Gubernatorov, Y. Ravikovich, N. Ivanov, L. Ponyaev, and D. Holobtsev. System architectures for thermal management of hybrid-electric aircraft - FutPrInt50. *IOP Conference Series: Materials Science and Engineering*, 1226(1):012062, 2022. doi:10.1088/1757-899x/1226/1/012062.

[18] I. A. A. Figueiras. Development of computational models for hybrid-electric propulsive systems. MSc Thesis in Aerospace Engineering, Instituto Superior Técnico, Lisbon, Portugal, 2022.

[19] International Air Transport Association. *Aircraft Technology Roadmap to 2050*. 2019. International Air Transport Association: Montreal, QC, Canada.

[20] J. L. Felder. NASA Electric Propulsion System Studies. In *EnergyTech 2015*, Cleveland, OH, USA, 2016.

[21] C. Pornet and A. Isikveren. Conceptual design of hybrid-electric transport aircraft. *Progress in Aerospace Sciences*, 79:114 – 135, 2015. doi:10.1016/j.paerosci.2015.09.002.

[22] T. Sinnige, N. van Arnhem, T. C. A. Stokkermans, G. Eitelberg, and L. L. M. Veldhuis. Wingtip-Mounted Propellers: Aerodynamic Analysis of Interaction Effects and Comparison with Conventional Layout. *Journal of Aircraft*, 56(1):295–312, 2019. doi:10.2514/1.C034978.

[23] M. Drela. Power Balance in Aerodynamic Flows. *AIAA Journal*, 47(7):1761–1771, 2009. doi:10.2514/1.42409.

[24] M. L. Celestina and M. J. Long-Davis. Large-scale boundary layer ingesting propulsor research. In *International Society for Air Breathing Engines (ISABE) Conference*, Canberra, Australia, 09 2019.

[25] HERRACUS project. State-of-the-art technologies on research and developments underway in the field of alternative propulsion architectures. https://ec.europa.eu/research/participants/documents/downloadPublic?documentIds=080166e5cdaeb892&appId=PPGMS, March 2020.

[26] Zunum Aero Technology. https://zunum.aero/technology/, 2022. Accessed: 2022-07-10.

[27] PEGASUS Activity Summary. https://sacd.larc.nasa.gov/asab/asab-projects-2/pegasus/, 2022. Accessed: 2022-07-10.

[28] ECO4: New generation hybrid-electric four place aircraft. http://sustainableaviation.org/sas2017/session/eco4-new-generation-hybrid-electric-four-place-aircraft/index.html, 2017. Accessed: 2022-07-10.

[29] Boeing: Build a Better Planet. https://www.boeing.com/aboutus/environment/environment_report_14/2014_environment_report.pdf, 2014. Accessed: 2022-07-10.

[30] J. K. Nøland. Hydrogen electric airplanes: A disruptive technological path to clean up the aviation sector. *IEEE Electrification Magazine*, 9(1):92–102, 2021. doi:10.1109/MELE.2020.3047173.

[31] NASA: Single-Aisle Turboelectric Aircraft with Aft Boundary Layer Propulsion. https://www1.grc.nasa.gov/aeronautics/eap/airplane-concepts/starc-abl/, 2022. Accessed: 2022-07-10.

[32] ESAero ECO-150:Project overview. https://www.esaero.com/eco-150-project-information, 2022. Accessed: 2022-07-10.

[33] NASA. NASA N3-X with turboelectric distributed propulsion. https://ntrs.nasa.gov/api/citations/20150002081/downloads/20150002081.pdf, 2014. Accessed: 2022-07-10.

[34] Eviation. Alice Aircraft. https://www.eviation.co/aircraft/, 2022. Accessed: 2022-07-10.

[35] NASA. X-57 Technical Papers. https://www.nasa.gov/aeroresearch/X-57/technical/index.html, 2021. Accessed: 2022-07-10.

[36] S. Stückl, J. van Toor, and H. Lobentanzer. Voltair-the All Electric Propulsion Concept for Atmospheric Platform – A Vision for Atmospheric Friendly Flight. In *28th International Congress of the Aeronautical Sciences (ICAS)*, Brisbane, Australia, September 2012.

[37] I. Geiß and R. Voit-Nitschmann. Sizing of fuel-based energy systems for electric aircraft. *Proceedings of the Institution of Mechanical Engineers, Part G: Journal of Aerospace Engineering*, 231(12): 2295–2304, 2017. doi:10.1177/0954410017721254.

[38] C. Silva, W. Johnson, E. Solis, M. Patterson, and K. Antcliff. VTOL Urban Air Mobility Concept Vehicles for Technology Development. In *2018 Aviation Technology, Integration, and Operations Conference*, Atlanta, Georgia, USA, June 2018. doi:10.2514/6.2018-3847.

[39] W. Johnson and C. Silva. NASA concept vehicles and the engineering of advanced air mobility aircraft. *The Aeronautical Journal*, 126(1295):59–91, 2022. doi:10.1017/aer.2021.92.

[40] B. T. Schiltgen and J. Freeman. Aeropropulsive Interaction and Thermal System Integration within the ECO-150: A Turboelectric Distributed Propulsion Airliner with Conventional Electric Machines. In *16th AIAA Aviation Technology, Integration, and Operations Conference*, Washington, DC, USA, June 2016. doi:10.2514/6.2016-4064.

[41] M. D. Patterson, J. M. Derlaga, and N. K. Borer. High-lift propeller system configuration selection for NASA's SCEPTOR distributed electric propulsion flight demonstrator. In *16th AIAA Aviation Technology, Integration, and Operations Conference*, Washington, DC, USA, June 2016. doi:10.2514/6.2016-3922.

[42] J. Sousa, L. Villafañe, and G. Paniagua. Thermal analysis and modeling of surface heat exchangers operating in the transonic regime. *Energy*, 64:961–969, 2014. doi:10.1016/j.energy.2013.11.032.

[43] E. Cabrera and J. Melo de Sousa. Use of Sustainable Fuels in Aviation—A Review. *Energies*, 15: 2440, 03 2022. doi:10.3390/en15072440.

[44] International Civil Aviation Organization.Sustainable Aviation Fuels (SAF). Alice Aircraft. https://www.icao.int/environmental-protection/pages/SAF.aspx, 2022. Accessed: 2022-07-13.

[45] I. Abrantes, A. F. Ferreira, A. Silva, and M. Costa. Sustainable aviation fuels and imminent technologies - CO2 emissions evolution towards 2050. *Journal of Cleaner Production*, 313:127937, 2021. doi:10.1016/j.jclepro.2021.127937.

[46] D. Chiaramonti. Sustainable aviation fuels: the challenge of decarbonization. *Energy Procedia*, 158:1202–1207, 2019. doi:10.1016/j.egypro.2019.01.308.

[47] S. Brynolf, M. Taljegard, M. Grahn, and J. Hansson. Electrofuels for the transport sector: A review of production costs. *Renewable and Sustainable Energy Reviews*, 81:1887–1905, 2018. doi:10.1016/j.rser.2017.05.288.

[48] M. Millinger, P. Tafarte, M. Jordan, A. Hahn, K. Meisel, and D. Thrän. Electrofuels from excess renewable electricity at high variable renewable shares: cost, greenhouse gas abatement, carbon use and competition. *Sustainable Energy Fuels*, 5:828–843, 2021. doi:10.1039/D0SE01067G.

[49] A. Bauen, N. Bitossi, L. German, A. Harris, and K. Leow. Sustainable aviation fuels. *Johnson Matthey Technology Review*, 01 2020. doi:10.1595/205651320X15816756012040.

[50] A. G. Rao, F. Yin, and H. G. Werij. Energy Transition in Aviation: The Role of Cryogenic Fuels. *Aerospace*, 7(12):181, 2020. doi:10.3390/aerospace7120181.

[51] B. J. Brelje and J. R. R. A. Martins. Aerostructural Wing Optimization for a Hydrogen Fuel Cell Aircraft. In *AIAA Scitech 2021 Forum*, Virtual Event, January 2021. doi:10.2514/6.2021-1132.

[52] Z. Pan, L. An, and C. Wen. Recent advances in fuel cells based propulsion systems for unmanned aerial vehicles. *Applied Energy*, 240:473–485, 2019. doi:10.1016/j.apenergy.2019.02.079.

[53] D. Pal and M. Severson. Liquid cooled system for aircraft power electronics cooling. In *16th IEEE Intersociety Conference on Thermal and Thermomechanical Phenomena in Electronic Systems (ITherm)*, Orlando, FL, USA, July 2017. doi:10.1109/ITHERM.2017.7992568.

[54] J. Freeman, P. Osterkamp, M. Green, A. Gibson, and B. Schiltgen. Challenges and opportunities for electric aircraft thermal management. *Aircraft Engineering and Aerospace Technology*, 86: 519–524, 2014. doi:10.1108/AEAT-04-2014-0042.

[55] M. Boll, M. Corduan, S. Biser, M. Filipenko, Q. H. Pham, S. Schlachter, P. Rostek, and M. Noe. A holistic system approach for short range passenger aircraft with cryogenic propulsion system. *Superconductor Science and Technology*, 33(4):044014, 2020. doi:10.1088/1361-6668/ab7779.

[56] D. Dezhin, I. Dezhina, and R. Ilyasov. Superconducting propulsion system with LH2 cooling for all-electric aircraft. *Journal of Physics: Conference Series*, 1559(1):012143, 2020. doi:10.1088/1742-6596/1559/1/012143.

[57] R. Wrobel. Thermal management of electrical machines for propulsion –challenges and future trends. *Archives of Electrical Engineering*, 71(1):175–187, 2022. doi:10.24425/aee.2022.140204.

[58] F. Zhang, L. Zhai, L. Zhang, M. Yi, B. Du, and S. Li. A novel hybrid battery thermal management system with fins added on and between liquid cooling channels in composite phase change materials. *Applied Thermal Engineering*, 207:118198, 2022. doi:10.1016/j.applthermaleng.2022.118198.

[59] S. Sahoo, X. Zhao, and K. Kyprianidis. A Review of Concepts, Benefits, and Challenges for Future Electrical Propulsion-Based Aircraft. *Aerospace*, 7(4):44, 2020. doi:10.3390/aerospace7040044.

[60] M. Ramezanizadeh, M. Alhuyi Nazari, M. Hossein Ahmadi, and L. Chen. A review on the approaches applied for cooling fuel cells. *International Journal of Heat and Mass Transfer*, 139: 517–525, 2019. doi:10.1016/j.ijheatmasstransfer.2019.05.032.

[61] S. H. Teichel, M. Dörbaum, O. Misir, A. Merkert, A. Mertens, J. R. Seume, and B. Ponick. Design considerations for the components of electrically powered active high-lift systems in civil aircraft. *CEAS Aeronautical Journal*, 6:49–67, 2014. doi:10.1007/s13272-014-0124-1.

[62] Y.-F. Mao, Y.-Z. Li, J.-X. Wang, K. Xiong, and J.-X. Li. Cooling Ability/Capacity and Exergy Penalty Analysis of Each Heat Sink of Modern Supersonic Aircraft. *Entropy*, 21(3):223, 2019. doi:10.3390/e21030223.

[63] H. Kellermann, M. Lüdemann, M. Pohl, and M. Hornung. Design and Optimization of Ram Air–Based Thermal Management Systems for Hybrid-Electric Aircraft. *Aerospace*, 8(1):3, 2021. doi:10.3390/aerospace8010003.

[64] N. J. Pignier, C. J. O'Reilly, and S. Boij. Aerodynamic and aeroacoustic analyses of a submerged air inlet in a low-mach-number flow. *Computers & Fluids*, 133:15–31, 2016. doi:10.1016/j.compfluid.2016.04.010.

[65] L. Piancastelli, L. Frizziero, and G. Donnici. The Meredith ramjet: An efficient way to recover the heat wasted in piston engine cooling. *ARPN Journal of Engineering and Applied Sciences*, 10: 5327–5333, 2015. URL `http://enginehistory.org/Installations/MeredithRamjet.pdf`.

[66] M. Dooley, N. Lui, R. Newman, and C. Lui. Aircraft Thermal Management - Heat Sink Challenge. In *SAE 2014 Aerospace Systems and Technology Conference*. SAE International, sep 2014. doi:10.4271/2014-01-2193.

[67] L. Pang, X. Dang, and J. Cheng. Study on Heat Transfer Performance of Skin Heat Exchanger. *Experimental Heat Transfer*, 28(4):317–327, 2015. doi:10.1080/08916152.2013.876461.

[68] T. Wang, C. Britcher, and P. Martin. Surface heat exchangers for aircraft applications - a technical review and historical survey. In *37th Aerospace Sciences Meeting and Exhibit*, Reno, Nevada, USA, January 1999. doi:10.2514/6.1999-119.

[69] E. Sozer, D. Maldonado, K. Bhamidapati, and S. L. Schnulo. Computational Evaluation of an OML-based Heat Exchanger Concept for HEATheR. In *AIAA Propulsion and Energy 2020 Forum*, (Virtual Event), August 2020. doi:10.2514/6.2020-3575.

[70] S. Schnulo, J. Chapman, P. Hanlon, H. Hasseeb, R. Jansen, D. Sadey, E. Sozer, J. Jensen, D. Maldonado, K. Bhamidapati, N. Heersema, K. Antcliff, Z. Frederick, and J. Kirk. Assessment of the Impact of an Advanced Power System on a Turboelectric Single-Aisle Concept Aircraft. In *2020 AIAA/IEEE Electric Aircraft Technologies Symposium (EATS)*, New Orleans, LA, USA, August 2020. doi:10.2514/6.2020-3548.

[71] H. Kellermann, A. L. Habermann, and M. Hornung. Assessment of Aircraft Surface Heat Exchanger Potential. *Aerospace*, 7(1):1, 2020. doi:10.3390/aerospace7010001.

[72] T. Jia, X. Zhang, Y. Liu, S. Gong, C. Deng, L. Pan, and J.-J. Zou. A comprehensive review of the thermal oxidation stability of jet fuels. *Chemical Engineering Science*, 229:116157, 2021. doi:10.1016/j.ces.2020.116157.

[73] L. J. Spadaccini and H. Huang. On-Line Fuel Deoxygenation for Coke Suppression. *Journal of Engineering for Gas Turbines and Power*, 125(3):686–692, 2003. doi:10.1115/1.1582497.

[74] A. Donovan, R. Roberts, and M. Wolff. Fuel Pump Trade Study for a Conceptual Design of an Integrated Air Vehicle System. In *51st AIAA/SAE/ASEE Joint Propulsion Conference*, Orlando, FL, USA, July 2015. doi:10.2514/6.2015-4172.

[75] European Aviation Safety Agency. Amendment 25: Easy access rules for large aeroplanes, June 2022. URL `https://www.easa.europa.eu/en/downloads/129017/en`.

[76] D. Doman. Fuel Flow Topology and Control for Extending Aircraft Thermal Endurance. *Journal of Thermophysics and Heat Transfer*, 32:1–16, 07 2017. doi:10.2514/1.T5142.

[77] A. van Heerden, D. Judt, C. Lawson, S. Jafari, T. Nikolaidis, and D. Bosak. Framework for integrated dynamic thermal simulation of future civil transport aircraft. In *AIAA Scitech 2020 Forum*, Orlando, FL, USA, January 2020. doi:10.2514/6.2020-1942.

[78] Z. Kang, Z. LIU, G. REN, and Y. LV. Fuel tank modeling and fuel temperature simulation of an aircraft in steady-state and transient-state methods. 11 2015. doi:10.13140/RG.2.1.3000.9681.

[79] A. van Heerden, D. Judt, C. Lawson, and D. Bosak. Effects of more electric systems on fuel tank thermal behaviour. In *MEA 2019 More Electric Aircraft*, Toulouse, France, February 2019.

[80] M. Ahlers. *2. Dynamic Thermal Management System Modeling of a More Electric Aircraft (2008-01-2886)*, pages 13–19. 2016. doi:10.4271/pt-178.

[81] P. Blázquez. Fuel temperature estimation and energy balance within an uav integral wing fuel tank. *WIT Transactions on Engineering Sciences*, 83:463–475, 2014. doi:10.2495/HT140401.

[82] C. Zilio, G. Longo, G. Pernigotto, F. Chiacchio, P. Borrelli, and E. D'Errico. CFD analysis of Aircraft fuel tanks thermal behaviour. volume 923, 06 2017. doi:10.1088/1742-6596/923/1/012027.

[83] B. German. A Tank Heating Model for Aircraft Fuel Thermal Systems with Recirculation. volume 28, 2011. doi:10.2514/6.2011-641.

[84] D. B. Doman. Optimal Cruise Altitude for Aircraft Thermal Management. *Journal of Guidance, Control, and Dynamics*, 38(11):2084–2095, 2015. doi:10.2514/1.G000845.

[85] P. Huang and D. Doman. Thermal Management of Single- and Dual-Tank Fuel-Flow Topologies Using an Optimal Control Strategy. *Journal of Thermal Science and Engineering Applications*, 10: 041019, 05 2018. doi:10.1115/1.4040036.

[86] E. J. Alyanak and D. L. Allison. Fuel Thermal Management System Consideration in Conceptual Design Sizing. In *57th AIAA/ASCE/AHS/ASC Structures, Structural Dynamics, and Materials Conference*, San Diego, California, USA, January . doi:10.2514/6.2016-0670.

[87] R. Manna, N. Ravikumar, S. Harrison, and K. Goni Boulama. Aircraft Fuel Thermal Management System and Flight Thermal Endurance. *Transactions of the Canadian Society for Mechanical Engineering*, 46(2), 2022. doi:10.1139/tcsme-2021-0146.

[88] G. P. Huang, D. B. Doman, M. J. Rothenberger, B. Hencey, M. P. DeSimio, A. Tipton, and D. O. Sigthorsson. Dimensional Analysis, Modeling, and Experimental Validation of an Aircraft Fuel Thermal Management System. *Journal of Thermophysics and Heat Transfer*, 33(4):983–993, 2019. doi:10.2514/1.T5660.

[89] L. Pang, S. Li, M. Liu, R. A, A. Li, and F. Meng. Influence of the Design Parameters of a Fuel Thermal Management System on Its Thermal Endurance. *Energies*, 11(7):1677, 2018. doi:10.3390/en11071677.

[90] H. Kellermann, A. Habermann, P. Vratny, and M. Hornung. Assessment of fuel as alternative heat sink for future aircraft. *Applied Thermal Engineering*, 170:114985, 2020. doi:10.1016/j.applthermaleng.2020.114985.

[91] A. G. Mohammed, K. E. Elfeky, and Q. Wang. Thermal management evaluation of Li-ion battery employing multiple phase change materials integrated thin heat sinks for hybrid electric vehicles. *Journal of Power Sources*, 516:230680, 2021. doi:10.1016/j.jpowsour.2021.230680.

[92] P. Ziolkowski, K. Zabrocki, and E. Müller. Teg design for waste heat recovery at an aviation jet engine nozzle. *Applied Sciences*, 8(12):2637, 2018. doi:10.3390/app8122637.

[93] S. Crossley, N. Mathur, and X. Moya. New developments in caloric materials for cooling applications. *AIP Advances*, 5:067153, 2015. doi:10.1063/1.4922871.

[94] K. A. Abdul Khalid, T. J. Leong, and K. Mohamed. Review on Thermionic Energy Converters. *IEEE Transactions on Electron Devices*, 63(6):2231–2241, 2016. doi:10.1109/TED.2016.2556751.

[95] J. E. Hesselgreaves, R. Law, and D. A. Reay. Chapter 1 - introduction. In J. E. Hesselgreaves, R. Law, and D. A. Reay, editors, *Compact Heat Exchangers*, pages 1–33. Butterworth-Heinemann, second edition, 2017. doi:10.1016/B978-0-08-100305-3.00001-X.

[96] W. M. Kays and A. L. London. *Compact heat exchangers*. 1984. URL `https://www.osti.gov/biblio/6132549`.

[97] K. Kasim, A. Muley, M. Stoia, and F. Ladeinde. Advanced Heat Transfer Devices for Aerospace Applications. In *ASME 2017 International Mechanical Engineering Congress and Exposition*, Tampa, Florida, USA, November 2017. doi:10.1115/IMECE2017-72382.

[98] J. E. Hesselgreaves, R. Law, and D. A. Reay. Chapter 4 - surface comparisons, size, shape and weight relationships. In J. E. Hesselgreaves, R. Law, and D. A. Reay, editors, *Compact Heat Exchangers*, pages 129–155. Butterworth-Heinemann, second edition, 2017. doi:10.1016/B978-0-08-100305-3.00004-5.

[99] A. Faghri. Review and Advances in Heat Pipe Science and Technology. *Journal of Heat Transfer*, 134(12), 2012. doi:10.1115/1.4007407.

[100] W. G. Anderson, J. Hartenstine, M. Ellis, J. Montgomery, and C. Peters. Electronics Cooling Using High Temperature Loop Heat Pipes With Multiple Condensers. In *Power Systems Conference*, Fort Worth, TX, USA, November 2010. doi:10.4271/2010-01-1736.

[101] M. Donovan and P. Del valle. Aeronautical Passive Energy Recovery System based on LHP Technology Extended Test Results. In *SAE 2014 Aerospace Systems and Technology Conference*, Cincinnati, Ohio, USA, September 2014. doi:10.4271/2014-01-2191.

[102] I. Kaur and P. Singh. State-of-the-art in heat exchanger additive manufacturing. *International Journal of Heat and Mass Transfer*, 178:121600, 2021. doi:10.1016/j.ijheatmasstransfer.2021.121600.

[103] A. Almertejy, M. M. Rashid, N. Ali, and S. Almurtaji. Application of Nanofluids in Gas Turbine and Intercoolers - A Comprehensive Review. *Nanomaterials*, 12(3):338, 2022. doi:10.3390/nano12030338.

[104] C. Perullo, M. Shi, G. Cinar, A. Alahmad, M. Sanders, D. N. Mavris, and M. Benzakein. An Update on Sizing and Performance Analysis of a Hybrid Turboelectric Regional Jet for the NASA ULI Program. In *AIAA Propulsion and Energy 2020 Forum*, (Virtual Event), August 2020. doi:10.2514/6.2020-3590.

[105] M. Shi, M. Sanders, A. Alahmad, C. Perullo, G. Cina, and D. N. Mavris. Design and Analysis of the Thermal Management System of a Hybrid Turboelectric Regional Jet for the NASA ULI Program. In *AIAA Propulsion and Energy 2020 Forum*, (Virtual Evente), August 2020. doi:10.2514/6.2020-3572.

[106] J. W. Chapman, H. Hasseeb, and S. L. Schnulo. Thermal Management System Design for Electrified Aircraft Propulsion Concepts. In *AIAA Propulsion and Energy 2020 Forum*, (Virtual Event), August 2020. doi:10.2514/6.2020-3571.

[107] N. Heersema and R. Jansen. Thermal Management System Trade Study for SUSAN Electrofan Aircraft. In *AIAA SCITECH 2022 Forum*, San Diego, CA, USA, January 2022. doi:10.2514/6.2022-2302.

[108] NASA Glenn Research Center. Subsonic Single Aft Engine (SUSAN) Aircraft. `https://www1.grc.nasa.gov/aeronautics/eap/airplane-concepts/susan/`, 2022. Accessed: 2022-08-15.

[109] N. Moebs, D. Eisenhut, E. Windels, J. van der Pols, and A. Strohmayer. Adaptive Initial Sizing Method and Safety Assessment for Hybrid-Electric Regional Aircraft. *Aerospace*, 9(3):150, 2022. doi:10.3390/aerospace9030150.

[110] D. Eisenhut, N. Moebs, E. Windels, D. Bergmann, I. Geiß, R. Reis, and A. Strohmayer. Aircraft Requirements for Sustainable Regional Aviation. *Aerospace*, 8(3):61, 2021. doi:10.3390/aerospace8030061.

[111] R. dos Reis, F. Odaguil, E. Windels, Y. Teeuwen, J. van der Pols, P. Laskaridis, D. Bergmann, D. Eisenhut, and N. Moebs. Requirements and reference aircraft. https://cordis.europa.eu/project/id/875551/results, march 2021. Deliverable 2.1, last accessed on 18-10-2022.

[112] ATR 42-600 Fact Sheet. http://1tr779ud5r1jjgc938wedppw-wpengine.netdna-ssl.com/wp-content/uploads/2020/07/Factsheets_-_ATR_42-600.pdf. Accessed on: 17/09/2022.

[113] F. P. Incropera and D. P. DeWitt. *Fundamentals of Heat and Mass Transfer*. John Wiley & Sons, New York City, New York, 7th edition, 2011.

[114] AC-9 Aircraft Environmental Systems Committee. *Thermophysical Characteristics of Working Fluids and Heat Transfer Fluids*, May 2017.

[115] AC-9 Aircraft Environmental Systems Committee. Heat Sinks for Airborne Vehicles, December 2021.

[116] M. Moran, H. Shapiro, D. Boettner, and M. Bailey. *Fundamentals of Engineering Thermodynamics*. Wiley, 2010. ISBN 9780470495902.

[117] J. E. Hesselgreaves, R. Law, and D. A. Reay. Chapter 7 - thermal design. In J. E. Hesselgreaves, R. Law, and D. A. Reay, editors, *Compact Heat Exchangers*, pages 275–360. Butterworth-Heinemann, second edition, 2017. doi:10.1016/B978-0-08-100305-3.00007-0.

[118] Engineers Edge. Overall Heat Transfer Coefficients in Heat Exchangers, . URL https://www.engineersedge.com/heat_transfer/overall_heat_transfer_coefficients_13827.htm. Accessed: 2022-07-27.

[119] Engineers Edge. Overall heat transfer coefficients in heat exchangers. https://www.engineersedge.com/thermodynamics/overall_heat_transfer-table.htm, . Accessed: 2022-07-27.

[120] R. Larkens. A coupled propulsion and thermal management system for hybrid electric aircraft design: A case study. MSc in Aerospace Engineering, Delft University of Technology, 2020.

[121] Philip G. Hill e Carl R. Peterson. *Mechanics and Thermodynamics of Propulsion*. Addison-Wesley Publishing Company, 2nd edition, 1992.

[122] V. Gnielinski. New equations for heat and mass transfer in turbulent pipe and channel flow. *Int. Chem. Eng*, 16(2):359–368, 1976.

[123] American Society of Heating Refrigerating and Air-Conditioning Engineers. *ASHRAE Handbook: Heating Ventilating and Air-Conditioning Applications SI Edition*. 2015.

[124] Gevo. Alcohol-to-Jet Synthetic Paraffinic Kerosene Is a Proven Pathway to Deliver a Bio-Based, Low-Carbon Option to Travelers. Technical report, December 2019. URL https://gevo.com/wp-content/uploads/2020/05/Gevo-Whitepaper-Sustainable-Aviation-Fuel.pdf.

[125] US Air Force Research Laboratory. Research for the aerospace systems directorate (r4rq), delivery order 0006: Airbreathing propulsion fuels and energy. Technical report, June 2017. URL https://apps.dtic.mil/sti/pdfs/AD1037321.pdf.

[126] G. Bindolino, G. Ghiringhelli, S. Ricci, and M. Terraneo. Multilevel Structural Optimization for Preliminary Wing-Box Weight Estimation. *Journal of Aircraft*, 47(2):475–489, 2010. doi:10.2514/1.41552.

[127] O. Dababneh and T. Kipouros. Influence of high fidelity structural models on the predicted mass of aircraft wing using design optimization. *Aerospace Science and Technology*, 79:164–173, 2018. ISSN 1270-9638. doi:10.1016/j.ast.2018.05.043.

[128] T. C. Cork. *Design of Aircraft*. Prentice Hall, New Jersey, USA, 2003.

[129] B. McBride, M. Zehe, and S. Gordon. NASA Glenn coefficients for calculating thermodynamic properties of individual species. Technical Report NASA/TP-2002-211556, NASA, Spetember 2002.

[130] J. R. R. A. Martins and A. Ning. *Engineering Design Optimization*. Cambridge University Press, 2021. ISBN 9781108833417. doi:10.1017/9781108980647.

[131] M. J. Kochenderfer and T. A. Wheeler. *Algorithms for optimization*. MIT Press, Cambridge, Massachuetts, USA, 2019.

[132] K. Deb, A. Pratap, S. Agarwal, and T. Meyarivan. A fast and elitist multiobjective genetic algorithm: NSGA-II. *IEEE Transactions on Evolutionary Computation*, 6(2):182–197, 2002. doi:10.1109/4235.996017.

[133] A. Seshadri. NSGA - II: A multi-objective optimization algorithm. https://www.mathworks.com/matlabcentral/fileexchange/10429-nsga-ii-a-multi-objective-optimization-algorithm, 2022. Accessed: 2022-07-15.

[134] X. Yu and X. Du. Reliability-based multidisciplinary optimization for aircraft wing design. *Structure and Infrastructure Engineering*, 2(3-4):277–289, 2006. doi:10.1080/15732470600590333.

[135] R. M. Paiva, C. Crawford, and A. Suleman. Robust and Reliability-Based Design Optimization Framework for Wing Design. *AIAA Journal*, 52(4):711–724, 2014. doi:10.2514/1.J052161.

[136] J. R. D'Errico and N. A. Zaino. Statistical Tolerancing Using a Modification of Taguchi's Method. *Technometrics*, 30(4):397–405, 1988. URL http://www.jstor.org/stable/1269802.

[137] M. C. Aral, M. Suhermanto, and M. Hosoz. Performance evaluation of an automotive air conditioning and heat pump system using R1234yf and R134a. *Science and Technology for the Built Environment*, 27(1):44–60, 2021. doi:10.1080/23744731.2020.1776067.

[138] M. W. Oppenheimer, D. Sigthorsson, and D. B. Doman. Extending Aircraft Thermal Endurance by Fuel Pump Sizing. In *2018 AIAA Guidance, Navigation, and Control Conference*, Kissimmee, Florida, USA, January 2018. doi:10.2514/6.2018-0856.

[139] U. Neuling and M. Kaltschmitt. Techno-economic and environmental analysis of aviation biofuels. *Fuel Processing Technology*, 171:54–69, mar 2018. ISSN 0378-3820. doi:10.1016/J.FUPROC.2017.09.022.

[140] C. Xu, Q. Dai, L. Gaines, M. Hu, A. Tukker, and B. Steubing. Future material demand for automotive lithium-based batteries. *Communications Materials*, 1:99, 2020. doi:10.1038/s43246-020-00095-x.

[141] S. Xu, Z. Li, Q. Yang, G. Chu, J. Zhang, D. Zhang, H. Zhou, and M. Gao. Comparative Life Cycle Assessment of Energy Consumption, Pollutant Emission, and Cost Analysis of Coal/Oil/Biomass to Ethylene Glycol. *ACS Sustainable Chemistry & Engineering*, 9(47):15849–15860, 2021. doi:10.1021/acssuschemeng.1c05454.

[142] ICAO Carbon Emissions Calculator. URL https://www.icao.int/environmental-protection/Carbonoffset/Pages/default.aspx. Accessed on: 2022-10-08.

[143] Greenhouse gas emission intensity of electricity generation in Europe. URL https://www.eea.europa.eu/ims/greenhouse-gas-emission-intensity-of-1. Accessed on: 2022-10-08.

Appendix A

Extra figures, graphs and tables

A.1 Aircraft initial design and sizing parameters

Figure A.1: FutPrInt50 aircraft initial design.

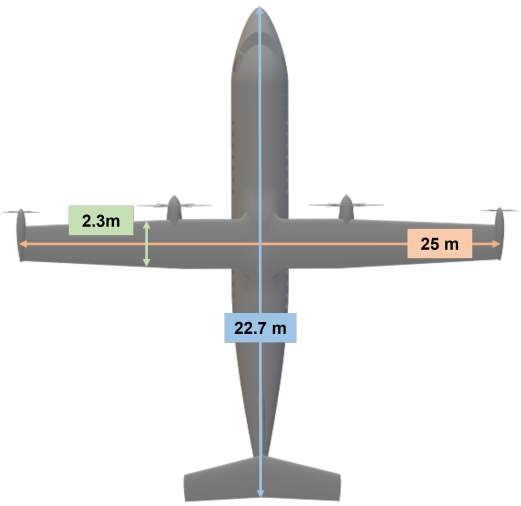

Figure A.2: FutPrInt50 aircraft initial sizing parameters.

A.2 Simulink blocks diagram

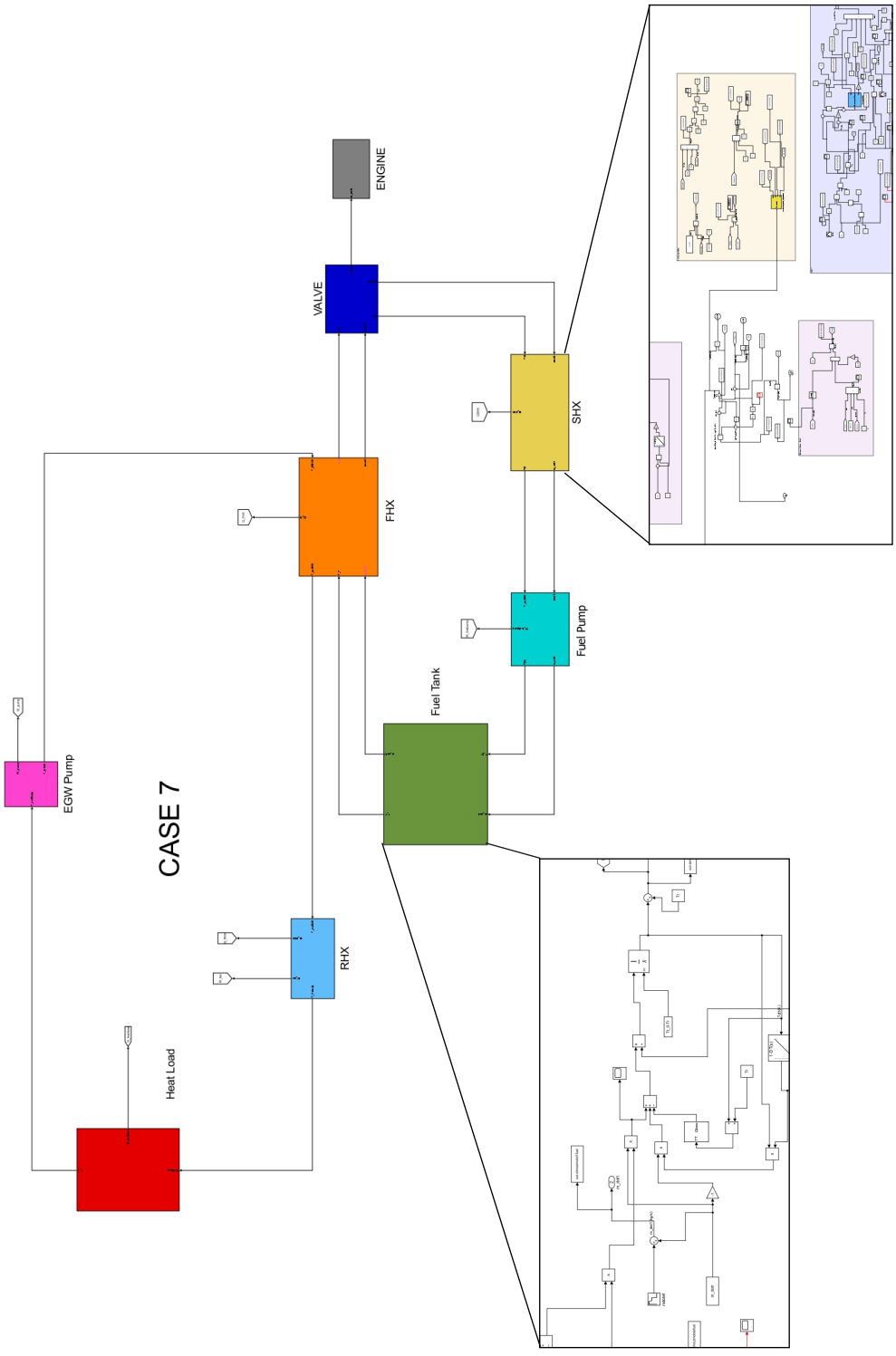

Figure A.3: Architecture 5 blocks diagram.

A.3 Regression component mass curves

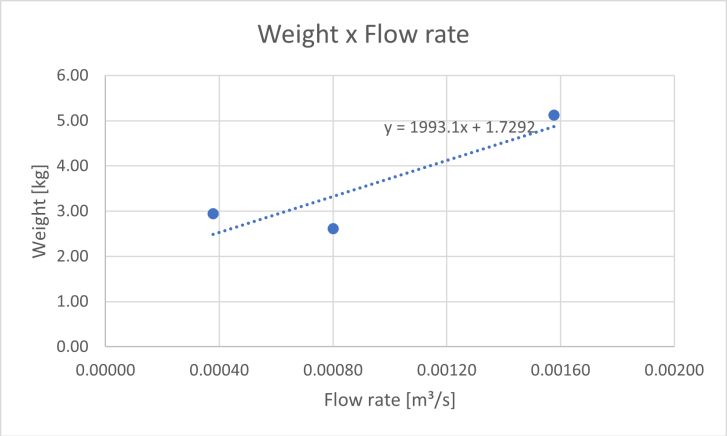

Figure A.4: Hydraulic pump mass regression.

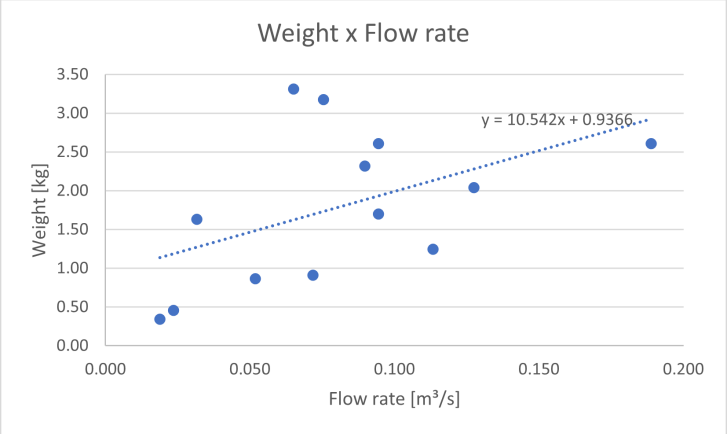

Figure A.5: Fan mass regression.

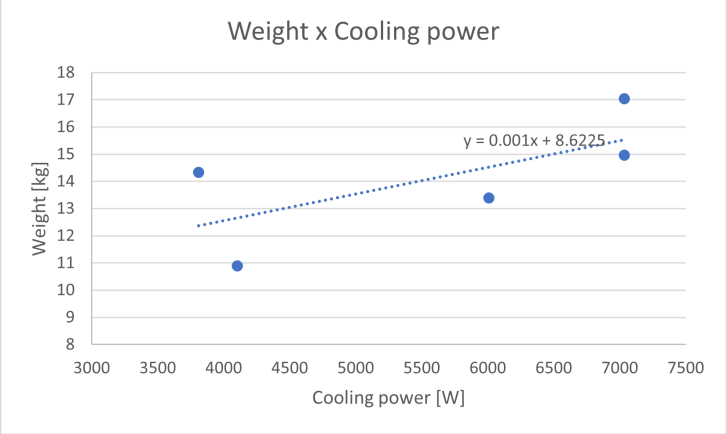

Figure A.6: Compressor mass regression.

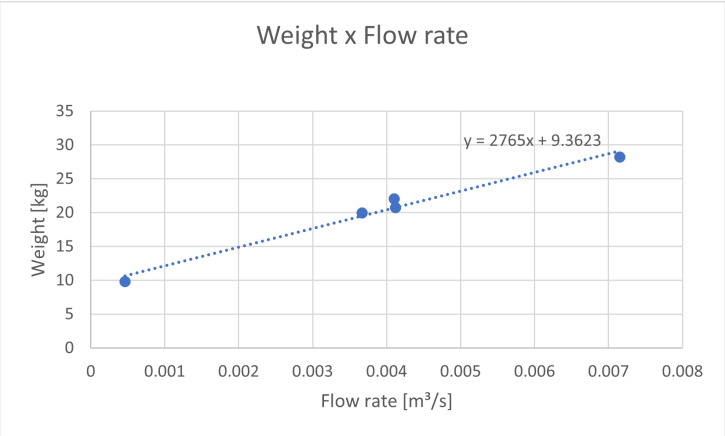

Figure A.7: Fuel pump mass regression.

A.4 Architectures flowcharts

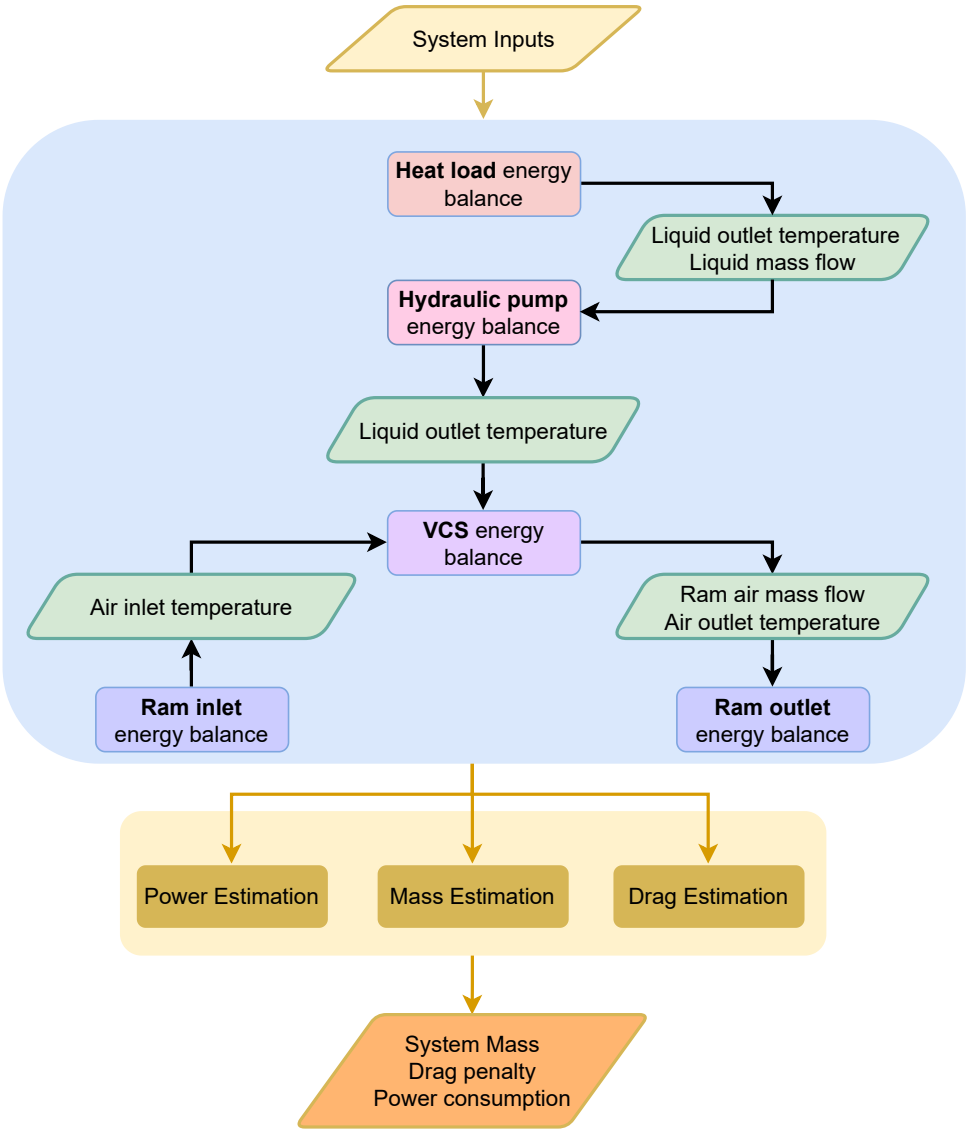

Figure A.8: Architecture 1 flowchart.

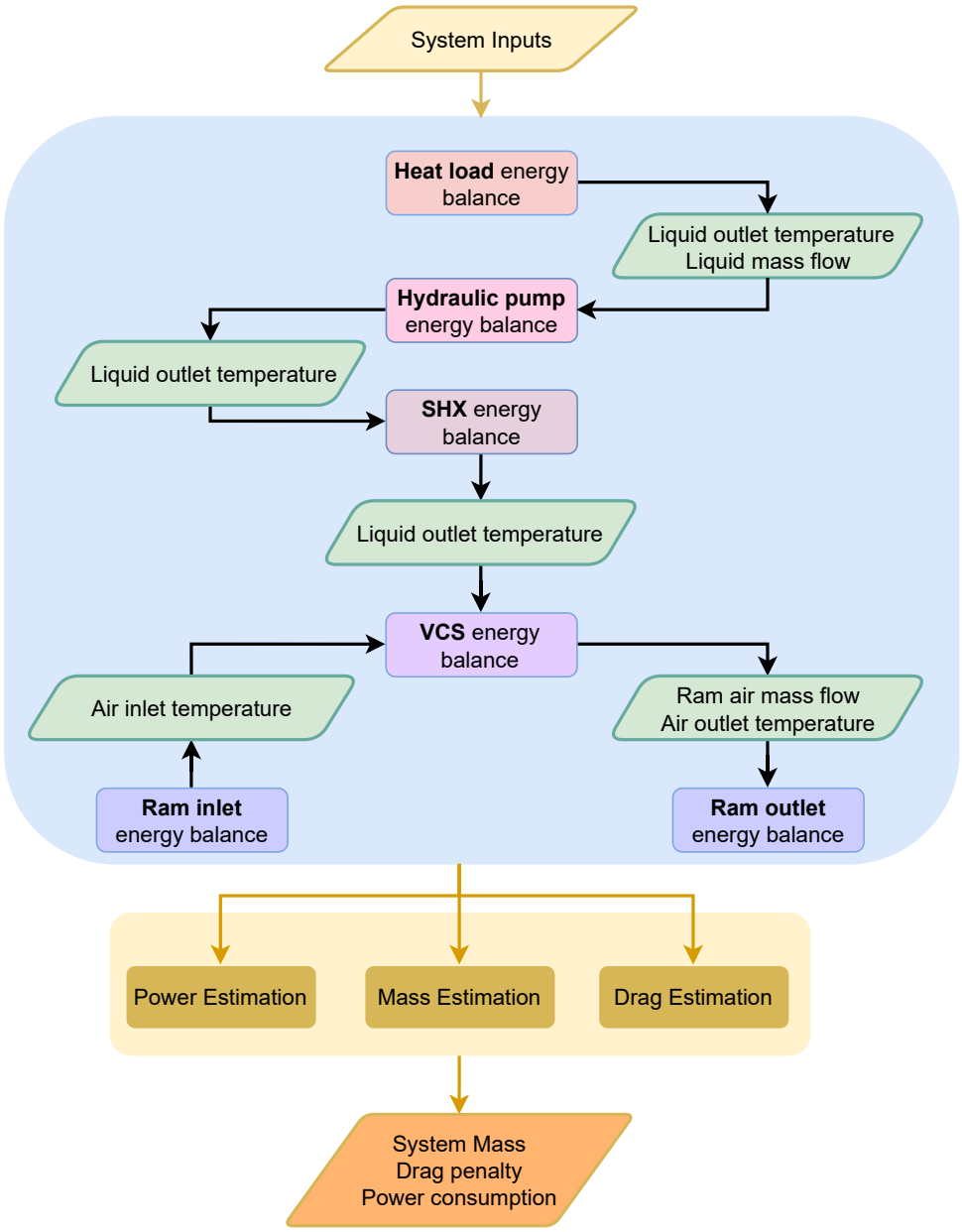

Figure A.9: Architecture 2 flowchart.

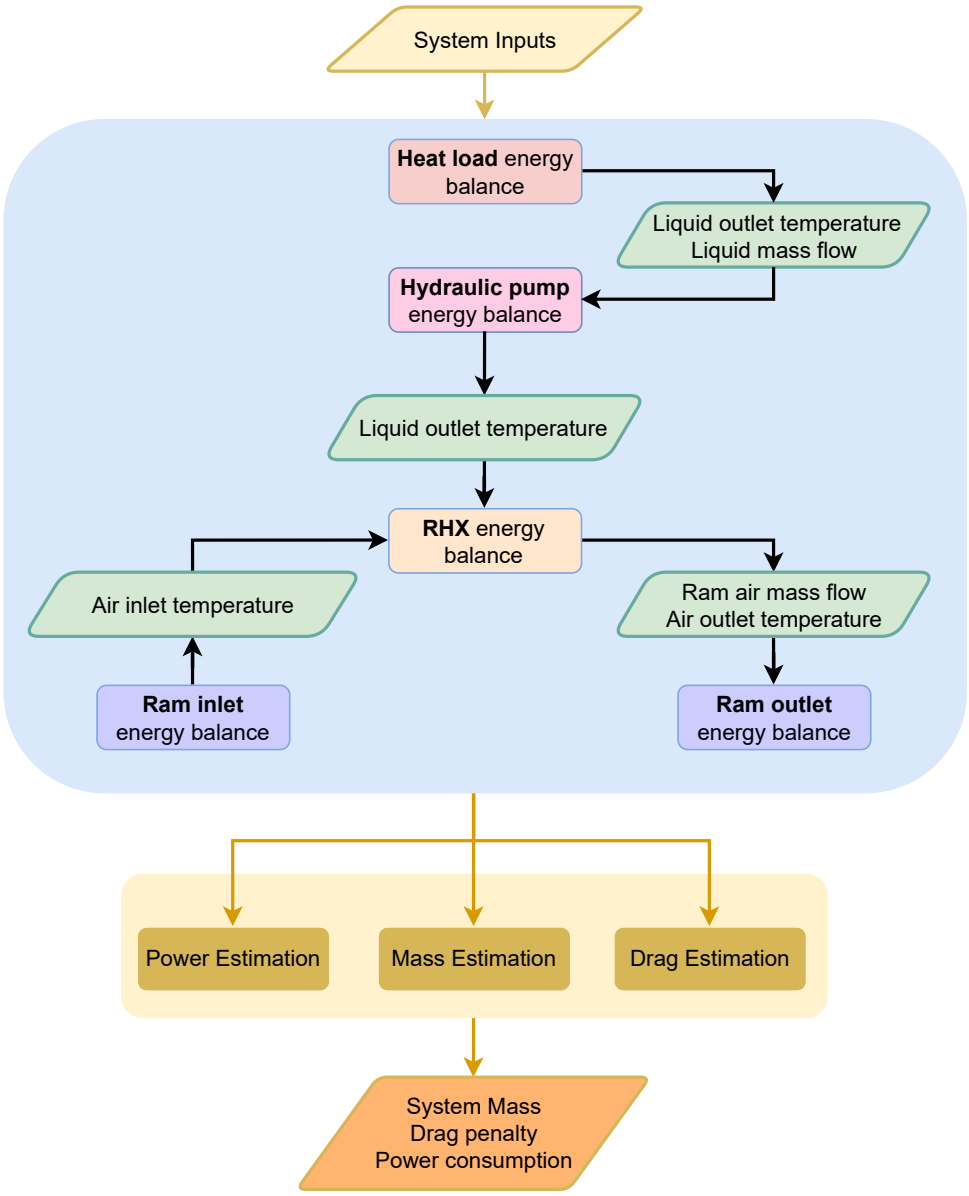

Figure A.10: Architecture 3 flowchart.

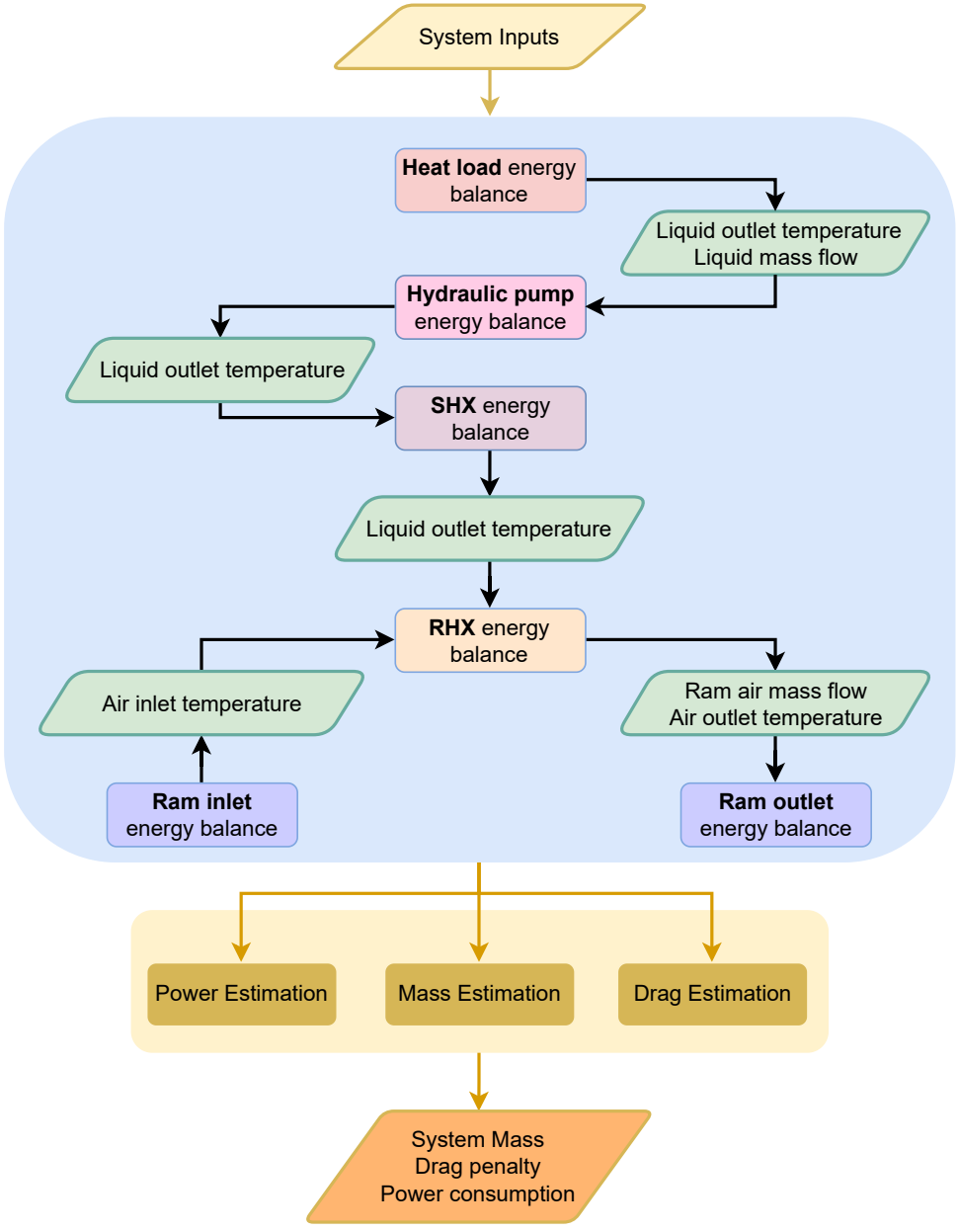

Figure A.11: Architecture 4 flowchart.

A.5 Optimisation design variables

Table A.1: Design Variables Upper Boundary (UB), Lower Boundary (LB), nominal value and the respective reference.

	DV	LB	UB	Nominal	Reference
A2	A_{SHX}	2	7	5	FutPrInt50 aircraft
	X	5	18	18	FutPrInt50 aircraft
	t_{bd}	0.005	0.05	0.01	Project, [67]
	$\dot{m}_{\text{liquid}}$	$0.023 \cdot Q_{\text{equip}}$	$0.045 \cdot Q_{\text{equip}}$	$0.045 \cdot Q_{\text{equip}}$	[115]
	ΔT (HEX)	6	12	10	Project
A4	A_{SHX}	2	7	5	FutPrInt50 aircraft
	X	5	18	18	FutPrInt50 aircraft
	t_{bd}	0.005	0.05	0.01	[67]
	$\dot{m}_{\text{liquid}}$	$0.023 \cdot Q_{\text{equip}}$	$0.045 \cdot Q_{\text{equip}}$	$0.045 \cdot Q_{\text{equip}}$	[115]
	ΔT (HEX)	6	12	10	Project
A5	A_{SHX}	2	5	5	FutPrInt50 aircraft
	X_{wing}	0.25	0.75	0.5750	FutPrInt50 aircraft
	t_{bd}	0.005	0.05	0.01	Project, [67]
	$\dot{m}_{\text{liquid}}$	$0.023 \cdot Q_{\text{equip}}$	$0.045 \cdot Q_{\text{equip}}$	$0.045 \cdot Q_{\text{equip}}$	[115]
	ΔT (HEX)	6	12	10	Project
	T_{T0}	280	290	288	[87]
	$\dot{m}_r$	0.15	0.2	0.15	[87]
	Tank b percent	60	85	70	[126]
	Tank c percent	12	71	25	[127]
	U_{wall}	30	50	40	Project

A.6 Emission factors

Table A.2: Different emission factors (optimistic and pessimistic scenarios.)

	Component	Emission factor	Reference
Production	Biofuel ATJ from wheat straw	31 gCO_2-eq/MJfuel	[139]
	Jet Fuel A1	87.5 gCO_2-eq/MJ-fuel	[139]
	Li-ion battery (LFP-Graphite)	40 $kgCO_2$-eq/(kWh)	[140]
	EGW (from a biomass source)	3489 kgCO2-eq/ton-EG	[141]
	EGW (from coal)	7538 kgCO2-eq/ton-EG	[141]
	Component	**Emission factor**	**Reference**
Consumption	Biofuel and fuel	3.16 $kgCO_2$-eq/kg-fuel	[142]
	Electric Mix (EU-27, 2020)	229 gCO_2-eq/(kWh)	[143]
	Electric Mix (Sweden, 2020)	8 gCO_2-eq/(kWh)	[143]